Title

Dynamic regulation of T cell priming in cancer and infection

Author

Hiam, Kamir J

Publication Date

2020

Dynamic Regulation of T Cell Priming in Cancer and Infection

by
Kamir John Hiam

DISSERTATION
Submitted in partial satisfaction of the requirements for degree of
DOCTOR OF PHILOSOPHY

in

Biomedical Sciences

in the

GRADUATE DIVISION
of the
UNIVERSITY OF CALIFORNIA, SAN FRANCISCO

Approved:

DocuSigned by:
Lewis Lanier
C111345FC07E42F...
Lewis Lanier
Chair

DocuSigned by:
Matthew Spitzer
[illegible]479...
Matthew Spitzer

DocuSigned by:
Cliff Lowell
[illegible]C7...
Cliff Lowell

DocuSigned by:
Larry Fong
91A2D66309BE4D7...
Larry Fong

Committee Members

This dissertation is dedicated to:

My parents John Robert Hiam and Doris Hiam-Galvez

My partner Didi Zhu

My grandparents who all passed away before I started graduate school: Nancy Hiam, Robert Hiam, Augusto Galvez Soto, Luz Galvez Sosa

My godfather who passed away during my time in graduate school: Bernard Lietaer

My scientific mentors before graduate school: Dr. Michael Van Dyke, Dr. Slobodan Beronja, Dr. Julie Rytlewski, Dr. Manu Platt, Dr. Meghan Ferrall-Fairbanks

My ancestors in Peru and England

Acknowledgements

Growing up, I had absolutely no intention of becoming a scientist. Instead, I wanted to be creative and make my living as a writer and musician. Based on my experiences in science classes, a career in science seemed like the least creative field possible. While I was quite interested in some scientific concepts, my middle school and high school science coursework made me certain I would never want to be a scientist. And yet now I cannot imagine doing anything else with my life. The three most important things that allowed me to succeed in this unexpected path are the support of my parents, the very early support I received from my first mentors in science, and the freedom of exploration I was afforded in graduate school by my thesis advisor Dr. Matt Spitzer.

I owe a great deal to Matt as a mentor and am honored to have been his first graduate student. In his lab, I've been able to explore and fail with so many topics that interested me and learn a great deal in the process. I am also incredibly thankful to always feel supported no matter what I was working on in lab and also supported outside the lab. Matt has also been an outstanding role model in a position I also aim to attain. I aim to emulate his scientific prowess, as well as charisma and compassion in my own career.

I would also like to thank the whole Spitzer lab that grew so much during my time there. I specifically would like to thank Bree Allen and Lauren Levine with whom I was so fortunate to join forces with for my co-first author papers. I would also like to especially thank Rachel DeBarge who helped me grow so much as a scientist and person by being the first trainee I mentored for a long time. I am also especially thankful of Nam Woo Cho, Jackie Yee, and Joel Babdor who have all been great scientific

colleagues and generally great people away from science as well. In short, the lab has been so great to be a part of.

Outside of the Spitzer lab I was also so lucky to be surrounded by a community of knowledgeable and kind scientists. I am thankful to my thesis committee and qualifying exam committee for providing critical feedback and new perspectives on biology: Lewis Lanier, Cliff Lowell, Larry Fong, Scott Kogan, and Melissa Reeves. I'm also thankful for the postdocs and senior grad students in senior labs that I would ask for help from frequently in my first few years in lab: John Gagnon, Marc Potempa, Eric Dang, Oscar Aguilar, Miqdad Dhariwala, and Su Yang Liu. I'm also thankful for the amazing flow core personnel where I spent so much time throughout grad school especially Stanley Tamaki, Claudia Bispo, and Vinh Nguyen. I'm also thankful to my cohort of BMS students, as well as the years above and below my class. It is very helpful to have a group of trainees going through the same processes at the same time.

I'm also eternally grateful for the support of my partner Didi. She gives meaning to everything and helps me feel remember what is important in life. Of course, I am also incredibly thankful for my parents who have supported me no matter what I have done. I could not have achieved what I have without their love and support.

Dynamic Regulation of T Cell Priming in Cancer and Infection

Kamir J. Hiam

Abstract

An immunological challenge initiates cascades of migration, activation, and interactions between diverse immune cell subsets that ultimately lead to protection of the host. Previous technological limitations have favored reductionist experimentation and hindered experimental and analytical assessment of the full breadth of immunological responses. Therefore, many emergent properties of pan-lineage dynamic immune responses have remained elusive. The present body of work addresses this gap in fundamental immunology by leveraging high-dimensional single-cell technologies and *in vivo* mouse models of immune responses to dissect the dynamic regulation of T cell priming in both cancer and infection. Generation of immune organization maps in eight tumor models showed that the global immune macroenvironment in cancer is significantly dysregulated as shown by gross alterations in cell frequencies and phenotypes. Orthogonal pathogen challenges in tumor-burdened mice revealed peripheral defects in CD8 T cell differentiation that were caused by impaired dendritic cell (DC) activation. To further profile natural immunity to bacterial challenges, mass cytometry was adapted to profile metabolic enzymes during an *in vivo* bacterial immune response. We revealed a highly transient early activated CD8 T cell state characterized by peak utilization of oxidative phosphorylation and glycolysis. Assessing all splenic immune lineages during an antibacterial immune response uncovered a DC activation zenith at two days post-infection. Peak DC activation functioned as a temporal regulator of T cell fate as late arriving T cells acquired memory T cell fate exclusively. Taken together these studies reveal transient functionally significant stages of regulation during cancer and infection.

TABLE OF CONTENTS

LIST OF FIGURES

LIST OF TABLES

Chapter 1 Introduction

1.1 Overview

The precise coordination of all immune cells throughout immune responses has not been thoroughly investigated. Recent work has begun to show that virtually all immune cells respond to an immunological insult such as an infection or tumor. Therefore. it is critical to understand the full scale of immune cell dynamics at critical stages of the immune response to identify how the immune system collectively makes decisions. By leveraging high-dimensional single-cell cytometry, *in vivo* challenges, and targeted perturbation experiments, the aims of this thesis were as follows:

1) Determine the consequences of tumor development on peripheral immune organization and function, described in chapter 2.
2) Map the metabolic differentiation trajectory of CD8 T cells at single cell resolution, described in chapter 3.
3) Identify how the entire splenic immune landscape rapidly responds to acute infection, described in chapter 4.

1.2 Systemic Perturbations to Immune Organization by Tumor Burden

Cancer is a systemic disease and prolonged inflammation is hallmark of cancer[1]. Whether this inflammation initiates tumorigenesis or supports tumor growth is context dependent, but ultimately the global immune landscape beyond the tumor is significantly altered. Despite systemic perturbations to the immune system, immunotherapy has revolutionized cancer therapy. However, immunotherapy remains ineffective in most clinical contexts[2]. Further progress towards more broadly effective immunotherapeutic strategies requires a deeper understanding of the organism-wide immunological relationships between tumor and host.

The tumor immunology field has focused heavily on local immune responses in the tumor microenvironment, yet immunity is coordinated across tissues. For example, many myeloid cells are frequently replenished from hematopoietic precursors in the bone marrow[3], and critical T cell priming events occur in lymphoid tissues as opposed to non-lymphoid organs such as a tumor[4]. The localized antitumor immune response cannot exist without continuous communication with the periphery. Furthermore, virtually every subset of immune cell has been implicated in cancer biology[5]. Therefore, studying immune responses to cancer must also focus on all the immune lineages within the peripheral immune system beyond the tumor microenvironment.

Many human cancers and mouse models of cancer drive extensive disruption of hematopoiesis. This manifests most prominently in an expansion of immature neutrophils and monocytes in the periphery of tumor-burdened hosts, which then also traffic to the tumor microenvironment and contribute to the local immunosuppression[6–8]. Hematopoietic stem and progenitor cells are mobilized into proliferation and differentiation towards the monocytic and granulocytic lineages, resulting in peripheral expansion and intratumoral accumulation of immunosuppressive neutrophils, monocytes, and macrophage lineages[9–13]. Several factors have been implicated in driving this process including G-CSF[10,14], GM-CSF[15,16], IL-17[13], oxysterol[17], IL-8[18], CCL2[12], and IL1-β[19]. The vast majority of research that highlights peripheral immune perturbations has focused on this increase in immature and immunosuppressive myeloid populations; however, this expansion does not occur in isolation.

Beyond excessive production of monocytic and neutrophilic cells through aberrant hematopoiesis, bone marrow-derived dendritic cell (DC) perturbations have long been observed in the periphery of tumor-burdened hosts. This has important implications for the development of antitumor immune responses as DCs are critical orchestrators of CD8 and CD4 T cell differentiation and proliferation in many contexts including cancer[20]. The frequency of DC subsets is decreased in the peripheral blood of human ovarian[21], prostate[22], breast[23], HNSCC[24], melanoma[25], lung[26], and renal[27] cancers when compared to healthy individuals. In pancreatic and breast cancer patient and mouse models, decreased peripheral DC frequency was driven through tumor-derived GCSF downregulating IRF8 in DC precursors, which reduced differentiation of mature DCs[28]. An alternative mechanism for DC paucity in a mouse model of pancreatic cancer was shown to be mediated by serum IL-6 driving increased DC apoptosis[29]. In human and mouse pancreatic cancer peripheral DCs obtain a semi-mature state characterized by moderate increases in costimulatory and coinhibitory receptors[29–31]. Transcriptomics revealed that these semi-mature DCs upregulated genes involved in proteasomal degradation but failed to upregulate T cell polarizing cytokines[29], suggesting that like semi-mature DCs in other contexts, they possess the capacity to provide only partial stimulation to T cells.

Substantially less is known about the organization of other major immune lineages in the tumor macroenvironment. Lymphopenia is common in breast cancer, lymphoma, and sarcoma patients[32]. Interestingly, human breast[33], lung[34], and cervical[35] cancer patients have decreased diversity of their circulating TCR repertoire. As larger TCR diversity is associated with better tumor control[36], an improved understanding of TCR repertoire fluctuations driven by cancer is warranted. Peripheral T cells are also functionally perturbed as polyclonal memory CD4 and CD8 T cells from the peripheral blood have decreased capacity to produce IL-2 and IFNγ in response to stimulation with PMA and ionomycin in human breast cancer patients[37]. Peripheral naïve CD4 T cells also exhibitied decreased responses to IL-6 stimulation as measured by phosphorylation of STAT1 and STAT3 in human breast cancer patients[38]. The most well studied perturbation of T cells in cancer is the expansion of suppressive regulatory CD4 T cells (Tregs) in the periphery and infiltration into the tumor[39]. Recent work has now shown that Tregs present in the blood of human cancer patients share phenotypic and TCR repertoires with intratumoral T cells, suggesting that a significant proportion of intratumoral suppressive Tregs are derived from naturally occurring thymic Tregs rather than through tumor-induced differentiation of naïve CD4 T cells[40,41]. NK cells are yet another important component of antitumor immunity than can directly kill tumor cells, as well as influence antitumorigenic behavior of other immune cells[42]. Similar to the many other cell types described previously, peripheral NK cells from human breast cancer patients also have altered phenotype characterized by decreased expression of activating receptors including NKp30, NKG2D, and 2B4, as well as exhibiting impaired capacity to directly kill target cells and degranulate *in vitro*[43]. Altogether, data overwhelming support the systemic corruption of immune organization in diverse tumor types. Further work is needed to fully characterize distinct new types of immune state based on tumor tissue of origin, stage of development, and patient demographics in order to inform therapeutics and future mechanistic studies of the causes for systemic disruptions.

1.3 Peripheral Immune Coordination of Antitumor Immunity

Immune cells from the periphery of tumor-burdened hosts are required for natural and therapeutically induced tumor control. Chemotherapeutic depletion of peripheral immune cells impedes the therapeutic benefit by PD-1 blockade, causing systemic lymphodepletion and abrogating long-term immune memory[44]. However, local use of chemotherapy spares peripheral immune cells and synergizes with PD-1 blockade to induce DC infiltration into the tumor and clonal expansion of tumor-specific effector T cells. A specialized subset of CD103+ DCs transport tumor antigen to the peripheral immune system by CCR7-dependent migration from the tumor to the draining lymph node where the priming of tumor specific CD8 T cells occurs[45–48]. Newly primed T cells then traffic from the lymph node to the tumor and this cycle is an essential process in natural and therapeutically induced antitumor immunity. As further evidence of continuous systemic reliance, blockade of lymphocyte egress from lymphoid organs using FTY720 or surgical resection of tumor-draining lymph nodes nullifies efficacy of immunotherapy[49,50].

Productive antitumor responses predominantly utilize effector CD8 T cells within the tumor microenvironment to directly kill tumor cells. However, recent studies demonstrate that intratumoral T cells acquire a terminally dysfunctional state in which cells are no longer amenable to therapeutic reinvigoration[51]. Additional studies have identified the transcription factor TOX as the master regulator of exhaustion through driving transcriptional and epigenetic reprogramming in response to chronic TCR stimulation[52,53]. To overcome local immune dysfunction, effective immunotherapies drive *de novo* peripheral immune responses through the priming of naïve CD8 T cells that proliferate, differentiate, and infiltrate the tumor. Several recent studies show that PD-1 and PD-L1 blockade drive the recruitment of new T cell clones into the tumor microenvironment that were not present locally prior to therapy[54,5556]. Together, these results demonstrate the importance of peripheral immunity in antitumor immunity.

1.4 Systemic Coordination of Immune Responses to Pathogens

Immune responses are remarkably dynamic and require coordinated interactions between many functionally distinct immune lineages, orchestrated across tissues and time. Previous work studying immune responses has been technologically limited to studying only small fragments of the immune response. However, recent work sampling peripheral blood to profile the human immune response to influenza H1N1 and primate responses to Ebola demonstrated that all immune cell lineages are engaged during an immune response and undergo dramatic shifts in cell phenotype and frequency[57,58]. Within this multi-lineage response, the most critical interaction for mediating adaptive immune responses occurs through dendritic cell priming of T cells. CD8 T cells are primed primarily by BAT3-dependent CD8$^+$ type 1 classic dendritic cells (cDC1s), whereas CD4 T cells are primed primarily by CD11b$^+$ type 2 classic dendritic cells (cDC2s)[59]. Effective priming requires recognition of peptide antigen loaded into Major Histocompatibility Complex (MHC) proteins, costimulatory molecule engagement such as CD86 and CD28, and proinflammatory cytokines to support proliferation[20]. Once CD8 T cells have been primed by cDC1s they undergo rapid proliferation and differentiation into multiple effector fates including short-lived cytotoxic cells that directly kill infected cells, and long-lived memory cells that persist after resolution of an infection and are able to initiate a faster and more potent secondary response to future challenges[60]. Elegant lineage tracing studies have shown that single T cells make very early decisions about the fate that they will ultimately acquire[61,62]. Yet the precise mechanisms for these early decisions remain unclear. Furthermore, the full scope of immune interactions, phenotypes, and frequency shifts that occur within a lymphoid organ during a response have not been studied.

The prior experience and state of the immune system dramatically shapes future responses to challenges. Altered basal cytokine levels or cellular composition and activation states are known to drive distinct secondary responses in models of chronic infection and coinfection[63–65]. Because the systemic immune state is significantly reorganized in tumor-bearing individuals, this may have functional consequences on the orchestration of new immune responses. Indeed, cancer patients often exhibit increased susceptibility to infection compared to healthy individuals[66,67]. During the ongoing 2020 SARS-CoV-2 pandemic, infected cancer patients are more likely to develop severe symptoms and ultimately death[68,69]. These observations suggest that the substantial pan-lineage phenotypic and compositional changes to the systemic immune landscape ultimately led to impaired immune responses to a secondary challenge beyond the tumor microenvironment. As an intact functional peripheral immune system is critical to the development of new antitumor immune responses as described in the previous section, it is imperative to understand how immunological decisions are made within the context the tumor-burdened state.

Recent work has begun to mechanistically dissect why the tumor-burdened immune state drives weakened peripheral secondary immune responses by using challenges that share no antigens with the initial tumor. The splenic CD8 T cell response to *Listeria monocytogenes* (*Lm*) in Pan02 pancreatic tumor-bearing mice also showed perturbed differentiation characterized by the acquisition of an exhausted fate[70]. Suppressed splenic expansion of CD8 T cells has also been observed in response to lymphocytic choriomeningitis virus (LCMV) with pre-existing B16 melanoma[71] . Vaccination of PanIN and pancreatic tumor-bearing mice with ovalbumin (OVA) and CpG also led to impaired OVA-specific CD8 T cell proliferation and differentiation in the spleen, which was linked to DC dysfunction and could be rescued by combined treatment with FLT3L and CD40 agonism to both increase DC numbers and activation, respectively[29]. In a PyMT-B6 mouse model of breast cancer, a matrigel plug containing poly I:C and OVA was used as an immunogenic secondary challenge without shared antigens to the primary tumor. Pre-existing malignancy drove significantly decreased frequency of cDC1s within the plug and the plug-draining lymph node, which then led to a reduced number OVA-specific CD8 T cells infiltrating the plug[28]. Taken together, these studies show that the innate and adaptive arms of immune responses, and specifically dendritic cell and CD8 T cell interactions do not proceed optimally in tumor-bearing mice.

Chapter 2 Systemic dysfunction and plasticity of the immune macroenvironment in cancer models

Breanna M. Allen[1,2,6], Kamir J. Hiam[1,2,6], Cassandra E. Burnett[1,2], Anthony Venida[1,3], Rachel DeBarge[1,2], Iliana Tenvooren[2], Diana M. Marquez[2], Nam Woo Cho[2,4], Yaron Carmi[5], and Matthew H. Spitzer[1,2]*

[1]Graduate Program in Biomedical Sciences, University of California, San Francisco, San Francisco, CA, USA

[2]Departments of Otolaryngology and Microbiology & Immunology, Helen Diller Family Comprehensive Cancer Center, Parker Institute for Cancer Immunotherapy, Chan Zuckerberg Biohub, University of California, San Francisco, San Francisco, CA, USA

[3]Department of Anatomy, University of California, San Francisco, San Francisco, CA, USA

[4]Department of Radiation Oncology, University of California San Francisco, San Francisco, CA, USA

[5]Department of Pathology, Sackler School of Medicine, Tel Aviv University, Tel Aviv, Israel.

[6]Co-First Author

Chapter 2 is reprinted as it appears in: Allen, B.M., Hiam, K.J., *et al.* Nature Medicine 26, 1125–1134 (2020). https://doi.org/10.1038/s41591-020-0892-6

2.1 Author Contributions

Conceptualization, B.M.A, K.J.H., Y.C., and M.H.S.; Experimental Methodology, B.M.A, K.J.H., C.E.B., A.V., R.D., I.T., D.M.M., N.W.C., Y.C., and M.H.S.; Computational Methodology, B.M.A, and M.H.S.; Investigation, all authors; Writing – Original Draft, B.M.A.; Writing – Review & Editing, all authors; Funding Acquisition, M.H.S.; Supervision, M.H.S.

2.2 Acknowledgements

We thank the UCSF Flow Cytometry Core and Stanley Tamaki for CyTOF maintenance, Drs. Mary Helen Barcellos-Hoff, Ross Levine, Hideho Okada, Edgar Engleman and Jeffrey Bluestone for cell lines, transgenic mice and reagents. We thank Drs. Lewis Lanier, Zena Werb, Mary Helen Barcellos-Hoff, and Lawrence Fong for insightful feedback. This work was supported by NIH grants DP5OD023056 and P50CA097257 (UCSF Brain Tumor SPORE Developmental Research Program), funds from the UCSF Program for Breakthrough Biomedical Research, and investigator funding from the Parker Institute for Cancer Immunotherapy to M.H.S., and by NIH grant S10OD018040, which enabled procurement of the mass cytometer used in this study.

This study makes use of data generated by NOWAC. A full list of investigators who contributed to the generation of the data is available from http://site.uit.no/nowac/. Funding for the project was provided by the European Research Council grant ERC-2008-AdG 232997. The NOWAC group is not responsible for the analysis or interpretation of the data presented.

2.3 Abstract

Our understanding of the factors governing immune responses in cancer remains incomplete, limiting patient benefit. Here, we use mass cytometry to define the systemic immune landscape in response to tumor development across five tissues in eight mouse tumor models. Systemic immunity was dramatically altered across models and time, with consistent findings in the peripheral blood of breast cancer patients. Changes in peripheral tissues differed from those in the tumor microenvironment. Mice with tumor-experienced immune systems mounted dampened responses to orthogonal challenges, including reduced T cell activation during viral or bacterial infection. Antigen-presenting cells (APCs) mounted weaker responses in this context, while promoting APC activation rescued T cell activity. Systemic immune changes were reversed with surgical tumor resection, and many were prevented by IL-1 or G-CSF blockade, revealing remarkable plasticity in the systemic immune state. These results demonstrate that tumor development dynamically reshapes the composition and function of the immune macroenvironment.

2.4 Introduction

Immunotherapy has rapidly expanded our toolkit against cancer, but a broader understanding of factors governing immune responses in cancer is required to extend clinical efficacy to all patients. Intratumoral CD8 T cells have been the main focus of cancer immunotherapies, yet recent studies demonstrate that cytotoxic T cells within the TME are irreversibly dysfunctional[51]. Several studies have shown that a systemic anti-tumor immune response is essential for immunotherapeutic efficacy[44,49,54,72–76]. However, we lack a comprehensive definition of how cancer development impacts the systemic immune state.

Several lines of evidence suggest that systemic immune perturbations occur with cancer. Peripheral granulocytic and monocytic expansion and impaired differentiation accompany tumor progression[1,10,77] along with a reduction in conventional dendritic cells[28]. Systemic effects on lymphocytes remain poorly understood. Most studies have explored anti-tumor immune responses at a single, static time point, leaving the dynamicity of the immune system during cancer development an open question. Prior immune experiences can impact responses to new stimuli by shifting basal cytokine levels, innate immune activation states, and cellular composition[64,65,78]. While many immunotherapies and vaccines seek to elicit new immune responses in cancer patients, it remains uncertain how tumor burden impacts these processes. It is also unclear whether there are lasting immune impacts after successful primary tumor clearance, though studies have associated tumor resection with a reduction in myeloid-derived suppressor cells[79,80]. Defining the functional capacity and stability of the tumor-experienced immune macroenvironment is critical for improving immunotherapies.

We used high content single-cell analysis and corresponding analytical methods to characterize the systemic immune landscape across eight commonly used mouse tumor models. These data, which are publicly available, provide a rich resource. While each tumor has unique immunological consequences, we found that three distinct breast cancer models converged on similar systemic changes. Tumors drove dynamic shifts in the organization and functional capacity of immune cells across the organism, culminating in attenuated responses to new immune challenges, while tumor resection was sufficient to revert the systemic immune landscape. These findings have implications for how and when we apply immunomodulatory agents in cancer, emphasizing the importance of strategies that are informed by preexisting alterations in the immune macroenvironment.

2.5 Results

2.5.1 Systemic immune organization is altered across multiple tumor types

We began by examining the TME across several common mouse tumor models, including genetically-engineered and transplantable syngeneic models across different mouse strains with different mutational loads, metastatic potential, variability and latency in tumor growth[81–84]. We characterized well-established, but pre-terminal tumor stages to reflect the patient populations most often treated with immunotherapies, but also to avoid the confounding impact of end-of-life processes. We utilized mass cytometry to quantify the abundance and activity state of immune cell subsets in the tumor as well as the blood, spleen, bone marrow and tumor-draining lymph nodes (Table 2-1and Figure 2-1).

The immune composition of the TME was distinct between models, varying in the degree of immune infiltration and diversity (Figure 2-2a and Figure 2-3). The predominant immune cell types were tumor-associated macrophages and other CD11b^{high} myeloid subsets, particularly in the transplantable MC38 colorectal cancer and SB28 glioblastoma models, with relatively fewer adaptive immune cells as reported in many human tumors[85]. Both transplantable LMP pancreatic cancer and genetically induced Braf^{-}Pten melanoma models showed extensive eosinophil infiltration. B16-F10 syngeneic melanoma and three models of breast cancer (transplantable cell lines 4T1 and AT3 and autochthonous MMTV-PyMT) showed less relative abundance but greater diversity in local immune cells, including B, T, and NK cell infiltration (Figure 2-2a and Figure 2-3a). Unique immune profiles were apparent across tumor types (Figure 2-2b and Figure 2-3g).

We next asked whether these tumor models also resulted in altered systemic immune states. The immune compositions of the tumor draining lymph node, bone marrow, blood, and spleen were indeed altered, with nuance in the extent of alteration and immune cell types affected (Figure 2-2c and Figure 2-3g). There was striking concordance among different models of the same tumor type (breast cancer and melanoma), shifting together across principal components. Surprisingly, SB28 glioblastoma extensively altered systemic immunity despite localization in the brain. Reporter protein expression was not responsible for systemic immune remodeling, as both the AT3 parental cell line and a derivative expressing GFP and luciferase exhibited strongly correlated systemic alterations (Figure 2-3h, $r = 0.9$, $p = 2.2e-16$). Systemic alterations also occurred in mice both with and without metastases (Figure 2-4a-e) and were tightly correlated with primary tumor size in the MMTV-PyMT model ($r = 0.8527$, $p < 0.0001$). While the majority of systemic immune remodeling could be explained by primary tumor size (78.4%), the residual values were correlated with both lung and lymph node metastases ($r = 0.5794$, $p = 0.0207$ for lung, and $r = 0.5882$, $p = 0.0185$ for lymph node). Compositional alterations in these peripheral sites did not correspond with the local immune infiltrate. Thus, tumor burden drives distinct changes in peripheral immune organization, dependent on the identity of the tumor.

We next performed Statistical Scaffold Analysis[49,86] to interrogate the impact of tumor burden in a more detailed manner, focusing initially on the spleen as a secondary lymphoid organ distal from the tumor (Figure 2-2d and Figure 2-3b-f, Methods). All models exhibited expansions in the splenic myeloid compartment, which was dominant in some, such as the three breast cancer models (Figure 2-2d and Table 2-2) but less dramatic in others, such as the two melanoma models (Figure 2-3e-f). Splenic remodeling in breast cancer was specifically characterized by increases in frequencies of neutrophils, eosinophils, and monocytes and reductions in B and T cells (Figure 2-2d). Consistency was observed across breast cancer models, which span three mouse strain backgrounds (BALB/c for 4T1, C57BL/6 for AT3, and FVB/N for MMTV-PyMT), orthotopic and autochthonous models, and a range of metastatic potential (AT3 – weakly metastatic, MMTV-PyMT – moderately metastatic, 4T1 – highly metastatic). Consistency despite model differences argues for a tumor and/or site-specific bias in systemic immune responses. Gene expression analysis of whole blood from untreated breast cancer patients and matched controls from the Norwegian Women and Cancer Study also demonstrated a marked shift in the immune state (PC1 Wilcoxon rank-sum p-value = 5.0×10^{-12}, PC2 p-value = 1.6×10^{-6}) (Figure 2-2e). Cellular enrichment analysis demonstrated increased neutrophils and decreased Th1 and CD8 T cells (Figure 2-2f). Altogether, these data suggest that tumor burden broadly disrupts immune macroenvironments, providing context to inform therapeutic manipulations designed to activate local versus systemic responses.

2.5.2 Tumor growth drives non-linear changes in immune cell frequencies over time

Tumors develop gradually, yet tumors are sampled at one developmental point in the clinic to provide prognostic information related to the immune response. We explored the dynamics of global immune remodeling during breast tumor growth, beginning with the predictable orthotopic 4T1 model before confirming results in an unrelated spontaneous model (MMTV-PyMT)**.** Absolute cell counts of tumor-infiltrating leukocytes positively correlated with tumor size, supporting a progressive immune response (Figure 2-4f, r = 0.6, p = 0.0256). Absolute spleen cell counts also increased, but cell frequencies as a percent of total leukocytes were comparable to absolute numbers per milligram of spleen (Figure 2-4g). Deep profiling of both the tumor and splenic immune compositions by mass cytometry revealed nonparametric correlations in individual cluster frequencies with time (Figure 2-5a-b), demonstrating at the single cell level that immune changes are indeed progressive. PCA of immune cell frequencies showed progressive changes across tissues over tumor growth in both 4T1 (Figure 2-5c-d) and MMTV-PyMT tumors (Figure 2-4h). Importantly, the immune profile within the TME remained distinct from those observed in peripheral sites. The draining lymph node immune composition was unique, while the spleen, blood, and bone marrow were more coordinated. Neutrophil expansion in the spleen and bone marrow, culminating in elevated circulation in blood, but lack of accumulation within the lymph node or tumor, is one feature contributing to these unique profiles (Figure 2-5d).

Progressive systemic immune responses to tumor burden were not strictly linear. The magnitude of change was non-uniform between each time point as evident by the PCA (Figure 2-5c and Figure 2-4h). While some population changes were relatively continuous, such as increasing neutrophils or decreasing CD4$^+$ T cells, many others were dynamic, like CD8$^+$ T cells and Tregs, which reciprocally expanded and contracted at distinct times in the tumor and draining lymph node (Figure 2-5d). In the spleen, myeloid expansion began by day 7 and continued to day 14, preceding the progressive decline in the T and B cells that began by day 14 (Figure 2-4i). The lymph node also changed most dramatically by day 14 (Figure 2-6a), while changes in blood were more continuous (Figure 2-6b). The bone marrow and tumor contained less mature and clearly defined cell types, with many more inter-cluster connections and individualized patterns of change over tumor growth (Figure 2-6c-d). These data demonstrate that the tumor immune response is a highly dynamic process.

2.5.3 Immune cell states are dynamically altered across immune organs with tumor growth

To understand the extent of systemic impacts on T cells, we leveraged unsupervised cell clustering to identify changes in T cell subsets, cell states, and potential cross-organ coordination of responses during tumor growth. Indeed, the T cell compartment was dramatically reorganized over both 4T1 and MMTV-PyMT tumor development (Figure 2-7a, Figure 2-8a-b). Tissues contained both unique and shared T cell subsets shifting with tumor growth (Figure 2-7b-c, Figure 2-8c-e). Blood and spleen profiles were more similar, dominated by CD4$^+$ T cells. In contrast, the tumor T cell pool had more shared subsets with the bone marrow, including an increasing double negative population and a decreasing NKT cell population (Figure 2-7c).

Demonstrating the breadth of immune reorganization in cancer, all T cell clusters changed in abundance across multiple tissues between early and late disease time points (Figure 2-7d). Of particular interest, tumor-infiltrating CD103$^+$ Tregs, described as potent suppressors of effector T cells[87], were abundant at day 7 but decreased with tumor progression (Figure 2-7e). This Treg subset expanded in the draining lymph node, suggesting that distal suppressive mechanisms may support local changes to maintain a tumor-promoting systemic state. Anti-correlated changes extended to conventional CD4$^+$ T cells, where CD44$^+$ CD90^{high} activated CD4 T cells decreased in the tumor but expanded in the lymph node (Figure 2-7f). The spleen showed the greatest change in CD44$^+$ CD27$^+$ memory CD4 T cells, which decreased with disease progression (Figure 2-7g). The blood showed increases of activated CD44$^+$ CD4$^+$ T cells expressing the CD31 adhesion receptor, which can promote T cell survival in settings of inflammation (Figure 2-7h)[88]. CD44+ CD8+ T cells expanding in the lymph node expressed Ly6C (Figure 2-7j), which can support lymph node homing of central memory T cells[89]. CD8$^+$ T cells generally expanded in the tumor, but the most dominant cluster expressed high levels of PD-1 and CD69 previously associated with T cell dysfunction (Figure 2-7i)[90,91]. To explore the extent of dysfunction, we interrogated intratumoral and splenic T cells for their expression of CD101 and CD38, two markers recently identified as evidence of permanent T cell dysfunction[51]. Late-stage tumor burden led to accumulation of CD38$^+$CD101$^+$ CD8$^+$ T cells in the tumor as expected; however, this phenotype did not emerge in the spleen (Figure 2-7k), suggesting that CD8$^+$ T cells are altered differently in the TME and periphery. Similar changes in T cell composition were observed in the MMTV-PyMT model (Figure 2-8c-h).

A similar pan-organ clustering analysis for the mononuclear phagocyte subsets, including macrophages and dendritic cells (Figure 2-9), revealed correlated and anti-correlated systemic changes in cell states with tumor progression. As expected, the tumor-infiltrating subsets were distinct from peripheral subsets and expressed high levels of PD-L1.

We specifically interrogated protein expression dynamics of PD-1 and PD-L1 , the most commonly manipulated immune checkpoints by cancer immunotherapies to facilitate T cell responses[92]. While expression of these molecules is used clinically for patient stratification, it remains unclear whether they are expressed consistently or modulated dynamically over time. We indeed found dynamic PD-1 and PD-L1 expression on infiltrating immune cells (CD45$^+$) and non-immune cells (CD45$^-$ CD31$^-$) in the TME and in the periphery of both 4T1 and AT3 breast cancer models (

Figure 2-10a- c). In fact, while the overall amount of PD-L1 expression was significantly less in the blood compared to the tumor, median leukocyte signal intensity was positively correlated between these tissues (

Figure 2-10d, r = 0.7487, p = 0.001). Both PD-1 and PD-L1 were promiscuously expressed across immune cell types, particularly within the TME (

Figure 2-10e). The most prominent cells expressing PD-L1 in the periphery were non-classical monocytes[93] and cDCs, while PD-1 was abundantly expressed on T cells, neutrophils and eosinophils. Dynamicity in PD-1 and PD-L1 expression suggests the potential for differential sensitivity to checkpoint blockade over the course of tumor development.

Changes in cellular proliferation or death rates are potential mechanisms contributing to immune composition alterations. We discovered that immune proliferation fluctuated systemically in a pattern unique to each site but was coordinated across all immune subsets within that site (Figure 2-11a-d). Changes in Ki67 and cleaved caspase-3 expression corresponded poorly with clusters that were increasing or decreasing in frequency in the spleen (Figure 2-11e). Thus, while tumor burden systemically alters proliferation and death, these processes alone likely do not account for the systemic immune alterations observed.

2.5.4 *De novo* T cell responses are impaired by pre-existing malignancy

Having established that tumor development drives an altered immune macroenvironment, we next examined whether immune responses to new challenges were affected. Type 1 immune responses are associated with strong cellular immunity and are generally thought to provide optimal anti-tumor immunity. To understand how type 1 immune responses might take place in the context of cancer, we challenged healthy or AT3 tumor-bearing mice with two well-described pathogens that induce potent type 1 immunity, lymphocytic choriomeningitis virus (LCMV) and *Listeria monocytogenes (Lm)*[94,95]. Tumor-burdened mice still cleared the pathogens from the spleen (Figure 2-12a-b), consistent with the lack of complete immunosuppression in solid tumor patients. However, the cellular immune response to infection was dramatically altered. The differentiation of effector CD8$^+$ T cells, the magnitude of CD8$^+$ T cell proliferation, and expression of the cytolytic mediator granzyme B were all significantly impaired in tumor-bearing mice after infection (Figure 2-12c-e and Figure 2-13a). These results demonstrate an unappreciated impairment of new cellular immune responses in the context of cancer.

We previously found that CD8+ T cells with markers of terminal dysfunction were only observed in the TME and not in the spleen (Figure 2-7k). Consistent with this hypothesis, splenic CD8$^+$ T cells harvested from either control or tumor-burdened animals were equally capable of producing the key effector cytokines IFNγ, TNFα, and IL-2 *in vitro* (Figure 2-13b). To test their functionality after infection, CD8$^+$ T cells from OT-I transgenic mice expressing a T cell receptor specific for ovalbumin (SIINFEKL) were isolated from control or tumor-bearing mice and transferred into recipient mice, which were infected with *Lm*-expressing ovalbumin (*Lm*-OVA). AT3 tumors still drove systemic changes in TCR transgenic mice (Figure 2-13c). OT-I CD8$^+$ T cells from control and tumor-bearing mice proliferated equivalently in control recipients at day 7 post-infection, the peak of the CD8 T cell response[94–96] (Figure 2-14a). However, when OT-I T cells were transferred into tumor-bearing recipients prior to infection, they expanded poorly, failed to induce T-bet expression associated with differentiation into effector cells, and expressed higher levels of PD-1 (Figure 2-14b). Similar results were also observed when polyclonal CD8 T cells from control or tumor-burdened mice were competitively transferred (Figure 2-14c). We found that antigen-specific central memory, effector memory, and short-lived effector CD8$^+$ T cells were less abundant in tumor-bearing mice at day 10 as well, suggesting that defects extend beyond peak proliferation and represent a fundamental impairment of *de novo* CD8$^+$ T cell responses (Figure 2-14d). Together, these results demonstrate that cell extrinsic mechanisms suppress systemic T cell function in the tumor context.

Since tumor experienced CD8$^+$ T cells in the periphery were not dysfunctional, we hypothesized that impaired APC activity earlier during infection contributes to decreased peripheral CD8$^+$ T cell activation. Dendritic cells (DCs) play a key role in orchestrating CD8$^+$ T cell responses to *Lm*[97], and evidence suggests that circulating DCs in breast cancer patients have reduced antigen presentation capacity[98]. Therefore, we quantified costimulatory molecule expression on splenic DCs 2 days post-infection. DCs from AT3 tumor-bearing animals expressed lower levels of key costimulatory molecules CD80 and CD86 and the activation marker CD83 when compared to tumor-free controls (Figure 2-14e and Figure 2-13d). DCs from tumor-bearing mice also exhibited suboptimal activation at day 7 of infection, expressing lower levels of CD80, the adhesion molecule CD54 (ICAM-1) and PD-L1 (Figure 2-13e). This result suggests that the PD-1/PD-L1 axis does not cause the T cell response impairment and indicates that alternative strategies are likely required to induce new systemic T cell activity. We therefore sought to pharmacologically boost APC activation as a plausible strategy for achieving this goal. Anti-CD40 treatment drives potent and systemic APC activation as shown by elevated CD86 and PD-L1 on splenic DCs (Figure 2-14f and Figure 2-13f). In the context of infection, anti-CD40 treatment rescued CD8$^+$ T cell proliferation in tumor-burdened animals 7 days post-infection (Figure 2-14g). We also observed significantly higher levels of activation markers CD80, CD54 and PD-L1 on DCs after treatment (Figure 2-13e), consistent with enhanced APC stimulation. In contrast, high doses of IL-12 or treatment with anti-CTLA-4 failed to rescue T cell proliferation (Figure 2-14g and Figure 2-13g), suggesting that T cell targeted interventions alone are not sufficient. These experiments demonstrate that APCs fail to drive optimal new T cell responses in the context of tumor burden.

2.5.5 Tumor resection reverses changes in systemic immune organization and responsiveness

Given that defects in T cell activity were reversed after removal from a tumor-burdened context, we asked whether tumor clearance was sufficient to revert changes in systemic immunity. We surgically resected tumors when systemic changes were evident across sites and allowed mice to recover from surgery for 14 days to mitigate immune confounders from wound healing.

We carefully tracked both local recurrence and metastatic outgrowth by bioluminescent imaging. Successful tumor resection reversed changes in systemic immunity in the AT3 and 4T1 breast cancer and the MC38 colorectal cancer models (Figure 2-15a). Splenic immune cluster frequencies and proliferative behavior became comparable to control animals (Figure 2-15b and c, and Figure 2-16a-c). Successful resection restored compositional changes in spleen immune frequencies and T cell clusters; however, local recurrence in the AT3 model and overt lung metastasis in the 4T1 model led to intermediate phenotypes in the systemic immune state (Figure 2-15d and e, and Figure 2-16d and f-g). Local recurrence induced changes in the spleen comparable to primary tumors, but the composition of T cells was less dramatically altered. Lung metastasis induced more moderate changes, suggesting that systemic immune perturbations are not primarily the consequence of disseminated metastases. Finally, we interrogated DC and T cell responses 7 days after *Lm*-OVA infection and observed higher CD86 and PD-L1 expression on DCs in successfully resected mice (Figure 2-16h), and both T cell proliferation and Granzyme B production were restored (Figure 2-15f-g). Local recurrence mitigated this rescue. Thus, changes in the immune macroenvironment, unlike those of T cells in the TME, are highly dependent on ongoing tumor burden and are reversible upon effective tumor clearance.

Finally, we investigated circulating cytokine levels to define potential mediators of tumor-driven systemic immune remodeling. We reasoned that candidate factors would be elevated in the serum of AT3 tumor-burdened mice, reduced in successfully resected animals, and elevated again with local recurrence, or vice versa. We found that levels of the inflammatory cytokines IL-1α and G-CSF followed this pattern (Figure 2-16i). Notably, recent studies have implicated G-CSF as a driver of myeloid-derived suppressor cell and neutrophil expansion in preclinical models and cancer patients[10,13,99]. While IL-1β has been shown to promote tumor development locally in the TME, the role of IL-1α is less well understood, though it is elevated human breast cancers[100–102]. Consistent with the hypothesis that tumor-secreted factors contribute to systemic immune remodeling, G-CSF and IL-1α, but not IL-1β, were produced by AT3 cancer cells *in vitro* (Figure 2-16j). We next treated mice with IL-1 and G-CSF blocking antibodies starting 5 days after tumor initiation, prior to most systemic immune changes. We also investigated the potential systemic impacts of TGFβ, a pleiotropic cytokine known to play key roles in shaping the TME, including immune cell exclusion and immunosuppression[103,104]. Both IL-1 and G-CSF blockade significantly abrogated systemic immune remodeling while TGFβ blockade had no effect (Figure 2-15h and Figure 2-16e). IL-1 and G-CSF blockade reduced splenic neutrophils and less mature CD11b+ myeloid cells (Figure 2-15i). Notably, IL-1 blockade also significantly reduced circulating levels of G-CSF, suggesting that IL-1 may act upstream to promote G-CSF production (Figure 2-16k), consistent with *in vitro* data from human tumor cell lines[105]. IL-1 blockade was additionally sufficient to reduce tumor effects on the splenic T cell composition, preventing the observed reductions in naïve and central memory CD8 T cells (Figure 2-15j-k). Thus, circulating IL-1α and G-CSF are critical mediators of tumor-driven systemic immune remodeling in this context.

2.6 Discussion

This study constructs a comprehensive landscape of the immune macroenvironment in cancer, revealing a systemic immune context to consider when targeting immune behavior therapeutically. Strong pre-existing T cell activity is associated with clinical benefit from currently available immunotherapies, but many cancer patients likely require the priming of new antitumor immune responses. However, the ability of a tumor-burdened immune system to establish new responses is poorly defined[71,106,107]. Cancer patients are more susceptible to opportunistic infections and mount less effective responses to vaccines[108,109], though the relative contributions of tumor driven systemic disruption and cytotoxic cancer therapies are debated. Here, we show that systemic immunity is disrupted to varying degrees across tumor types. Systemic immune alterations in breast cancer impair new immune responses, even to highly immunogenic pathogens that do not share tumor antigens. This challenges the idea that T cell dysfunction in cancer is limited to tumor-specific T cells experiencing chronic antigen exposure. Our data reveal impairment in the initial coordination of a T cell response by APCs, impacting T cell proliferation and differentiation. Impaired type 1 immune responses represent a fundamental, but previously unappreciated, obstacle for effective immunotherapy. These results, alongside promising clinical results of CD40 agonism in pancreatic cancer[110], strongly support combinatorial therapeutic strategies that include APC activation.

This work further reveals remarkable plasticity in the systemic immune state, as successful tumor resection largely reverted systemic immune disruptions. Influenced by physiological context, immunotherapies may have different consequences when applied pre- or post-operatively. These studies show that the immune macroenviornment in cancer is highly manipulatable, warranting further studies in cancer patients. Prior studies have connected systemic changes with relapse in breast cancer patients, showing altered immune gene signatures in uninvolved lymph nodes and blood of patients with metastatic versus non-metastatic disease[111] and that circulating CD45RA$^-$Foxp3^{high} Tregs predict future relapse[41]. In breast tumor models, we show that the primary tumor is a primary driver of systemic immune reorganization, but that lung and lymph node metastasis are also associated with additional subtle changes. Future work to understand systemic immune alterations across cancer patients could inform prognosis and optimal therapy.

Our study lays the foundation for detailed studies of specific tumor macroenvironments to match our detailed understanding of tumor microenvironments in mouse tumor models and patients. Building a complete understanding of systems-level immunity in cancer should further our ability to drive effective and rationally-designed anti-tumor immune responses in all cancer patients.

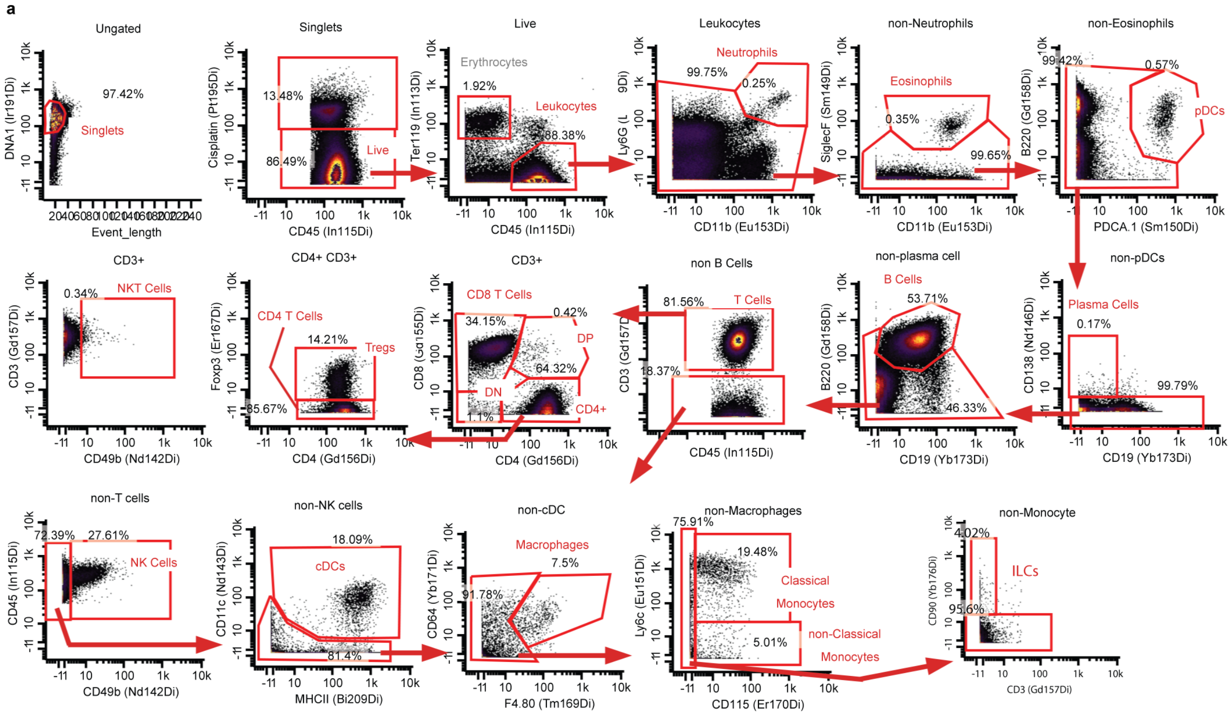

Figure 2-1: Main mass cytometry gating strategy
a, Main gating strategy for identifying major immune cell populations from mass cytometry datasets.

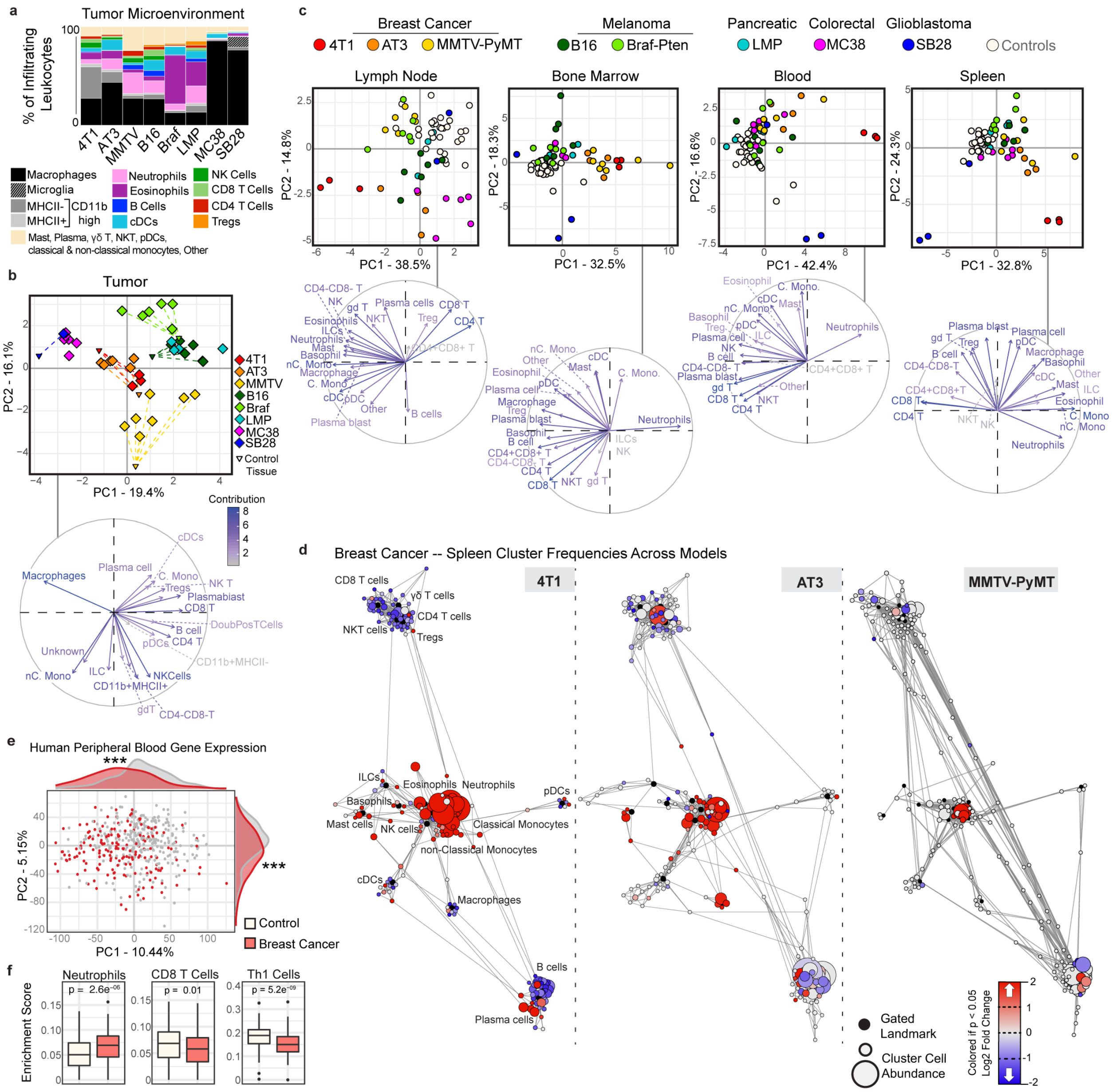

Figure 2-2: The systemic immune landscape is remodeled across tumor models.
a, Composition of tumor immune infiltrates across late stage mouse models, identified by manual gating (n = 3 independent animals for 4T1; n = 6 AT3; n = 7 MMTV-PyMT; n = 6 B16; n = 6 Braf-Pten; n = 4 LMP; n = 6 MC38; n = 1 SB28; n = 30 Controls). **b-c**, Principal component analysis (PCA) and corresponding vector plot of individual contributions for the tumor infiltrating immune frequencies (**b**), and the log2 fold change of immune frequencies for the tumor draining lymph node, bone marrow, blood, and spleen (**c**) identified manually (n = 3 for SB28, otherwise as in panel (a)) **d**, Scaffold maps of spleen immune frequencies in breast tumor models (4T1, AT3, and MMTV-PyMT). Black nodes represent canonical cell populations identified manually. Other nodes reflect unsupervised clustering of leukocytes. Nodes are arranged by similarity using a force-directed graphing algorithm (see Methods). Red denotes populations significantly higher in frequency in tumor-burdened animals compared to controls; blue denotes significantly lower

frequency. For significant nodes ($q < 0.05$ by significance analysis of microarrays), the degree of coloring reflects log2 fold change (n as in panel (a)). **e-f**, PCA (**e**) and significant immune changes by cellular enrichment analysis (**f**) from human whole blood gene expression, comparing breast cancer patients ($n = 173$) and matched controls ($n = 281$), p*** <0.001 by two-sided Wilcoxon rank-sum test with Benjamini-Hochberg correction. Box plots: center line, median; box limits, upper and lower quartiles; whiskers, 1.58x interquartile range / sqrt(n); points, outliers.

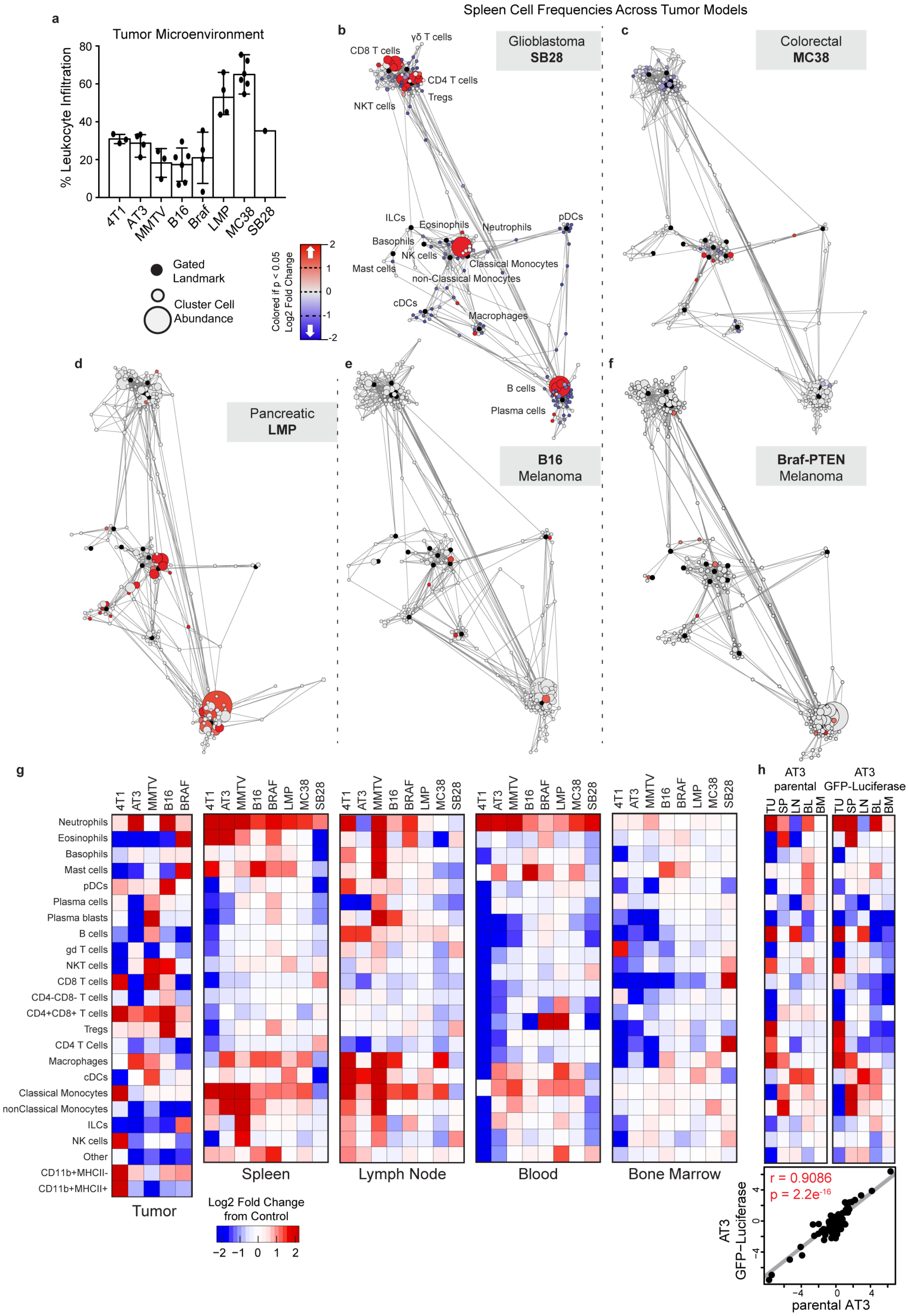
a
Tumor Microenvironment
% Leukocyte Infiltration
0
20
40
60
80
4T1
AT3
MMTV
B16
Braf
LMP
MC38
SB28
Gated Landmark
Cluster Cell Abundance
Colored if p < 0.05
Log2 Fold Change
2
1
0
-1
-2
Spleen Cell Frequencies Across Tumor Models
b
Glioblastoma
SB28
γδ T cells
CD8 T cells
CD4 T cells
Tregs
NKT cells
ILCs
Eosinophils
Neutrophils
pDCs
Basophils
NK cells
Classical Monocytes
Mast cells
non-Classical Monocytes
cDCs
Macrophages
B cells
Plasma cells
c
Colorectal
MC38
d
Pancreatic
LMP
e
B16
Melanoma
f
Braf-PTEN
Melanoma
g
Neutrophils
Eosinophils
Basophils
Mast cells
pDCs
Plasma cells
Plasma blasts
B cells
gd T cells
NKT cells
CD8 T cells
CD4-CD8- T cells
CD4+CD8+ T cells
Tregs
CD4 T Cells
Macrophages
cDCs
Classical Monocytes
nonClassical Monocytes
ILCs
NK cells
Other
CD11b+MHCII-
CD11b+MHCII+
4T1
AT3
MMTV
B16
BRAF
LMP
MC38
SB28
Tumor
Spleen
Lymph Node
Blood
Bone Marrow
Log2 Fold Change from Control
−2
−1
0
1
2
h
AT3 parental
AT3 GFP-Luciferase
TU
SP
LN
BL
BM
r = 0.9086
p = 2.2e-16
AT3 GFP−Luciferase
parental AT3
-4
0
4

Figure 2-3: Systemic immunity is distinctly remodeled across tumor types.
a, Relative abundance of total leukocytes infiltrating the TME across eight tumor models. **b-f**, Scaffold maps of spleen cell frequencies across five distinct tumor models, SB28 glioblastoma (**b**), MC38 colorectal (**c**), LMP pancreatic (**d**), B16 melanoma (**e**), and Braf-PTEN melanoma (**f**), comparing late stage tumor burden to their respective health littermate controls. **g**, Heatmaps of the log2 adjusted fold change in bulk immune cell frequencies across all five tissues, where relevant, across all models. **h**, Heatmaps of the log2 adjusted fold change in bulk immune cell frequencies comparing the parental AT3 and engineered AT3 expressing reporters GFP and Luciferase, with cell labels in g. Lower inset shows linear correlation between these systemic immune features.

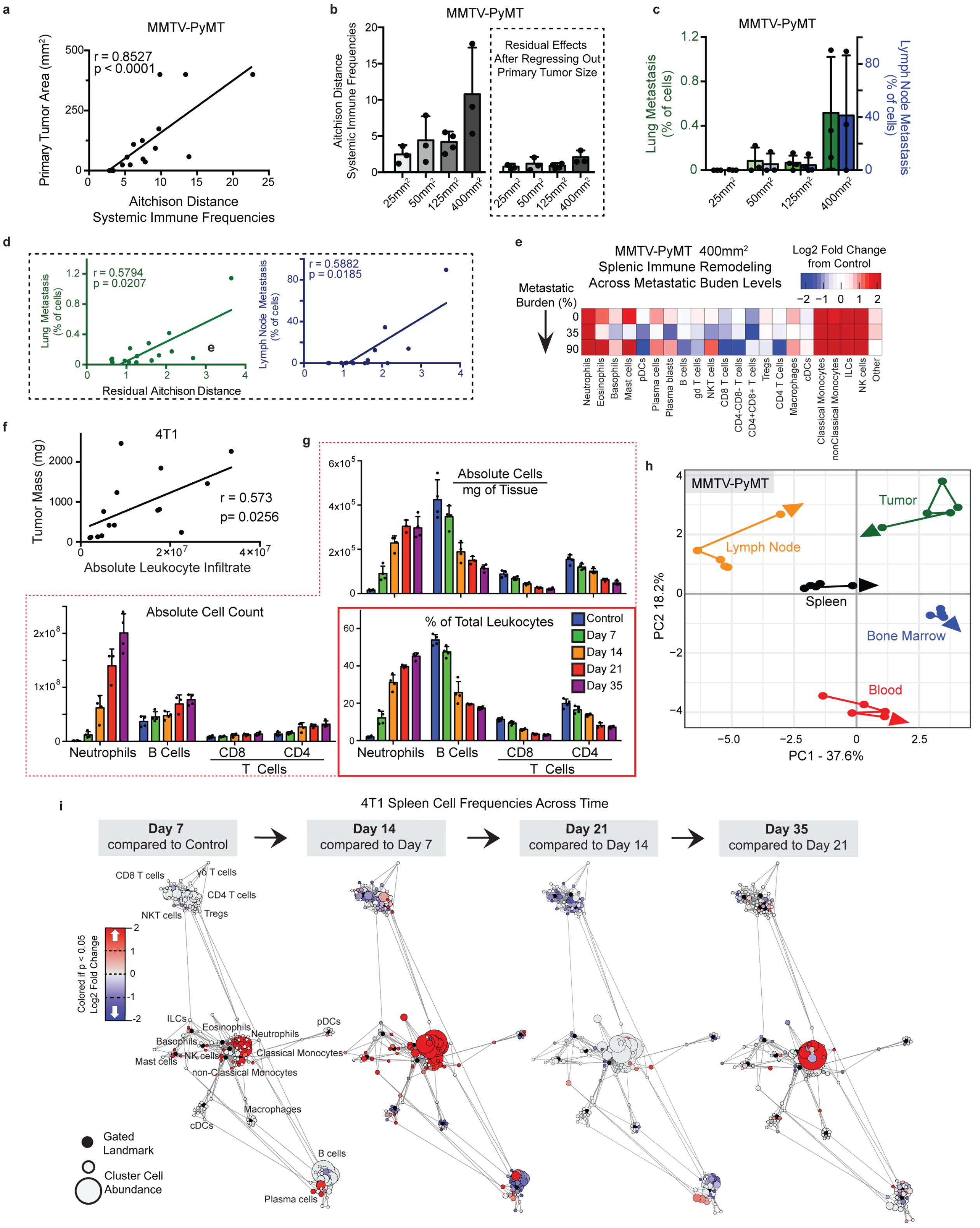

Figure 2-4: Systemic immunity is distinctly remodeled over tumor development.
a, Pearson correlation between MMTV-PyMT primary tumor size and change in systemic immune composition, measured as Aitchison distance. **b**, Degree of systemic immune change by Aitchison

distance over tumor growth (left) and after removing the contribution of primary tumor size by linear regression (right). **c**, Percent of PyMT expressing metastatic cancer cells in the lung (green) and primary draining lymph node (blue). **d**, Pearson correlation between lung or lymph node metastasis and the residual changes in systemic immune composition after regressing out primary tumor burden. **e**, Heatmap of the log2 adjusted fold change in bulk spleen immune cell frequencies for each 400mm2 tumor-bearing mouse, ranging from 0 to high metastatic disease. **f**, Pearson correlation between tumor mass and absolute number of infiltrating leukocytes in 4T1 breast tumors. **g**, Spleen immune absolute cell counts, adjusted absolute cell counts per mg of tissue, and unadjusted immune frequencies at each time point for neutrophils, B cells and T cells of the 4T1 breast tumor model. **h**, PCA of relative immune cell frequencies from each major immune tissue over time in the MMTV-PyMT breast tumor model. Vectors designate progression from control (first point) to 25 mm2, 50mm2, 125mm2, and 400mm2 (last point, arrowhead). **i**, Scaffold maps of immune cell frequencies in the spleen at each time point of 4T1 tumor burden, colored by log2 fold change in frequency compared to the previous time point.

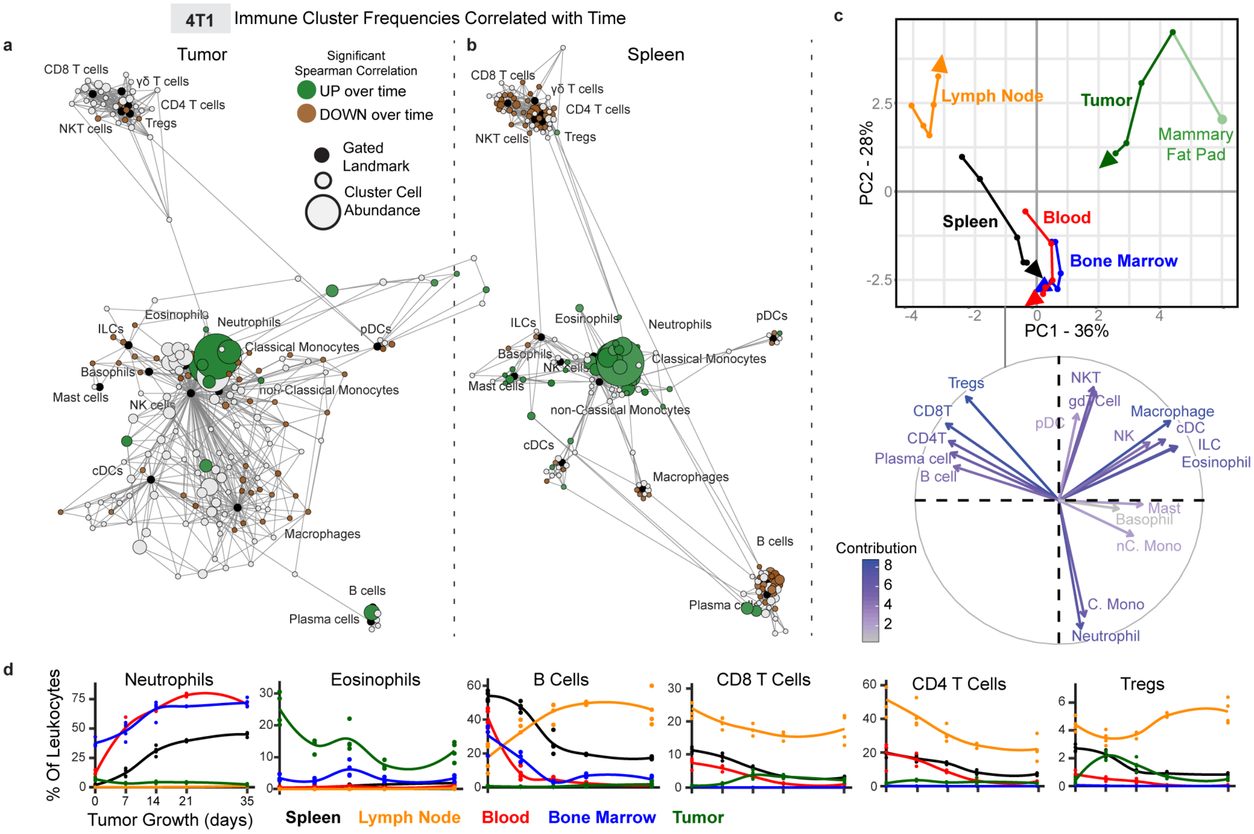

Figure 2-5: The systemic immune landscape is remodeled progressively with tumor development.
a-b, Scaffold maps of 4T1 tumor (**a**) and spleen (**b**) cell frequencies colored by significant Spearman correlation with time (across day 0, 7, 14, 21 and 35), $p < 0.05$ by two-sided t-test with Benjamini-Hochberg correction. Green denotes positive correlation, and brown denotes negative correlation. **c**, PCA and corresponding vector plot of contributions for immune cell frequencies from each immune tissue over 4T1 breast tumor growth. Vectors designate progression from control day 0 (first point) to day 7, 14, 21, and 35 (last point, arrowhead). **d**, Curves of mean cell frequencies across time from a subset of immune cell types contributing to c, colored by tissue corresponding with c. All panels from one experiment, n = 3 independent animals for day 21 and n = 4 for all other timepoints.

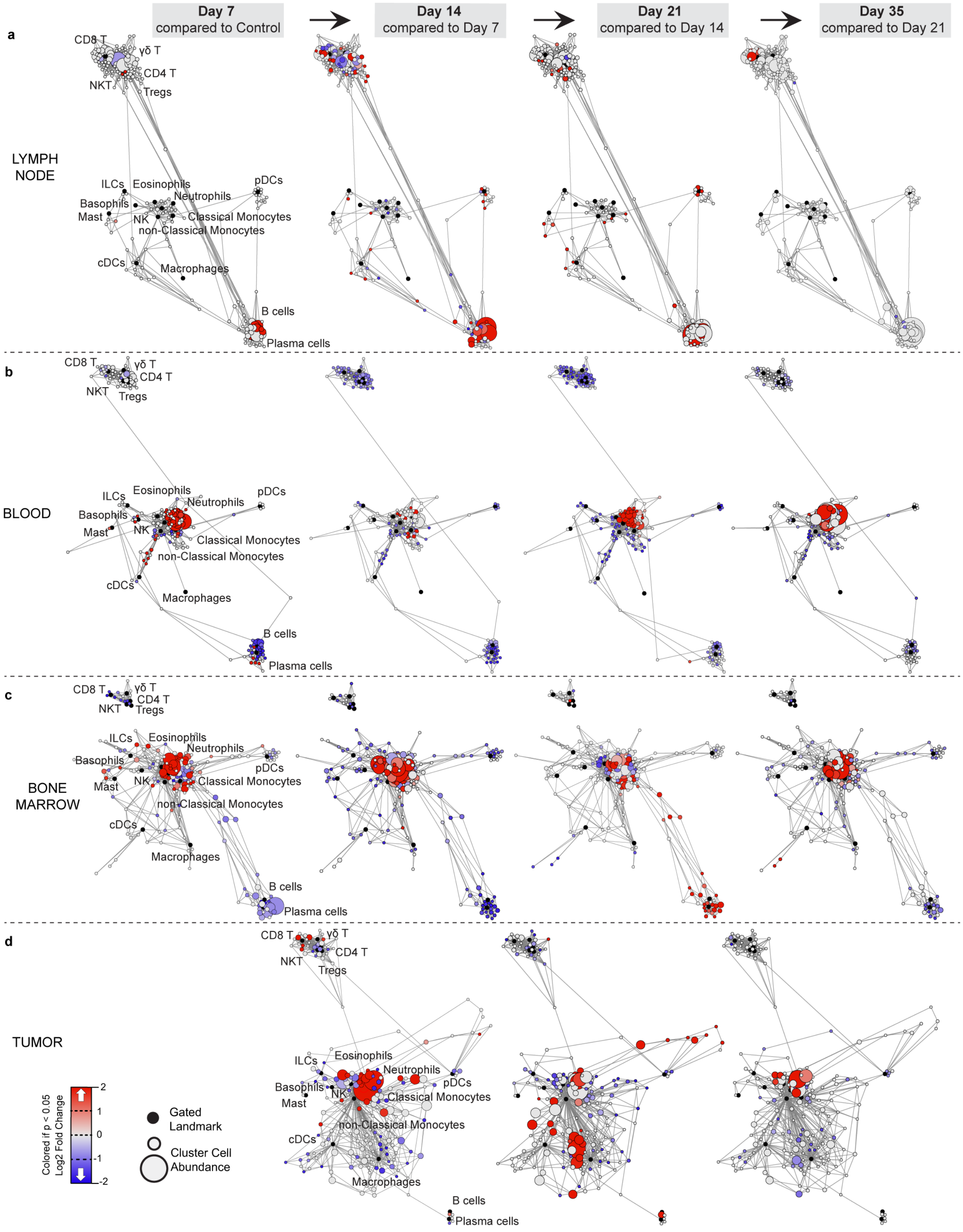

Figure 2-6: Immunity is distinctly remodeled by compartment over tumor development. **a-d**, Scaffold maps of immune cell frequencies over 4T1 tumor progression in the tumor draining lymph node (**a**) blood (**b**), bone marrow (**c**), and tumor (**d**), colored by fold change relative to the previous time point.

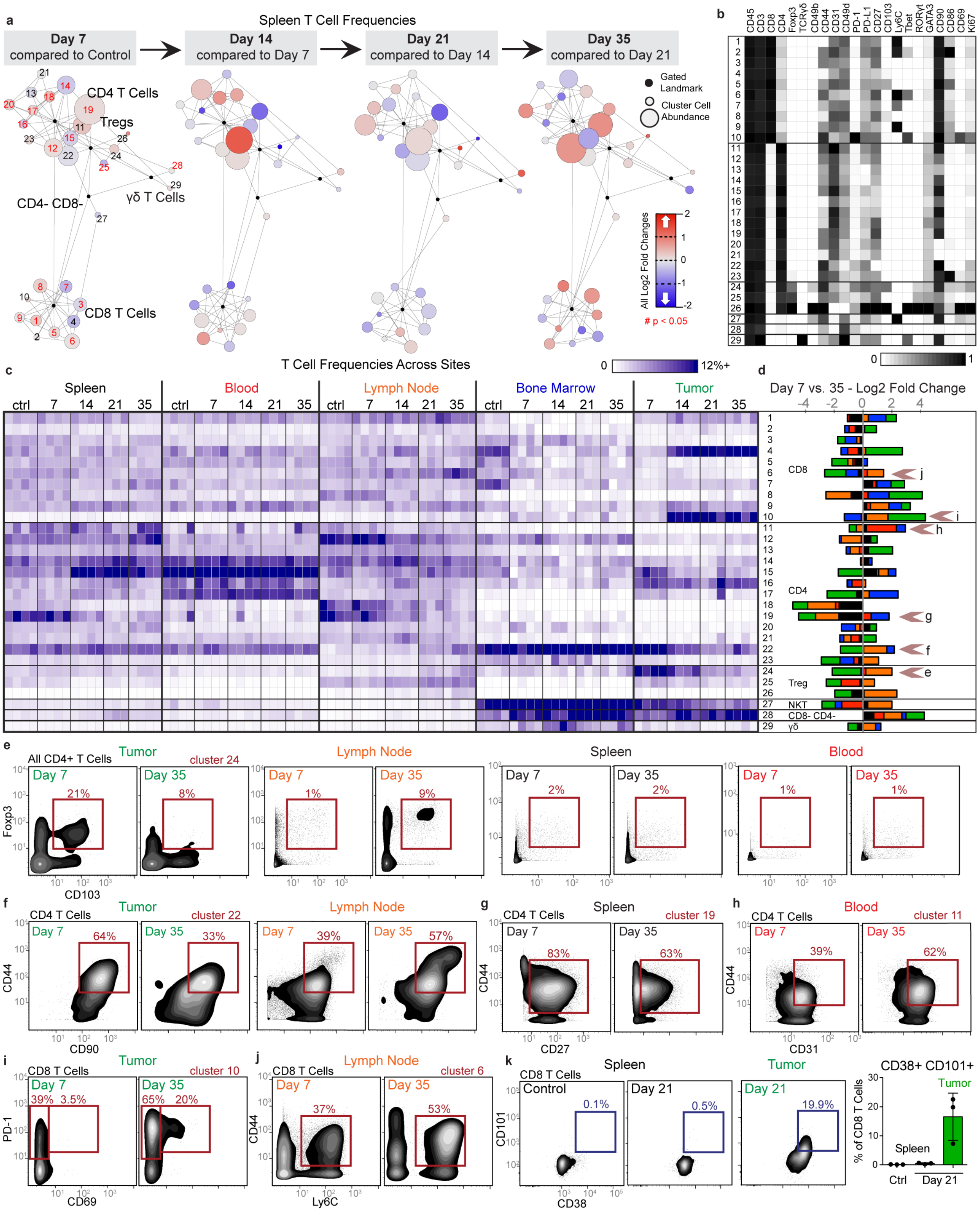

Figure 2-7: Tumor burden progressively changes the systemic T cell composition.
a-d, CD3+ CD11b- leukocytes from all tissues from healthy and 4T1 tumor-burdened animals at progressive time points. **a**, Scaffold maps of the T cell cluster frequencies in the spleen at each disease stage, all colored by log2 fold change in frequency. Clusters with significant change over

time are highlighted in red in the first map, q < 0.05 by multiclass significance analysis of microarrays. **b**, Heatmap of the protein expression defining each T cell cluster, column normalized to each protein's maximum positive expression. **c**, Heatmap of each T cell cluster frequency, by row, in each site and across the individual 3-4 animals per time point. **d**, Stacked bar plot of the log2 fold change in cluster frequency between early (day 7) and late (day 35) disease stage, colored by tissue. **e-j**, Representative scatter plots of key proteins defining T cell clusters that change in frequency in the designated tissues between early and late disease stage for Tregs (**e**), CD4 T cells (**f-h**), and CD8 T cells (**i-j**). **k**, Representative scatter plots and quantification of CD101+ CD38+ dysfunctional CD8 T cells in the spleen and tumor of health or day 21 tumor-burdened animals. All panels from one experiment, n = 3 independent animals for day 21 and n = 4 for all other timepoints. Barplot: centre, mean; whiskers, standard deviation.

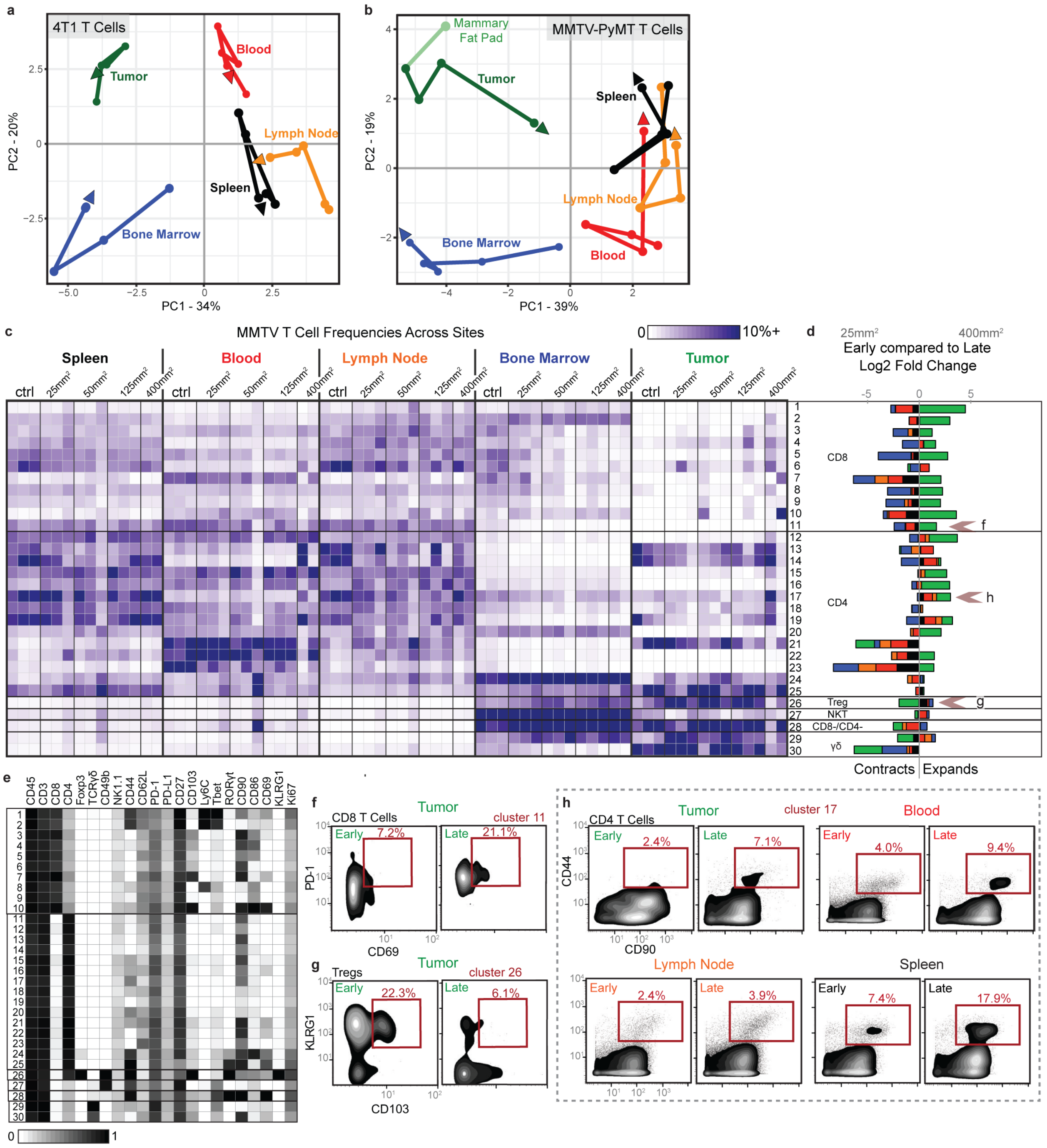

Figure 2-8: Tumor growth shifts the systemic T cell composition across models.
a-b, PCA of T cell cluster frequencies across lymphoid tissues over tumor development for the 4T1 (**a**) and MMTV-PyMT (**b**) breast tumor models. Vectors designate directional progression from control (first point) to late stage disease (last point, arrowhead). In **a**, tumor time points include day 7, 14, 21, and 35 after 4T1 cancer cell transplant. In **b**, tumor time points include tumor sizes of 25 mm^2, 50 mm^2, 125 mm^2, and 400 mm^2. **c-e**, CD3+ CD11b- leukocytes from all tissues clustered together from healthy and MMTV-PyMT tumor-burdened animals at progressive tumor sizes. **c**, Heatmap of each T cell cluster frequency, by row, in each site and across the individual 2-3 animals per time point. **d**, Stacked bar plot of the log2 fold change in cluster

frequency between early (25 mm^2) and late (400 mm^2) disease time points, colored by tissue. **e**, Heatmap of the protein expression defining each T cell cluster, column normalized to each protein’s maximum positive expression. **f-h**, Representative scatter plots of key proteins that define T cell clusters changing in frequency in the designated site between early and late disease stage for CD8 T cells (**f**), Tregs (**g**), and CD4 T Cells (**h**).

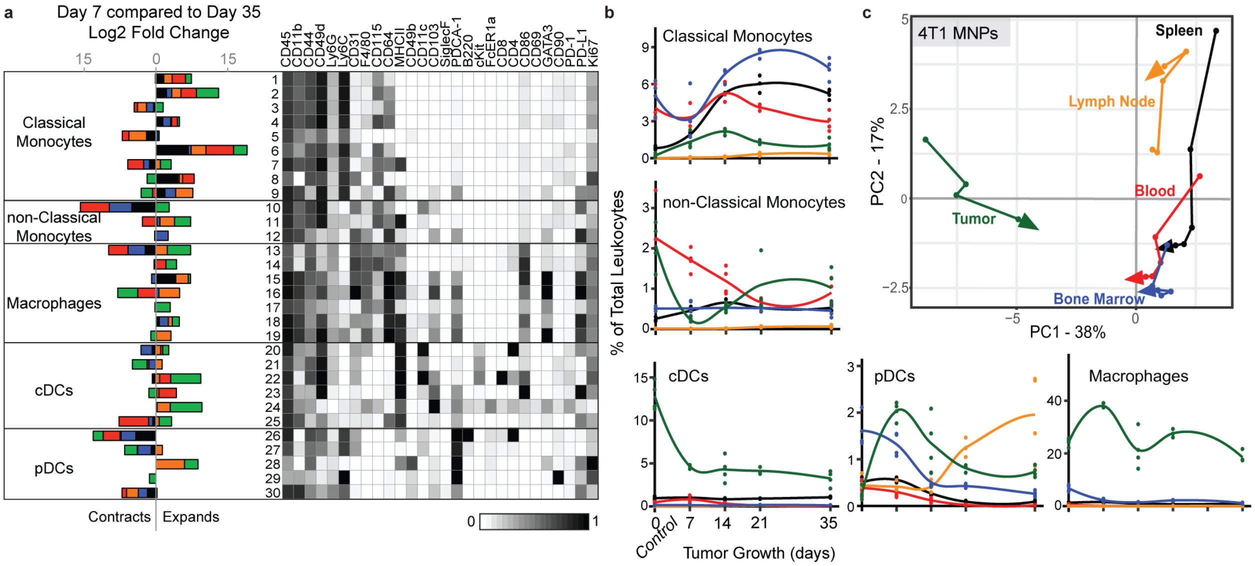

Figure 2-9: Tumor growth shifts the systemic mononuclear phagocyte composition.
a, CD3- CD19- leukocytes from all tissues clustered together from healthy and 4T1 tumor-burdened animals at progressive time points. Left, stacked bar plot of the log2 fold change in cluster frequency between early (day 7) and late (day 35) times points, colored by tissue. Right, heatmap of the protein expression defining each cluster, column normalized to each protein's maximum positive expression. **b**, Curves of the mean cell frequencies over time in the 4T1 breast tumor model from designated mononuclear phagocyte cell types, colored by tissue. **c**, PCA of the mononuclear phagocyte cell frequencies from each tissue over time in the 4T1 breast tumor model. Vectors designate progression from control (first point) to day 7, 14, 21, and 35 (last point, arrowhead). Coloring of tissues for a-c corresponds to labels in c.

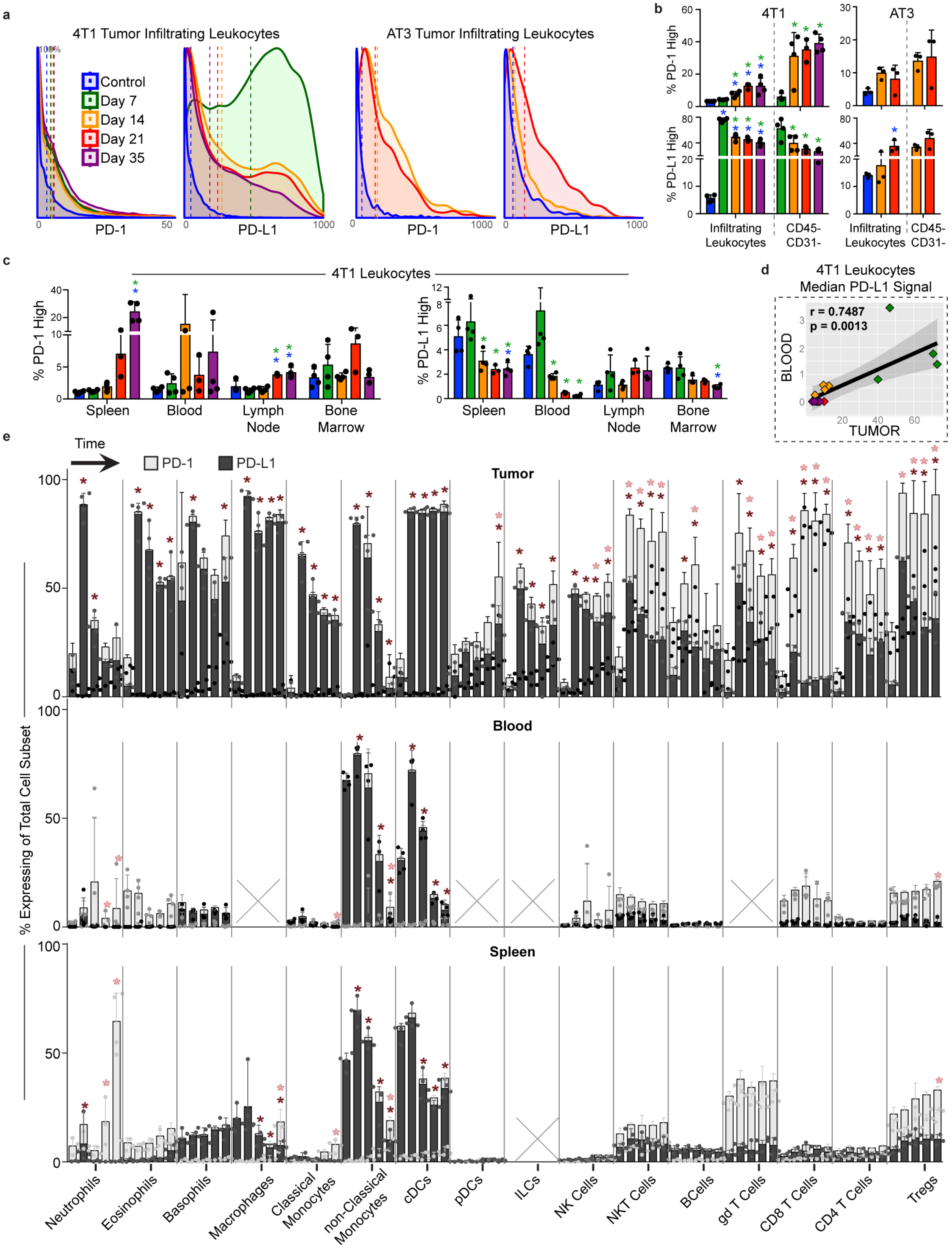
a
4T1 Tumor Infiltrating Leukocytes
AT3 Tumor Infiltrating Leukocytes
Control
Day 7
Day 14
Day 21
Day 35
100%
PD-1
PD-L1
PD-1
PD-L1
0
50
0
1000
0
1000
0
1000
b
4T1
AT3
% PD-1 High
% PD-L1 High
Infiltrating Leukocytes
CD45- CD31-
Infiltrating Leukocytes
CD45- CD31-
c
4T1 Leukocytes
% PD-1 High
% PD-L1 High
Spleen
Blood
Lymph Node
Bone Marrow
Spleen
Blood
Lymph Node
Bone Marrow
d
4T1 Leukocytes
Median PD-L1 Signal
r = 0.7487
p = 0.0013
BLOOD
TUMOR
e
Time
PD-1
PD-L1
Tumor
Blood
Spleen
% Expressing of Total Cell Subset
Neutrophils
Eosinophils
Basophils
Macrophages
Classical Monocytes
non-Classical Monocytes
cDCs
pDCs
ILCs
NK Cells
NKT Cells
BCells
gd T Cells
CD8 T Cells
CD4 T Cells
Tregs

Figure 2-10: PD-1 and PD-L1 expression is dynamic over tumor growth.
a, Distribution of PD-1 and PD-L1 signal intensities on tumor infiltrating leukocytes over time in the 4T1 or AT3 breast tumor models. Coloring of time points for a-d corresponds to legend in a. **b**, Percent of total infiltrating leukocytes (left of dashed line) or CD45-, non-endothelial cells (right of dashed line) with high PD-1 or PD-L1 expression in the 4T1 or AT3 tumor models. **c**, Percent of leukocytes with high PD-1 or PD-L1 expression over time and across tissues, 4T1 model. **d**, Pearson correlation between median PD-L1 signal intensity on blood versus tumor infiltrating leukocytes, 4T1 model. **e**, Percent of each major immune cell subset expressing high PD-1 or PD-L1 in the tumor, blood, and spleen, identified manually. Cell subsets below 0.2% of total leukocytes were not included, X. Bars ordered by time point, beginning at healthy control. Double positive PD-1/PD-L1 expression was rare and not illustrated. p*<0.05, One-Way ANOVA, with Tukey correction versus control tissue or healthy mammary fat pad (blue in b-c, fill corresponding to bar color in e), or versus day 7 (green in b-c).

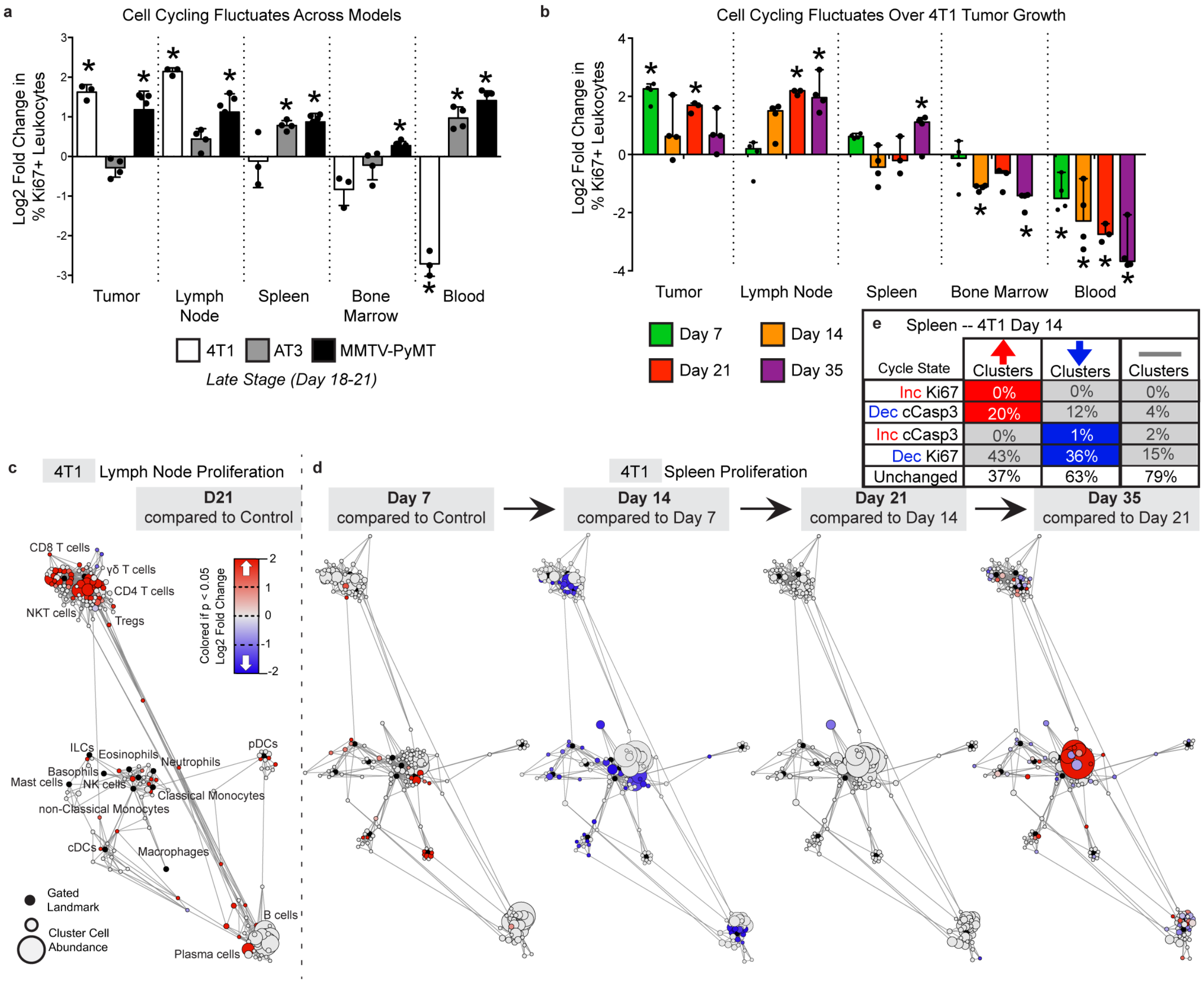

Spleen -- 4T1 Day 14

Cycle State	↑ Clusters	↓ Clusters	— Clusters
Inc Ki67	0%	0%	0%
Dec cCasp3	20%	12%	4%
Inc cCasp3	0%	1%	2%
Dec Ki67	43%	36%	15%
Unchanged	37%	63%	79%

Figure 2-11: Tumor burden induces tissue-specific changes in immune cell cycling. **a-b**, Log2 fold change in bulk Ki67 expressing leukocytes in each tissue tissues for 4T1, AT3 and MMTV breast tumors (**a**), and over 4T1 tumor progression (**b**). p*< 0.05, One-Way ANOVA, with Tukey correction versus control. **c-d**, Statistical Scaffold maps of Ki67 expression in immune cells of the tumor draining lymph node comparing control to day 21 (**c**) and the spleen over time (**d**) in 4T1 tumor burdened animals. **e**, Percent of increasing clusters (red, total of 56), decreasing clusters (blue, total of 90), or unchanged cluster that have corresponding changes in cell cycle markers Ki67 and cleaved caspase-3.

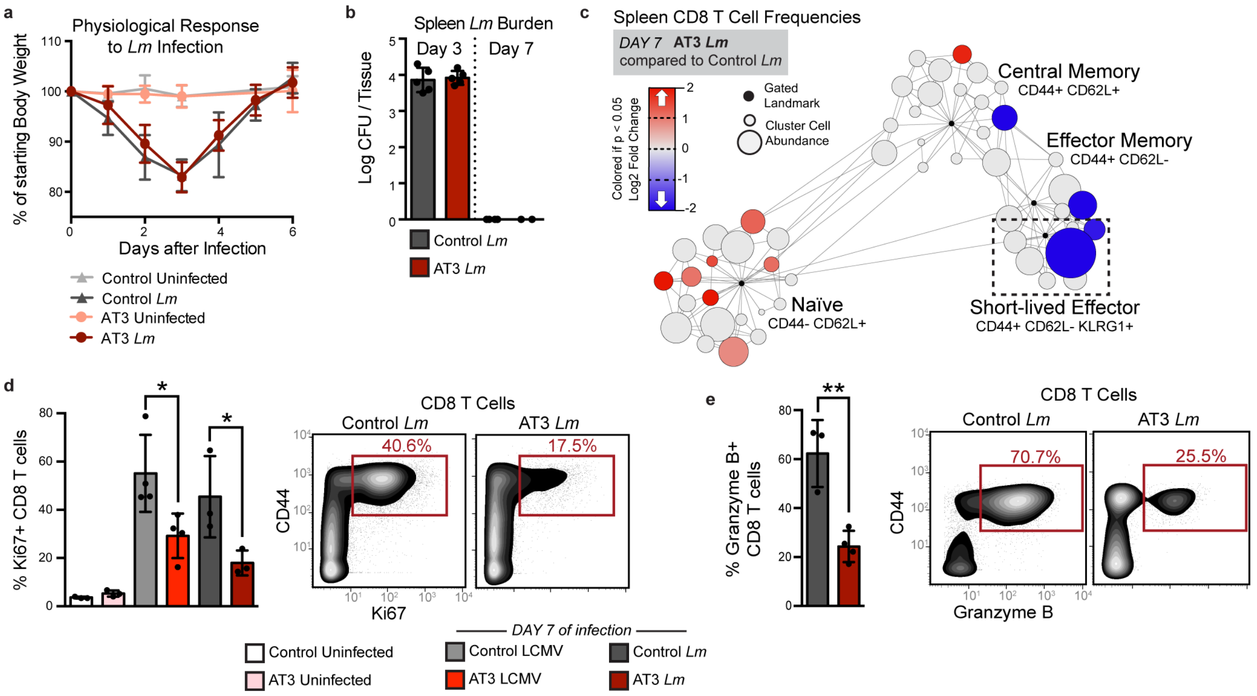

Figure 2-12: Tumor burden leads to impaired T cell responses to secondary infection. **a-b**, Fold change in body weight after Listeria monocytogenes (*Lm*) infection (n = 11 independent animals for control groups and n = 9 for AT3 groups) (**a**), and quantification of *Lm* bacterial burden (**b**) in control and AT3 tumor-burdened animals (n = 5 for day 3 groups, n = 4 for control day 8, and n = 2 for AT3 day 8). **c**, Scaffold map of CD8 T cell frequencies in the spleen in AT3 tumor-burdened mice after 7 days of *Lm* infection, colored by fold change in frequency compared to infected control mice (n = 3 uninfected, n = 3 *Lm* infected), $q < 0.05$ by significance analysis of microarrays. **d-e**, Quantification and representative scatter plots of splenic CD8+ T cell proliferation (**d**) and granzyme B production (**e**) in response to LCMV Armstrong or *Lm* in healthy or AT3 tumor-burdened animals (n = 3 uninfected, n = 4 LCMV, and n = 3 *Lm*-infected). For all barplots: $p^* < 0.05$, $p^{**} < 0.01$ by two-sided t-test; center, mean; whiskers, standard deviation.

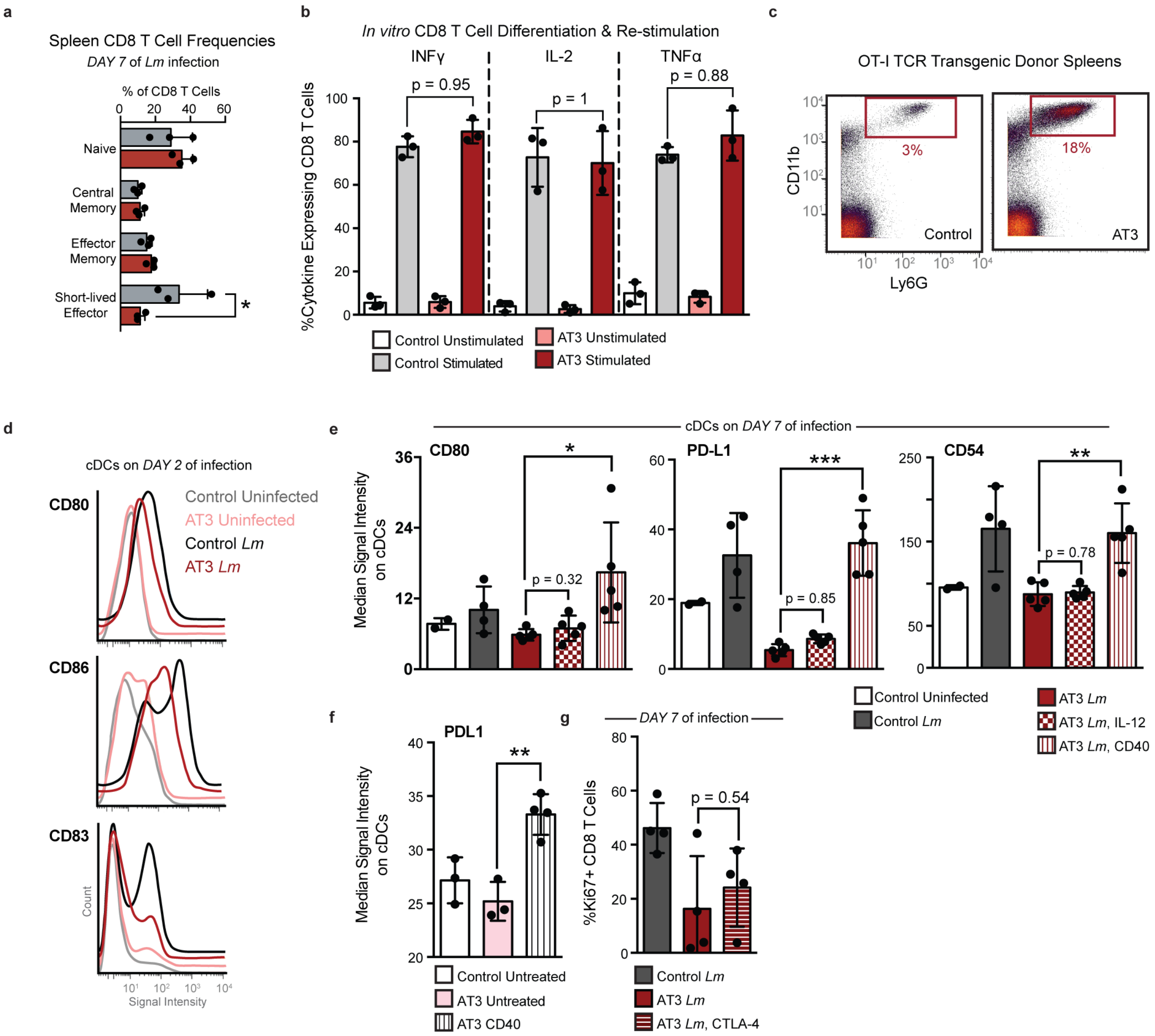

Figure 2-13: Tumor driven deficits in T cell responses are cell-extrinsic.
a, Quantification of CD8$^+$ T cell populations in the spleen of healthy or AT3 tumor-burdened mice after 7 days of *Lm* infection, Two-Way ANOVA with Bonferroni correction. **b**, Expression of inflammatory cytokines, Ifng, IL-2, and TNFa in splenic CD8 T Cells isolated from control or AT3 tumor-burdened mice after *in vitro* differentiation with CD3, CD28, and IL-2, and re-stimulation with brefeldin A and PMA and ionomycin. **c**, Scatter plots of CD11b and Ly6G showing expected neutrophilia in OT-I TCR transgenic mice with AT3 tumor burden. **d**, Histograms of CD80, CD86, and CD83 signal intensity on cDCs from healthy or AT3 tumor-burdened mice at day 2 of *Lm*-OVA infection. **e**, Median signal intensity of CD80, PD-L1 and CD54 activation markers on splenic cDCs from healthy or AT3 tumor-burdened mice compared to IL-12p70 or CD40 treatment at day 7 of *Lm*-OVA infection. **f**, Median signal intensity of PD-L1 on splenic cDCs from untreated or CD40 treated AT3 tumor-burdened (day 21) mice. **g**, Quantification of splenic CD8+ T cell proliferation in healthy, untreated or CTLA-4 treated AT3 tumor-burdened animals in response to 7 days of *Lm*-OVA infection. p*<0.05, two-tailed t-test.

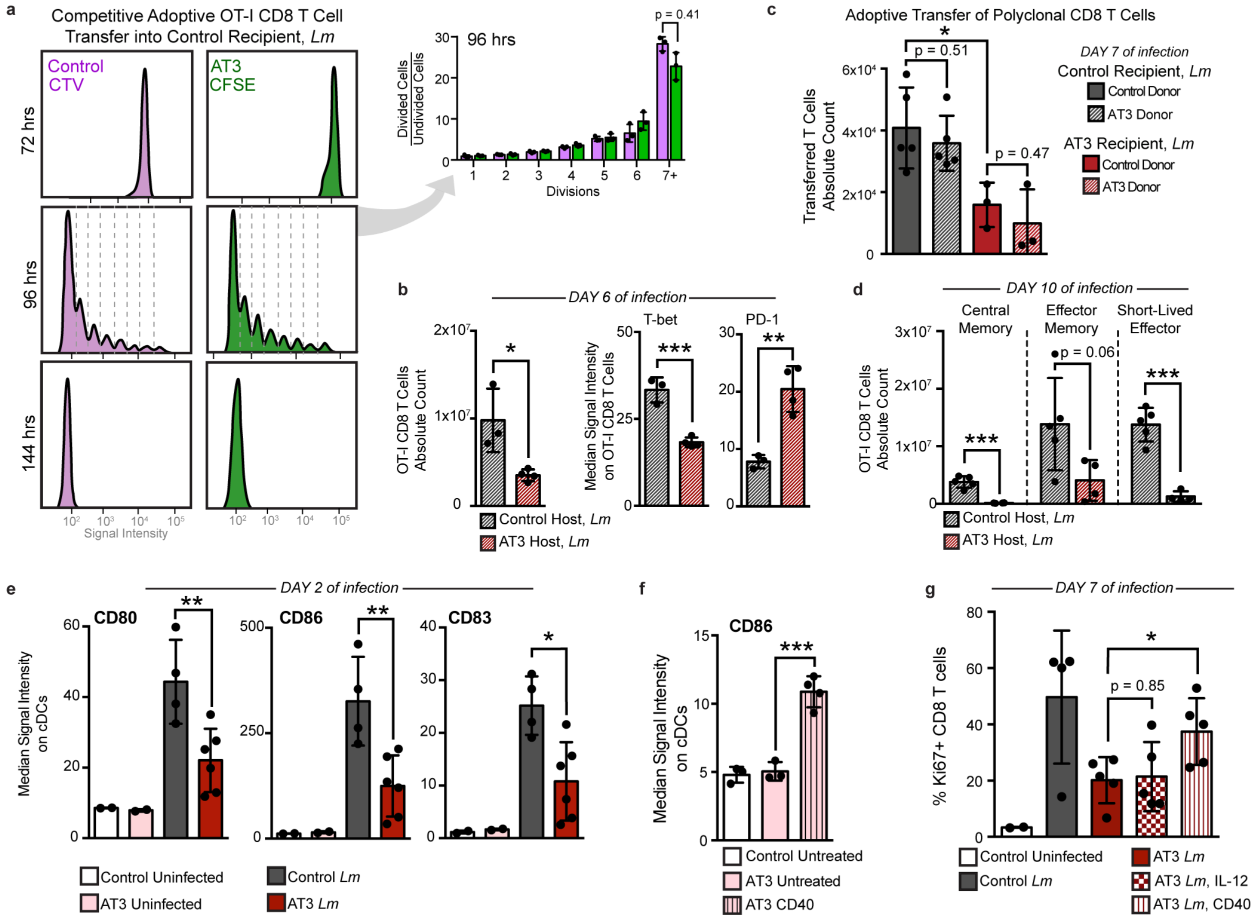

Figure 2-14: Tumor burden attenuates dendritic cell activation during secondary infection. **a**, OT-I T cell proliferation from control or tumor-burdened animals transferred into control recipients, and analyzed at 72, 96, and 144 hours post-*Lm*-Ova infection (n = 3 independent animals per group). Quantification of 96 hours. **b**, Transferred OT-I T cell counts and median signal intensity of T-bet and PD-1 at day 6 of *Lm*-OVA infection (n = 3 for control, and n = 4 for AT3 hosts). **c**, Competitively transferred polyclonal CD8 T cell counts from congenic (CD45.1+ AT3 tumor-burdened or CD45.1+CD45.2+ control) donors into CD45.2 control (n = 5) or AT3 tumor-burdened recipients (n = 4), after 7 days of *Lm* infection. **d**, CD8+ T cell subtype counts from transferred CD45.1+ OT-I T cells at day 10 of *Lm*-OVA infection (n = 5 for control, and n = 4 for AT3 hosts). **e**, Median signal intensity of CD80, CD86, and CD83 on splenic classical dendritic cells (cDCs) from healthy (n = 4) or AT3 tumor-burdened (day 28, n = 6) mice, at day 2 of *Lm*-OVA infection (n = 2 for uninfected groups). **f**, Median signal intensity of CD86 on splenic cDCs from untreated (n = 3) or CD40-treated (n = 4) AT3 tumor-burdened (day 21) mice. **g**, Quantification of splenic CD8+ T cell proliferation in healthy versus untreated, IL-12p70-treated, or anti-CD40-treated AT3 tumor-burdened animals at day 7 of *Lm*-OVA infection (n = 2 control uninfected, n = 4 control *Lm*, and n = 5 for AT3 groups). For all barplots: p* <0.05, p** <0.01, p*** <0.001 by two-sided t-test; center, mean; whiskers, standard deviation.

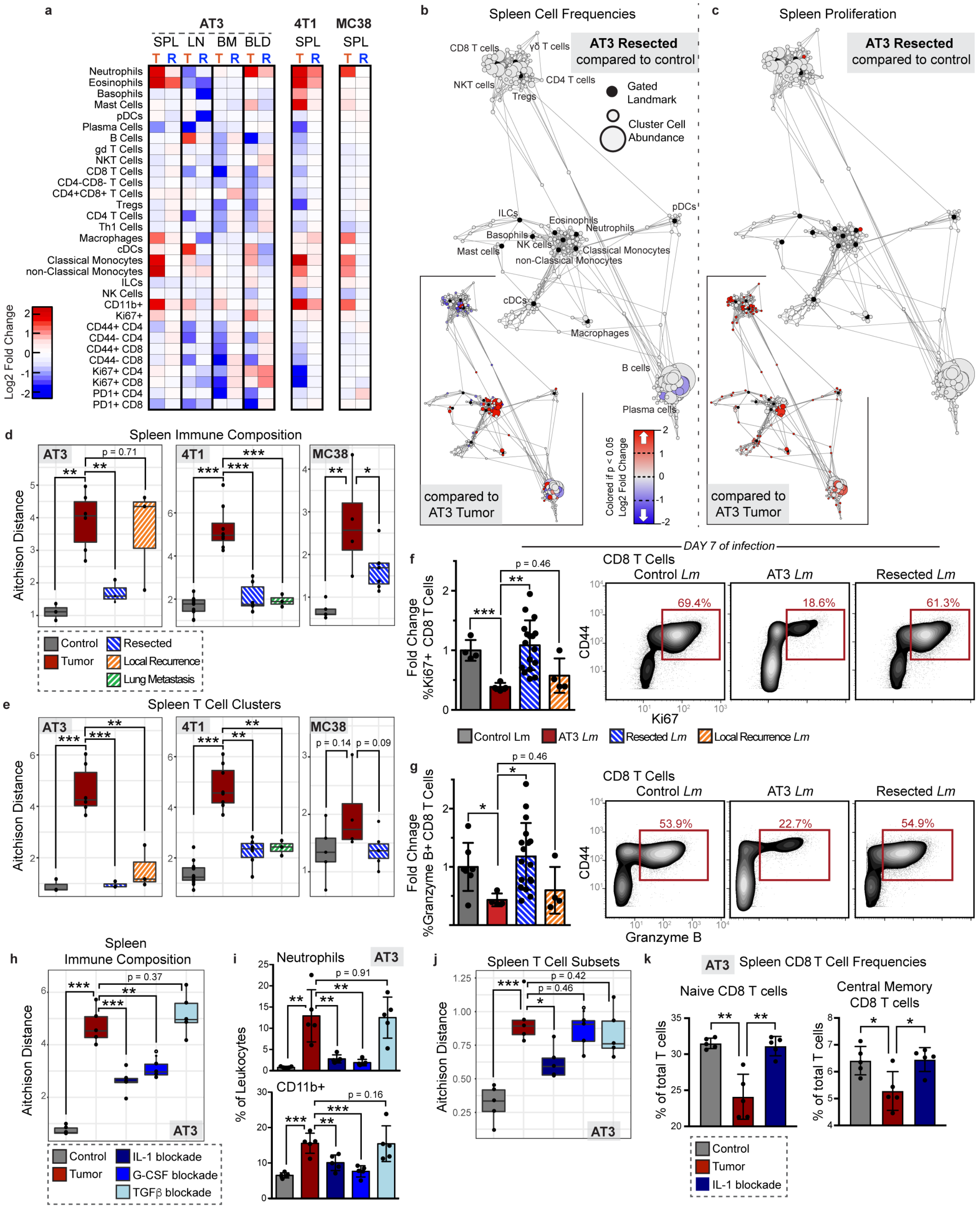

Figure 2-15: Tumor resection completely resets the systemic immune landscape.
a, Heatmaps of log2 fold changes in peripheral immune frequencies from tumor-burdened (T) or resected (R) mice. **b-c**, Scaffold maps of spleen immune frequencies (**b**) and proliferation (**c**) after AT3 resection compared to control (n = 3 per group). Insets show resected compared to tumor-

burden (n = 4), q < 0.05 by significance analysis of microarrays. **d-e**, Compositional Aitchison distances in spleen immune frequencies (**d**) or T cell cluster frequencies (**e**) from control (n = 3 for AT3, 8 for 4T1, and 5 for MC38), tumor-burdened (n = 6, 8, and 4), resected (n = 3, 6 and 6), or locally recurrent mice for AT3 and distal lung metastasis for 4T1 (n = 3 for both)(2 independent experiments for 4T1 and 1 experiment for AT3 and MC38). **f-g**, Quantification and representative scatter plots of splenic CD8+ T cell proliferation (**f**) and granzyme B production (**g**) after *Lm* infection in control (n = 4 and n = 7), AT3 tumor-burdened (n = 4), resected (n = 17), or recurrent mice (n = 4), 3 independent experiments. **h-k**, Compositional Aitchison distances of spleen immune frequencies (**h**), spleen frequencies of neutrophil (top) and undefined CD11b+ cells (bottom) (**i**), compositional Aitchison distances of T cell subset frequencies (**j**), and splenic CD8$^+$ T cell frequencies (**k**) from control, or tumor-burdened mice untreated or with IL-1, G-CSF, or TGFβ antibody blockade (n = 5 per group, from 1 experiment). All box plots: center line, median; box limits, upper and lower quartiles; whiskers, 1.58x interquartile range / sqrt(n); points, outliers. All barplots: p* <0.05, p** <0.01, p*** <0.001 by two-sided t-test; centre, mean; whiskers, standard deviation.

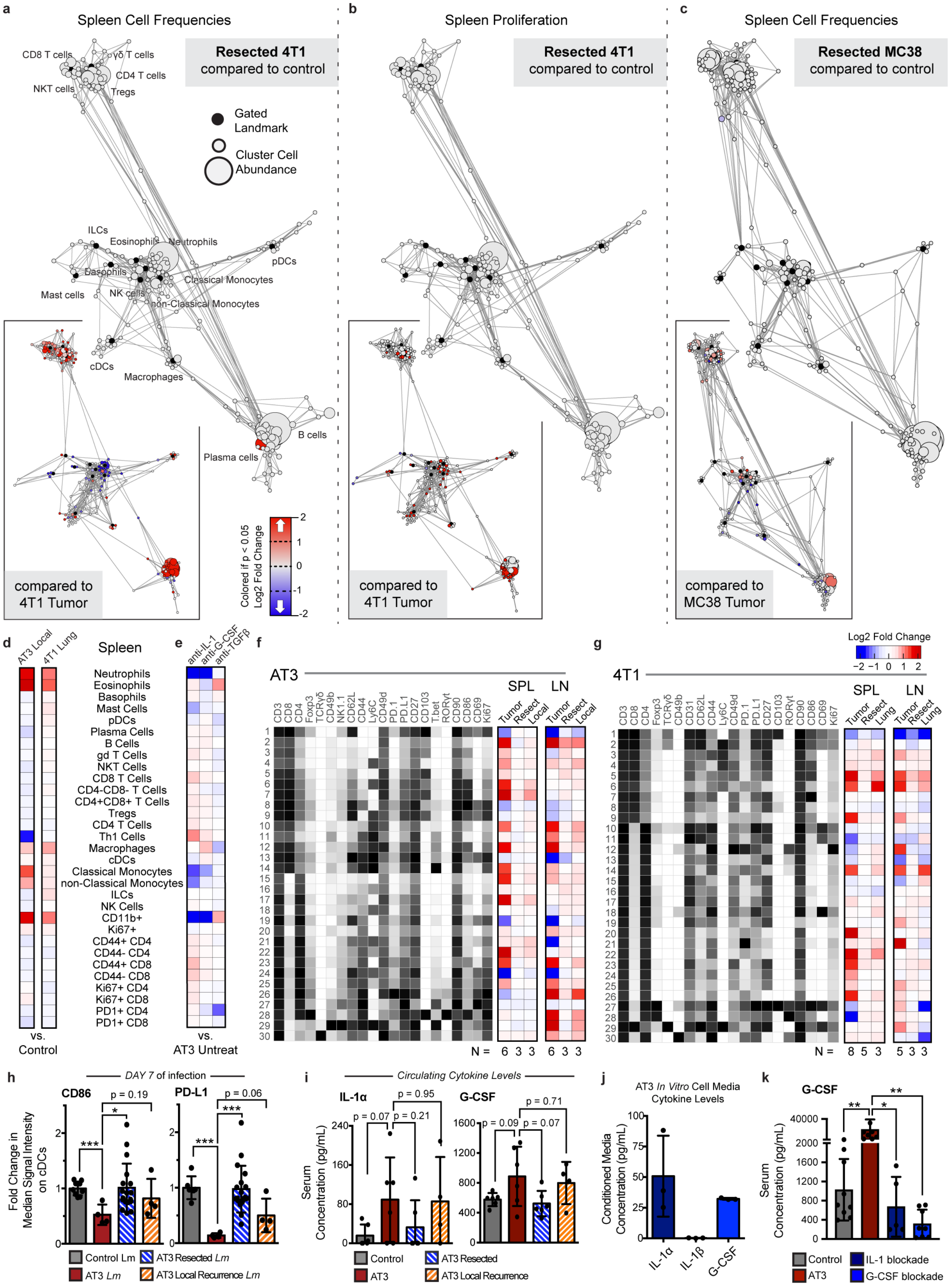
a
Spleen Cell Frequencies
Resected 4T1
compared to control
CD8 T cells
γδ T cells
CD4 T cells
NKT cells
Tregs
Gated Landmark
Cluster Cell Abundance
ILCs
Eosinophils
Neutrophils
pDCs
Basophils
Classical Monocytes
Mast cells
NK cells
non-Classical Monocytes
cDCs
Macrophages
B cells
Plasma cells
compared to 4T1 Tumor
Colored if p < 0.05
Log2 Fold Change
2
1
0
-1
-2
b
Spleen Proliferation
Resected 4T1
compared to control
compared to 4T1 Tumor
c
Spleen Cell Frequencies
Resected MC38
compared to control
compared to MC38 Tumor
d
AT3 Local
4T1 Lung
Spleen
Neutrophils
Eosinophils
Basophils
Mast Cells
pDCs
Plasma Cells
B Cells
gd T Cells
NKT Cells
CD8 T Cells
CD4-CD8- T Cells
CD4+CD8+ T Cells
Tregs
CD4 T Cells
Th1 Cells
Macrophages
cDCs
Classical Monocytes
non-Classical Monocytes
ILCs
NK Cells
CD11b+
Ki67+
CD44+ CD4
CD44- CD4
CD44+ CD8
CD44- CD8
Ki67+ CD4
Ki67+ CD8
PD1+ CD4
PD1+ CD8
vs. Control
e
anti-IL-1
anti-G-CSF
anti-TGFβ
vs. AT3 Untreat
f
AT3
CD3 CD8 CD4 Foxp3 TCRγδ CD49b NK1.1 CD62L CD44 Ly6C CD49d PD.1 PD.L1 CD27 CD103 Tbet RORγt CD90 CD86 CD69 Ki67
SPL
LN
Tumor Resect Local
1–30
N = 6 3 3 6 3 3
g
4T1
Log2 Fold Change
−2 −1 0 1 2
CD3 CD8 CD4 Foxp3 TCRγδ CD49b CD31 CD62L CD44 Ly6C CD49d PD.1 PD.L1 CD27 CD103 RORγt CD90 CD86 CD69 Ki67
SPL
LN
Tumor Resect Lung
1–30
N = 8 5 3 5 3 3
h
DAY 7 of infection
CD86
PD-L1
p = 0.19
p = 0.06
***
*
Fold Change in Median Signal Intensity on cDCs
0 1 2
Control Lm
AT3 Lm
AT3 Resected Lm
AT3 Local Recurrence Lm
i
Circulating Cytokine Levels
IL-1α
G-CSF
p = 0.95
p = 0.07
p = 0.21
p = 0.71
p = 0.09
p = 0.07
Serum Concentration (pg/mL)
0 80 160 240
0 400 800 1200 1600
Control
AT3
AT3 Resected
AT3 Local Recurrence
j
AT3 In Vitro Cell Media Cytokine Levels
Conditioned Media Concentration (pg/mL)
0 25 50 75 100
IL-1α
IL-1β
G-CSF
k
G-CSF
**
*
**
Serum Concentration (pg/mL)
0 400 800 1200 1600 2000 40000
Control
AT3
IL-1 blockade
G-CSF blockade

Figure 2-16: Tumor resection resets systemic immune organization and function.
a-c, Statistical scaffold maps of spleen immune cell frequencies (**a**) and proliferation by Ki67 expression (**b**) in 4T1-resected mice, and of spleen immune cell frequencies in MC38-resected mice (**c**) compared to healthy control. Insets show resected mice compared to tumor-burdened mice. **d-e**, Heatmap of the log2 fold changes in splenic immune cell frequencies for local or lung recurrences from control mice (**d**), and for IL-1, G-CSF, or TGFβ blockade from untreated AT3 tumor-burdened mice (**e**). **f-g**, Heatmaps of T cell cluster expression profiles and log2 fold change from control for AT3 (**f**) and 4T1 (**g**) for the spleen and draining lymph node. **h**, Median signal intensity of CD86 and PD-L1 on splenic cDCs from healthy, AT3 tumor-burdened, resected, or resected mice with local recurrence at day 7 of *Lm*-OVA infection. **i**, Concentration of circulating cytokines, IL-1α and G-CSF from healthy, AT3 tumor-burdened, resected, or resected mice with local recurrence. **j**, Concentration of circulating G-CSF in control or AT3 tumor burdened mice left untreated or after 1L-1 or G-CSF blockade. **k**, Concentration of cytokines, IL-1α, IL-1β and G-CSF from *in vitro* cell culture media conditioned with AT3 cancer cells. p*<0.05, two-tailed t-test.

Table 2-1: Antibody panel used for mass cytometry experiments.

MAIN

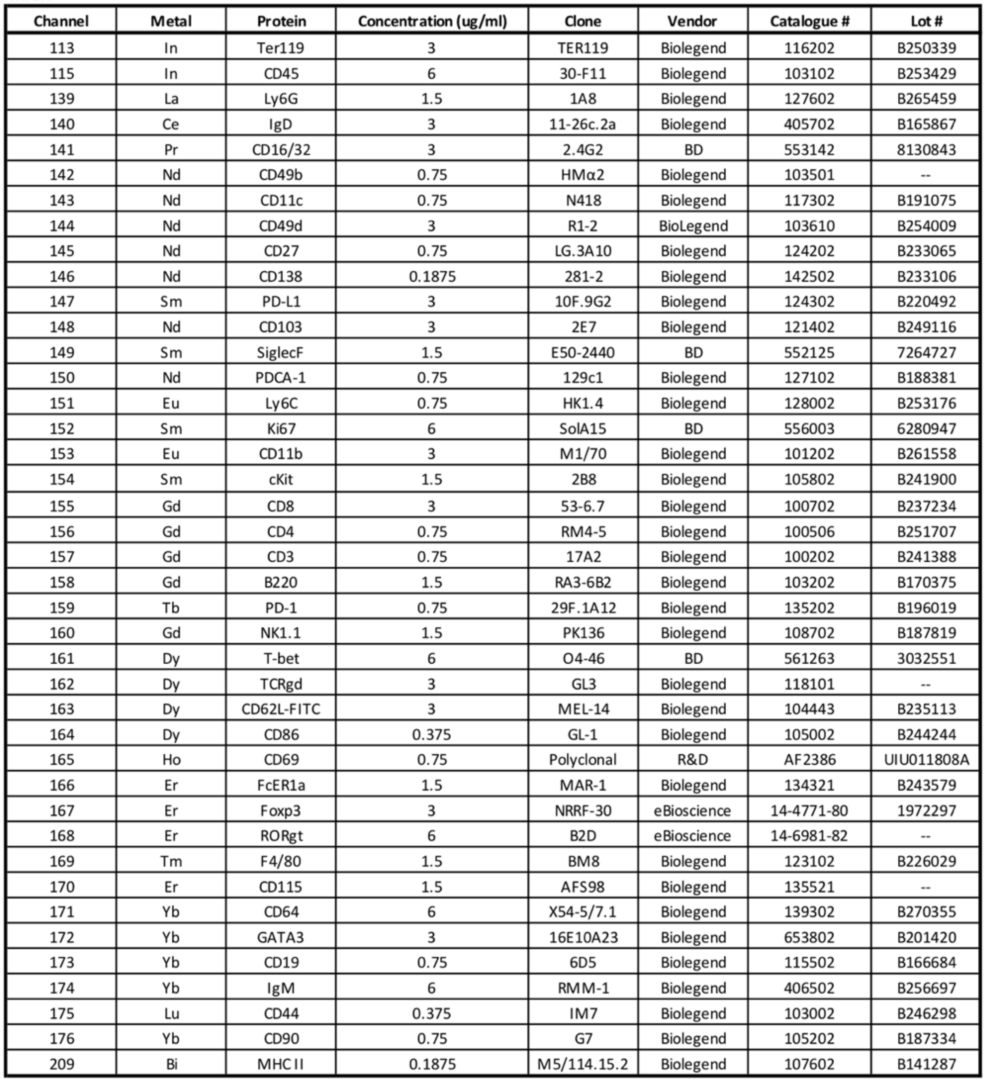

Channel	Metal	Protein	Concentration (ug/ml)	Clone	Vendor	Catalogue #	Lot #
113	In	Ter119	3	TER119	Biolegend	116202	B250339
115	In	CD45	6	30-F11	Biolegend	103102	B253429
139	La	Ly6G	1.5	1A8	Biolegend	127602	B265459
140	Ce	IgD	3	11-26c.2a	Biolegend	405702	B165867
141	Pr	CD16/32	3	2.4G2	BD	553142	8130843
142	Nd	CD49b	0.75	HMα2	Biolegend	103501	--
143	Nd	CD11c	0.75	N418	Biolegend	117302	B191075
144	Nd	CD49d	3	R1-2	BioLegend	103610	B254009
145	Nd	CD27	0.75	LG.3A10	Biolegend	124202	B233065
146	Nd	CD138	0.1875	281-2	Biolegend	142502	B233106
147	Sm	PD-L1	3	10F.9G2	Biolegend	124302	B220492
148	Nd	CD103	3	2E7	Biolegend	121402	B249116
149	Sm	SiglecF	1.5	E50-2440	BD	552125	7264727
150	Nd	PDCA-1	0.75	129c1	Biolegend	127102	B188381
151	Eu	Ly6C	0.75	HK1.4	Biolegend	128002	B253176
152	Sm	Ki67	6	SolA15	BD	556003	6280947
153	Eu	CD11b	3	M1/70	Biolegend	101202	B261558
154	Sm	cKit	1.5	2B8	Biolegend	105802	B241900
155	Gd	CD8	3	53-6.7	Biolegend	100702	B237234
156	Gd	CD4	0.75	RM4-5	Biolegend	100506	B251707
157	Gd	CD3	0.75	17A2	Biolegend	100202	B241388
158	Gd	B220	1.5	RA3-6B2	Biolegend	103202	B170375
159	Tb	PD-1	0.75	29F.1A12	Biolegend	135202	B196019
160	Gd	NK1.1	1.5	PK136	Biolegend	108702	B187819
161	Dy	T-bet	6	O4-46	BD	561263	3032551
162	Dy	TCRgd	3	GL3	Biolegend	118101	--
163	Dy	CD62L-FITC	3	MEL-14	Biolegend	104443	B235113
164	Dy	CD86	0.375	GL-1	Biolegend	105002	B244244
165	Ho	CD69	0.75	Polyclonal	R&D	AF2386	UIU011808A
166	Er	FcER1a	1.5	MAR-1	Biolegend	134321	B243579
167	Er	Foxp3	3	NRRF-30	eBioscience	14-4771-80	1972297
168	Er	RORgt	6	B2D	eBioscience	14-6981-82	--
169	Tm	F4/80	1.5	BM8	Biolegend	123102	B226029
170	Er	CD115	1.5	AFS98	Biolegend	135521	--
171	Yb	CD64	6	X54-5/7.1	Biolegend	139302	B270355
172	Yb	GATA3	3	16E10A23	Biolegend	653802	B201420
173	Yb	CD19	0.75	6D5	Biolegend	115502	B166684
174	Yb	IgM	6	RMM-1	Biolegend	406502	B256697
175	Lu	CD44	0.375	IM7	Biolegend	103002	B246298
176	Yb	CD90	0.75	G7	Biolegend	105202	B187334
209	Bi	MHC II	0.1875	M5/114.15.2	Biolegend	107602	B141287

Other Substitutes

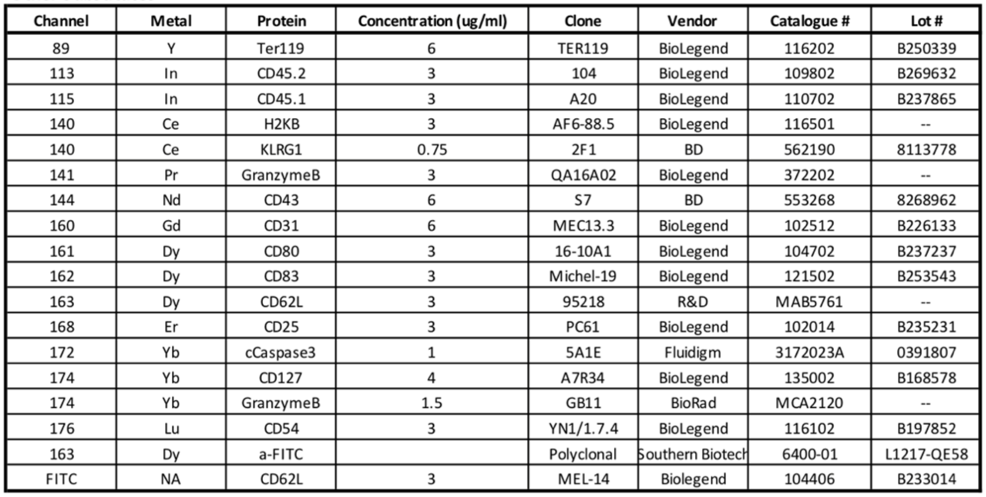

Channel	Metal	Protein	Concentration (ug/ml)	Clone	Vendor	Catalogue #	Lot #
89	Y	Ter119	6	TER119	BioLegend	116202	B250339
113	In	CD45.2	3	104	BioLegend	109802	B269632
115	In	CD45.1	3	A20	BioLegend	110702	B237865
140	Ce	H2KB	3	AF6-88.5	BioLegend	116501	--
140	Ce	KLRG1	0.75	2F1	BD	562190	8113778
141	Pr	GranzymeB	3	QA16A02	BioLegend	372202	--
144	Nd	CD43	6	S7	BD	553268	8268962
160	Gd	CD31	6	MEC13.3	BioLegend	102512	B226133
161	Dy	CD80	3	16-10A1	BioLegend	104702	B237237
162	Dy	CD83	3	Michel-19	BioLegend	121502	B253543
163	Dy	CD62L	3	95218	R&D	MAB5761	--
168	Er	CD25	3	PC61	BioLegend	102014	B235231
172	Yb	cCaspase3	1	5A1E	Fluidigm	3172023A	0391807
174	Yb	CD127	4	A7R34	BioLegend	135002	B168578
174	Yb	GranzymeB	1.5	GB11	BioRad	MCA2120	--
176	Lu	CD54	3	YN1/1.7.4	BioLegend	116102	B197852
163	Dy	a-FITC		Polyclonal	Southern Biotec	6400-01	L1217-QE58
FITC	NA	CD62L	3	MEL-14	Biolegend	104406	B233014

Table 2-2: Change in spleen immune cell frequencies with tumor burden.

two-sided Wilcoxon rank-sum tests with Benjamini-Hochberg correction

4T1		
Immune Cell Type	**raw pVal**	**adjusted pVal**
ClassicalMonocytes	5.28E-05	0.000686167
Neutrophils	5.28E-05	0.000686167
Bcells	6.55E-05	0.000785893
Tregs	8.11E-05	0.000891661
gdTCells	0.000123	0.001232678
nonClassicalMonocytes	0.000186	0.001670571
CD8TCells	0.00072	0.004320097
NKCells	0.000598	0.004320097
PlasmaCells	0.00072	0.004320097
Eosinophils	0.001481	0.007403936
CD4TCells	0.006514	0.026055191
pDCs	0.011825	0.035476343
cDCs	0.779707	0.779706761
Macrophages	0.460883	0.779706761

AT3		
Immune Cell Type	**raw pVal**	**adjusted pVal**
ClassicalMonocytes	8.73E-05	0.00122275
Neutrophils	0.000115	0.001489942
Eosinophils	0.000253	0.003031765
nonClassicalMonocytes	0.000419	0.004611308
Macrophages	0.000869	0.008688611
Bcells	0.001384	0.012454788
CD8TCells	0.005073	0.040583301
pDCs	0.007574	0.053018294
cDCs	0.019242	0.096212185
NKCells	0.016096	0.096212185
CD4TCells	0.037797	0.151188336
gdTCells	0.156288	0.468863135
PlasmaCells	0.488718	0.921212055
Tregs	0.921212	0.921212055

MMTV-PyMT		
Immune Cell Type	**raw pVal**	**adjusted pVal**
ClassicalMonocytes	0.014248	0.170976956
NKCells	0.014248	0.170976956
nonClassicalMonocytes	0.014248	0.170976956
Neutrophils	0.022494	0.247436983
CD8TCells	0.034611	0.311495018
pDCs	0.034611	0.311495018
Eosinophils	0.051913	0.415303719
cDCs	0.075927	0.531488741
Bcells	0.150786	0.799846106
Macrophages	0.271899	0.799846106
CD4TCells	0.446873	0.799846106
PlasmaCells	0.672604	0.799846106
Tregs	0.672604	0.799846106
gdTCells	0.799846	0.799846106

Number of Animals	4T1	AT3	MMTV-PyMT
Controls	8	10	3
Tumor	17	12	7

$p < 0.05$

$P < 0.1$

nonsignificant

Table 2-3: Antibody panel used for flow cytometry experiments.

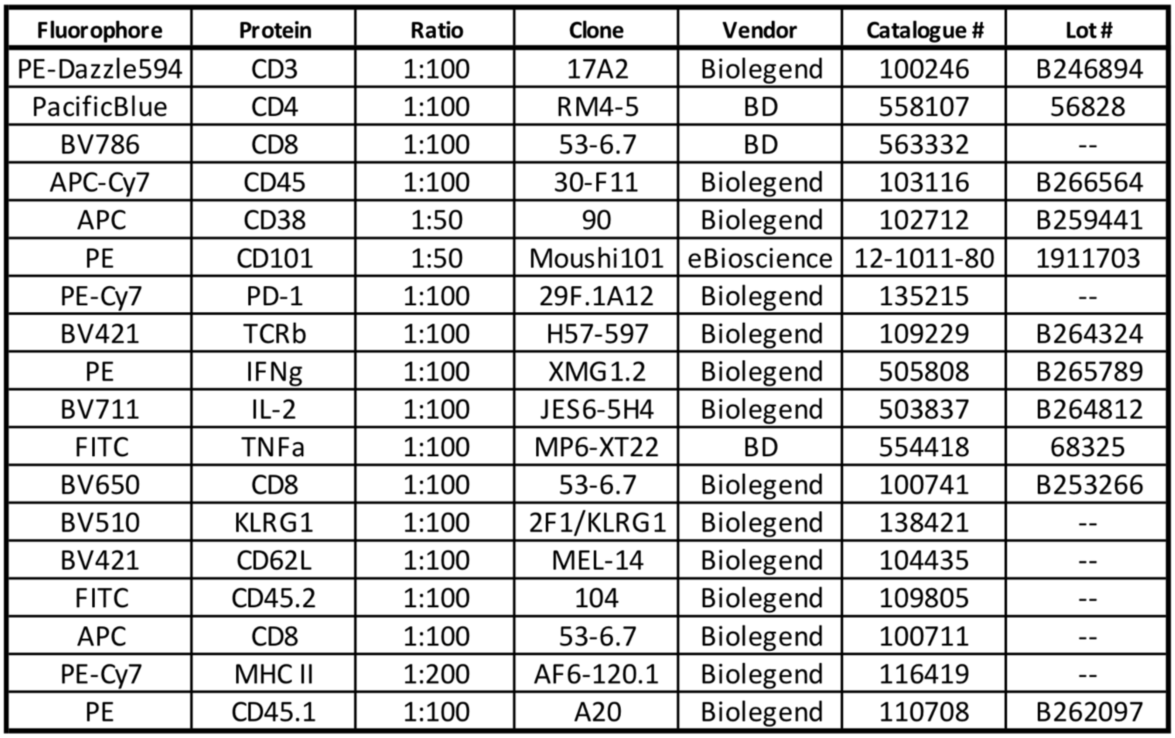

Fluorophore	Protein	Ratio	Clone	Vendor	Catalogue #	Lot #
PE-Dazzle594	CD3	1:100	17A2	Biolegend	100246	B246894
PacificBlue	CD4	1:100	RM4-5	BD	558107	56828
BV786	CD8	1:100	53-6.7	BD	563332	--
APC-Cy7	CD45	1:100	30-F11	Biolegend	103116	B266564
APC	CD38	1:50	90	Biolegend	102712	B259441
PE	CD101	1:50	Moushi101	eBioscience	12-1011-80	1911703
PE-Cy7	PD-1	1:100	29F.1A12	Biolegend	135215	--
BV421	TCRb	1:100	H57-597	Biolegend	109229	B264324
PE	IFNg	1:100	XMG1.2	Biolegend	505808	B265789
BV711	IL-2	1:100	JES6-5H4	Biolegend	503837	B264812
FITC	TNFa	1:100	MP6-XT22	BD	554418	68325
BV650	CD8	1:100	53-6.7	Biolegend	100741	B253266
BV510	KLRG1	1:100	2F1/KLRG1	Biolegend	138421	--
BV421	CD62L	1:100	MEL-14	Biolegend	104435	--
FITC	CD45.2	1:100	104	Biolegend	109805	--
APC	CD8	1:100	53-6.7	Biolegend	100711	--
PE-Cy7	MHC II	1:200	AF6-120.1	Biolegend	116419	--
PE	CD45.1	1:100	A20	Biolegend	110708	B262097

2.7 Materials and Methods

Animals:

All mice were housed in an American Association for the Accreditation of Laboratory Animal Care–accredited animal facility and maintained in specific pathogen-free conditions. Animal experiments were approved and conducted in accordance with Institutional Animal Care & Use Program protocol number AN157618. Wild-type female BALB/c, C57BL/6, and B6x129 F1 mice between 8-10 weeks old were purchased from The Jackson Laboratory and housed at our facility. 4T1 ($1X10^5$ cells / 100µl) or AT3 ($5x10^5$ cells / 100µl) breast cancer cells were transplanted into the fourth mammary fat pad. SB28 glioblastoma cells ($1x10^5$ cells / 2µl) were transplanted into the right cerebral hemisphere by stereotactic injection. MC38 colon cancer cells ($1x10^5$ cells / 100µl), B16-F10 melanoma cancer cells ($1x10^5$ cells / 100µl), or LMP pancreatic cancer cells ($2x10^5$ cells / 100µl) were transplanted into the subcutaneous region of the flank. Female MMTV-PyMT mice were bred at Stanford University. Tyr::CreER; Braf$^{V600E/+;}$ Pten$^{lox/lox}$ mice were purchased from Jackson Laboratory and housed at our facility. Tumors were considered well-established when they reached approximately 1 cm^3 in volume. TCR Transgenic OT-I CD45.1 mice and heterozygous CD45.2,CD45.1 mice were bred at our facility. Animals were housed under standard SPF conditions with typical light/dark cycles and standard chow.

Cell Lines:

4T1 cells were gifted from Dr. Mary-Helen Barcellos-Hoff (UCSF). AT3 cells were gifted from Dr. Ross Levine (MSKCC). For *in vivo* experiments tracking tumor growth and recurrence after resection, we used 4T1 cells expressing mCherry-Luciferase and AT3 cells expressing GFP-Luciferase. SB28 cells, derived from a NRasV12;shp53;mPGDF transposon-induced glioma[112], were gifted from Dr. Hideho Okada (UCSF). LMP cells, derived from the Kras$^{G12D/+}$;LSL-Trp53$^{R172H/+}$;Pdx-1-Cre model of pancreatic cancer[113], were gifted from Dr. Edgar Engleman (Stanford University). MC38 cells and B16-F10 cells gifted from Dr. Jeffrey Bluestone (UCSF). 4T1, MC38, B16 and SB28 cells were cultured in RPMI-1640, and AT3 and LMP cells were cultured in DMEM, all supplemented with 10% fetal calf serum (FCS), 2 mM L-glutamine,100 U/mL penicillin and 100 μg/mL penicillin and streptomycin.

Infectious Agents:

Listeria monocytogenes strain 10403s expressing OVA (*Lm*-OVA) was originally kindly provided by Dr. Shomyseh Sanjabi (UCSF).[114] Lm-OVA stocks frozen at -80 ° C were grown overnight at 37 ° C in BHI broth supplemented with 5 ug/ml erythromycin. Then, overnight cultures were sub-cultured by diluting into fresh BHI broth supplemented with 5 ug/ml erythromycin and grown for 4 hours. Bacteria CFU was then quantified by measuring optical density at 600 nm. Bacteria were then diluted to $5X10^4$ CFU / 100μl in sterile PBS and 100 μl was injected per mouse i.v. via the retro-orbital vein.

Lymphocytic choriomeningitis virus (LCMV) was kindly provided by Dr. Jason Cyster (UCSF) and mice were infected with pre-titered and aliquoted stocks stored in PBS at -80° C and diluted with sterile PBS. Mice were infected with $2x10^5$ PFU by intraperitoneal injection.

Mass Cytometry Antibodies:

All mass cytometry antibodies and concentrations used for analysis can be found in Supplementary Table1. Primary conjugates of mass cytometry antibodies were prepared using the MaxPAR antibody conjugation kit (Fluidigm) according to the manufacturer's recommended protocol. Following labeling, antibodies were diluted in Candor PBS Antibody Stabilization solution (Candor Bioscience GmbH, Wangen, Germany) supplemented with 0.02% NaN3 to between 0.1 and 0.3 mg/mL and stored long-term at 4°C. Each antibody clone and lot was titrated to optimal staining concentrations using primary mouse samples.

Cell Preparation:

All tissue preparations were performed simultaneously from each individual mouse, as previously reported[49]. After euthanasia by $C0_2$ inhalation, peripheral blood was collected via the posterior vena cava prior to perfusion of the animal and transferred into sodium heparin-coated vacuum tubes prior to dilution in PBS with 5 mM EDTA and 0.5% BSA (PBS/EDTA/BSA). Spleens and lymph nodes were homogenized in PBS/EDTA at 4° C. Bone marrow was flushed from femur and re-suspended in PBS/EDTA at 4°C. Tumors were finely minced and digested in RPMI-1640 with 4 mg/ml collagenase IV, and 0.1 mg/ml DNase I. After digestion, re-suspended cells were quenched with PBS/EDTA at 4° C. All tissues were washed with PBS/EDTA and re-suspended 1:1 with PBS/EDTA and 100 mM cisplatin (Enzo Life Sciences, Farmingdale, NY) for 60 s before quenching 1:1 with PBS/EDTA/BSA to determine viability as previously described[86]. Cells were centrifuged at 500 x g for 5 min at 4°C and re-suspended in PBS/EDTA/BSA at a density between 1-10 x 10^6 cells/ml. Suspensions were fixed for 10 min at RT using 1.6% paraformaldehyde (PFA) in PBS and frozen at -80° C.

Mass-Tag Cellular Barcoding:

Mass-tag cellular barcoding was performed as previously described[115]. Briefly, 1 x 10^6 cells from each animal were barcoded with distinct combinations of stable Pd isotopes in 0.02% saponin in PBS. Samples from any given tissue from each mouse per experiment group were barcoded together. Cells were washed once with cell staining media (PBS with 0.5% BSA and 0.02% NaN3), and once with 1X PBS, and pooled into a single FACS tube (BD Biosciences). After data collection, each condition was deconvoluted using a single-cell debarcoding algorithm[115].

Mass Cytometry Staining and Measurement:

Cells were resuspended in cell staining media (PBS with 0.5% BSA and 0.02% NaN_2) and metal-labeled antibodies against CD16 and CD32 were added at 20 μg/ml for 5 min at room temperature (RT) on a shaker to block Fc receptors. Surface marker antibodies were then added, yielding 500 uL final reaction volumes and stained for 30 min at RT on a shaker. Following staining, cells were washed 2 times with cell staining media, then permeabilized with methanol for at 10 min at 4° C. Cells were then washed twice in cell staining media to remove remaining methanol, and stained with intracellular antibodies in 500 μL for 30 min at RT on a shaker. Cells were washed twice in cell staining media and then stained with 1mL of 1:4000 191/193Ir DNA intercalator (Fluidigm) diluted in PBS with 1.6% PFA overnight. Cells were then washed once with cell staining media and then two times with double-deionized (dd) H_20. Care was taken to assure buffers preceding analysis were not contaminated with metals in the mass range above 100 Da. Mass cytometry samples were diluted in dd H_2O containing bead standards (see below) to approximately 10^6 cells per mL and then analyzed on a CyTOF 2 mass cytometer (Fluidigm) equilibrated with dd H_2O. We analyzed 1-5 x 10^5 cells per animal, per tissue, per time point, consistent with generally accepted practices in the field.

Mass Cytometry Bead Standard Data Normalization:

Data normalization was performed as previously described[49]. Briefly, just before analysis, the stained and intercalated cell pellet was resuspended in freshly prepared dd H_2O containing the bead standard at a concentration ranging between 1 and 2 x 10^4 beads/ml. The mixture of beads and cells were filtered through a filter cap FACS tubes (BD Biosciences) before analysis. All mass cytometry files were normalized together using the mass cytometry data normalization algorithm[116], which uses the intensity values of a sliding window of these bead standards to correct for instrument fluctuations over time and between samples.

Mass Cytometry Gating Strategy:

After normalization and debarcoding of files, singlets were gated by Event Length and DNA. Live cells were identified by Cisplatin negative cells. All positive and negative populations and antibody staining concentrations were determined by titration on positive and negative control cell populations.

Scaffold Map Generation:

Statistical scaffold maps were generated using the open source Statistical Scaffold R package available at github.com/SpitzerLab/statisticalScaffold with modifications detailed below.

Statistical scaffold analysis combines unsupervised clustering to identify immune cell subsets with dimensionality reduction using a force-directed graph to visualize the organization of immune cells within a tissue. Regions of the graph are easy to identify due to the incorporation of canonical immune cell types defined manually as 'landmarks' in the graph. As previously described[49,86], cells from each tissue for all animals were clustered together and then deconvolved into their respective samples. Cluster frequencies or the Boolean expression of specific proteins for each cluster were passed into the Significance Analysis of Microarrays algorithm[117] (using a q-value cutoff of 0.05), and the fold change results were reported (rather than the binary significance cutoff as originally implemented in Spitzer et al., 2017). Cluster frequencies were also correlated with the time from tumor inoculation using Spearman's rank-ordered correlation. All results were tabulated into the Scaffold map files for visualization through the graphical user interface, with coloring modifications to graph the spectrum of fold change or correlation strength. The fold change was log2 normalized and graphed with an upper and lower limit of a four-fold difference, unless otherwise indicated. Cluster frequencies were calculated as a percent of total live leukocytes or parent immune subset as indicated. The spleen data from the 4T1 model were used to spatialize the initial Scaffold map because all major, mature immune cell populations are present in that tissue.

Cell Frequency Heat Map Generation:

Specified subsets, i.e. T cells and mononuclear phagocytes, were manually gated from each tissue for all animals and clustered together. Cluster frequencies were calculated as a percent of total live nucleated cells within that subset (excluding erythrocytes). T cells were identified as $CD3^+$, $CD11b^-$. Mononuclear phagocytes were defined as $CD11b^+$, $CD19^-$, $CD3^-$, $Ly6G^-$. Heatmaps of the resulting cluster frequencies were generated in R.

Human Gene Expression Analysis:

Whole blood microarray data was generated by The Norwegian Women and Cancer (NOWAC) study and is deposited in the European Genome-Phenome Archive under accession number EGAS00001001804 as previously reported[118]. Principal component analysis of centered and scaled data was performed in R using the prcomp function. xCell cell type enrichment analysis[119] was performed in R using the xCell package (https://github.com/dviraran/xCell) using a customized list of cell populations known to exist in peripheral whole blood (B-cells, Basophils, $CD4^+$ memory T-cells, $CD4^+$ naive T-cells, $CD4^+$ T-cells, $CD4^+$ central memory T-cells (Tcm), $CD4^+$ effector memory T-cells (Tem), $CD8^+$ naive T-cells, $CD8^+$ T-cells, $CD8^+$ Tcm, $CD8^+$ Tem, DC, class-switched memory B-cells, eosinophils, erythrocytes, megakaryocytes, memory B-cells, Monocytes, naive B-cells, neutrophils, NK cells, NKT, pDC, plasma cells, platelets, Tgd cells, Th1 cells, Th2 cells, and Tregs).

In vitro CD8 T cell Differentiation and cytokine production:

Mice bearing 21-day AT3 tumors were euthanized and their spleens harvested and dissociated. CD8 T cells were enriched using the EasySep Streptavidin Negative Selection Kit with the following biotinylated markers: CD11b, MHCII, CD11c, Gr1, B220, CD4, CD44, and Ter119. Isolated CD8 T cells were then stimulated with plate-bound anti-CD3 (1μg/mL) and suspended in anti-CD28 (0.5μg/mL) containing T cell media for 3 days. The cells were then removed from CD3/CD28 stimulation and rested for 1 day. Cells were then restimulated with PMA and ionomycin (2μL/mL) or left unstimulated for 4 hours with brefeldin A and analyzed by flow cytometry.

Adoptive T Cell Transfer:

For OT1 and polyclonal adoptive transfers, CD8 T cells were isolated from spleens of CD45.1 OT1 TCR transgenic or CD45.1,CD45.2 heterozygote wildtype or CD45.1 BoyJ mice by enrichment with EasySep Streptavidin Negative Selection Kit with the following biotinylated markers: CD11b, MHCII, CD11c, Gr1, B220, CD4, and Ter119. Cells were stained with CFSE or Cell Trace Violet and $1x10^5$ cells were then adoptively transferred into each recipient mouse via the retroorbital vein.

Quantifying Bacterial Burden:

To quantify bacterial burden, spleens were harvested and dissociated. Cells from each mouse were lysed in 0.5% Triton-X 100 in PBS and cells were serially diluted in duplicate and aliquots were then added to BHI agar and incubated overnight at 37° C. Colonies grown were then counted to quantify bacterial CFU present.

Treatments:

For infection studies, *in vivo* antibody treatments were given i.p. starting on day 0 of *Lm*-Ova infection: 200 µg of agonistic anti-CD40 (FGK4.5, BioXCell) on day 0, 225 µg of recombinant IL-12p70 (BioLegend) daily, and 200 µg of anti-CTLA-4 (9H10, BioXCell) on day 0 and day 3. For cytokine inhibition studies, *in vivo* antibody treatments were given i.p. starting on day 5 after injection of AT3 cells: 10ug of blocking anti-GCSF (67604, R&D Systems) daily, and 200 ug of both blocking anti-IL-1a (ALF-161, BioXCell) and blocking anti-IL-1R (JAMA-147, BioXCell) every 3 days. We observed compensatory elevations in circulating IL-1α with anti-IL-1α treatment, so we added anti-IL-1R to ensure sufficient blockade of this pathway.

Tumor Resection:

Mice bearing 14-day 4T1 tumors or 16 to 21-day AT3 or MC38 tumors (between 350-550mm^3) were anesthetized by intraperitoneal (i.p) injection with a mixture of ketamine and xylazine, and titrated to effect with isoflurane from a precision vaporizer. The surgical site was shaved and sterilized with 70% ethanol and 10% povidone iodine. An incision was made subcutaneously at the anterior midline and along the flank of the side with the tumor, using surgical scissors, to reveal the inguinal mammary tumor. The tumor was teased away using forceps and the surgical wound closed with wound clips. Wound clips were removed after 7 days. 20-30% of AT3- or 4T1-resected mice had tumor recurrence due to incomplete removal of primary tumors or outgrowth of micro-metastases. These mice were separated from successful resection analyses.

Cytokine Quantification:

For *in vivo* circulating plasma cytokines, mice were bled via the retroorbital vein using heparinized capillary tubes. Blood was then centrifuged at 1000 x g for 10 minutes and the supernatant plasma was removed for analysis. For tissue culture supernatants, cells were grown for 48 hours in fresh media, then supernatant was removed, centrifuged at 3000g for 10 minutes to remove debris. Plasma and tissue culture supernatant samples were sent to Eve Technologies (Calgary, AB), and analyzed using a multiplex cytokine array.

Flow Cytometry:

Cells were stained for viability with Zombie-NIR stain. Cell surface staining was performed in cell staining media (PBS with 0.5% BSA and 0.02% NaN3) for 15 minutes at room temperature. Intracellular staining was performed after fixing cells with BioLegend FluoroFix Buffer and permeabilizing cells with BioLegend's Intracellular Staining Perm Wash Buffer. The following anti-mouse antibodies were used: (PE-Dazzle594) – CD3 (clone 17A2), (Pacific Blue) – CD4 (clone RM4-5), (BV786) – CD8 (clone 53-6.7), (APC-Cy7) – CD45 (clone 30-F11), (APC) – CD38 (clone 90), (PE) – CD101 (clone Moushi101) , (PD1) – PE-Cy7 (clone 29F.1A12), (BV421) – TCRb (clone H57-597), (PE) – IFNγ (clone XMG1.2), (BV711) – IL2 (clone JES6-5H4), (FITC) – TNFalpha (clone MP6-XT22), (BV650) – CD8 (clone 53-6.7), (BV510) – KLRG1 (clone 2F1-KLRG1), (BV421) – CD62L (clone MEL-14), (FITC) – CD45.2 (clone 104), (APC) – CD8 (clone 53-6.7), (PE-Cy7) – MHC I (clone AF6-120.1), (PE) – CD45.1 (clone A20). All antibodies were purchased from BioLegend, Inc., BD Biosciences, or Thermo Fisher Scientific. Stained cells were analyzed with a CytoFLEX flow cytometer (Beckman Coulter) or an LSR II flow cytometer (BD Biosciences).Singlets were gated by forward scatter area (FSC-A) and forwards scatter width (FSC-W), as well as by side scatter area (SSC-A) and side scatter width (SSC-W). All positive and negative populations were determined by staining on positive and negative control populations.

Quantification and statistical analysis:

Comparison of cell frequencies and protein expression in Statistical Scaffold was performed using Significance Analysis of Microarrays as described above and in Bair and Tibshirani, 2004 and Bruggner et al., 2014. Features with q <0.05 were considered statistically significant. Comparison of cell frequencies was performed using Wilcoxon rank-Sum test with Benjamini-Hochberg correction in R. Analysis of principle components for human gene expression was performed using two-sided Wilcoxon rank-sum test in R. Analysis of cell correlation with time was performed using Spearman correlation with Benjamini-Hochberg correction. All comparisons over 4T1 tumor growth were performed by one-way ANOVA with Tukey correction in Prism. Unless otherwise states, all other comparisons after infection, treatment, or resection were made using two-sided t tests in Prism. All tests with p <0.05 were considered statistically significant. Unless otherwise stated in the figure legends, n = 3 to 6 independent mice for each experimental condition.

Data availability:

All mass cytometry data are publicly available by request to the senior author without restrictions or at https://premium.cytobank.org/cytobank/projects/2433/.

Code availability:

The updated Statistical Scaffold package is available at https://github.com/SpitzerLab/statisticalScaffold.

Chapter 3 Single-cell metabolic dynamics of early activated CD8 T cells during the primary immune response to infection

Lauren S. Levine[1-6*], Kamir J. Hiam-Galvez[2-6*], Diana M. Marquez[2-6], Iliana Tenvooren[2-6], Diana C. Contreras[7], Jeffrey C. Rathmell[7], Matthew H. Spitzer[2-6]

1. Department of Medicine, University of California San Francisco, San Francisco, CA 94143
2. Helen Diller Family Comprehensive Cancer Center, University of California San Francisco, San Francisco, CA 94158
3. G.W. Hooper Research Foundation, Department of Immunology and Microbiology, University of California San Francisco, San Francisco, CA 94143
4. Department of Otolaryngology, University of California San Francisco, San Francisco, CA 94143
5. Chan Zuckerberg Biohub, San Francisco, CA 94158
6. Parker Institute for Cancer Immunotherapy, San Francisco, CA 94129
7. Vanderbilt Center for Immunobiology, Department of Pathology, Microbiology, and Immunology, Vanderbilt University Medical Center, Nashville, TN 37232

*These authors contributed equally to this work.

Chapter 3 is reprinted as a manuscript in revision.

3.1 Author contributions

L.S.L., K.J.H, J.C.R., and M.H.S. conceptualized this study and designed experiments. L.S.L, K.J.H. D.M.M., I.T. and D.C.C. performed experiments. L.S.L, K.J.H., and M.H.S. performed data analysis. L.S.L. and M.H.S. wrote the manuscript. M.H.S. supervised the study.

3.2 Acknowledgements

We would like to thank the members of the Spitzer lab, Vinh Ngyuen, Stanley Tamaki, Sagar Bapat, Adil Daud, Lawrence Fong, Andrei Goga, Rushika Perera for their experimental contributions and helpful discussions. Listeria monocytogenes strain 10403s expressing OVA (Lm-OVA) was kindly provided by Shomyseh Sanjabi (UCSF). We acknowledge the Parnassus Flow Cytometry Core Facility supported in part by NIH Grants P30DK063720, S10OD018040, S10OD018040 and S10OD021822. Recombinant human IL-2 (IL-2; TECIN; Teceleukin) was provided by the National Cancer Institute.

This work was supported by NIH grants DP5OD023056 to M.H.S. and R01DK105550 and R01HL136664 to J.C.R. L.S.L. was supported by Conquer Cancer Foundation Young Investigator Award grant CA-0122026. M.H.S. is a Chan Zuckerberg Biohub investigator and a Parker Institute for Cancer Immunotherapy investigator.

3.3 Abstract

Memory T cells conventionally rely on oxidative phosphorylation and short-lived effector T cells on glycolysis. Here, we investigate how T cells arrive at these states during an immune response. In order to understand the metabolic state of rare, early activated T cells, we adapted mass cytometry to quantify metabolic regulators at single-cell resolution in parallel with cell signaling, proliferation, and effector function. We interrogated CD8 T cell activation *in vitro* as well as the trajectory of CD8 T cells responding to *Listeria monocytogenes* infection, a well-characterized *in vivo* model for studies of T cell differentiation. This approach revealed a unique metabolic state in early activated T cells characterized by maximal expression of glycolytic and oxidative metabolic proteins. Peak utilization of both pathways was confirmed by extracellular flux analysis. Cells in this transient state were most abundant five days post-infection before rapidly downregulating metabolic protein expression. This approach should be useful for mechanistic investigations of metabolic regulation of immune responses.

3.4 Introduction

Understanding the regulatory mechanisms underlying immune responses is crucial to developing more rationally designed treatment strategies for acute and chronic infections, autoimmune diseases, and malignancy [120]. CD8 T cells, when activated, expand and differentiate into potent short-lived effector cells (SLECs) as well as long-term memory cells, which confer durable protection against re-infection and cancer relapse [121–123]. The former mediate primary adaptive immune responses against pathogens through the release of cytotoxic granules and pro-inflammatory cytokines [124,125]. In contrast, long-lived memory cells remain quiescent until re-encountering antigen, upon which they rapidly mediate secondary immune responses [126]. The field of immunometabolism has provided critical insight into these processes, revealing a complex regulatory interplay of signaling, metabolic, and epigenetic adaptations during CD8 T cell differentiation [127,128].

Upon activation, effector CD8 T cells undergo clonal expansion, necessitating as many as 20 replication cycles to generate sufficient daughter cells to clear pathogens [123]. This process is energetically costly and requires rapid ATP production for the biosynthesis of essential building blocks [127]. Previous studies suggest that the exit from quiescence is supported by a dramatic metabolic shift from oxidative phosphorylation (OXPHOS) in naïve cells, fueled by beta-oxidation of long chain fatty acids (LCFA), to aerobic glycolysis in SLECs, characterized by lactate production in the setting of adequate oxygen [129–131]. This metabolic conversion permits continued cycling through the pentose phosphate pathway and thus generation of intermediates necessary for nucleic acid and lipid biosynthesis. This adaptation also circumvents negative feedback induced by the accumulation of pyruvate and acetyl-CoA [127,132]. Additional feed-forward mechanisms supporting this process include the activation of transcription factors downstream of phosphoinositide 3-kinase (PI3K) signaling. For instance, hypoxia inducible factor 1 (HIF1α) mediates the upregulation of nutrient receptors including glucose transporter 1 (Glut1), the main point of entry for glucose into T cells [129].

Meanwhile, the transition to the memory T cell fate is associated with the inhibition of PI3K/mTORC1 signaling and silencing of aerobic glycolysis by AMP-activated protein kinase (AMPK). Instead, AMPK favors mitochondrial biogenesis and fusion [125,133–135], which is mediated by peroxisome proliferator-activated receptor gamma coactivator 1-alpha (PGC1α) [130,136]. This tightly regulated metabolic shift results in an LCFA-fueled oxidative program characterized by increased mitochondrial mass [133]. This property of memory cells confers additional oxidative potential, known as spare respiratory capacity (SRC), to permit more rapid recall during secondary immune responses [137].

While many previous studies using polyclonal and multicellular T cell populations suggest that a reciprocal, tightly regulated relationship exists between OXPHOS and glycolysis and the signaling cascades that regulate these pathways, their precise interactions in individual cells have yet to be elucidated. Moreover, the regulation of metabolic machinery in rare, early activated T cells remains poorly understood. The early stages of infection lead to antigen specific CD8 T cells acquiring transient cell states preceding differentiation into effector subsets, but precisely how these intermediate stages of differentiation metabolically orchestrate rapid proliferation and differentiation has remained technically challenging [138–140]. Recently, considerable advances in single-cell analysis have enabled studies of signaling and effector programs in T cells at high resolution [141,142]. Analogous studies of T cell metabolic regulation would likely provide new insights. For instance, a recent study utilizing stable isotope tracing in activated T cells has found that OXPHOS may be more prominent in effector T cells *in vivo* than was previously thought [143]. However, in the absence of single-cell resolution, it remains unclear whether the same cells are responsible for both OXPHOS and glycolysis, or alternatively, whether individual cells already differentiate and preferentially use one pathway versus the other during the effector phase. Many of the regulatory mechanisms that govern cellular metabolism are post-transcriptional and are not directly measurable by RNA-sequencing [136]. Therefore, a single-cell proteomic approach provides unique opportunities.

Mass cytometry uses metal-tagged antibodies to directly measure up to 45 proteins simultaneously in individual cells [144,145]. This approach has permitted characterization of various aspects of cellular behavior including phenotype, signaling [146], proliferation [147], and chromatin state [148]. Here, we have further adapted this platform to measure expression levels of enzymes and transporters involved in metabolic checkpoints. We have integrated direct quantitative evaluation of the signaling cues thought to mediate their regulation along with proteins indicative of CD8 T cell fate and function. In this study, we used this approach to interrogate key inflection points of the CD8 T cell response to *Listeria monocytogenes* infection (Lm-OVA), a well-characterized model of CD8 T cell differentiation [149].

3.5 Results

3.5.1 Mass cytometry permits high-dimensional quantification of metabolic regulators in single CD8 T cells

T cell differentiation requires the coordinated interplay of signaling and metabolic pathways, including the upregulation of rate-limiting enzymes and regulatory switches. The transition to aerobic glycolysis in SLECs is mediated by co-stimulatory signaling through CD28 via the AKT/PI3K pathway [129,150]; therefore, we measured the downstream intermediates mTOR, pS6, p4EBP1, and HIF1α (Fig. 3-1A). Signaling through this pathway promotes glucose uptake through the Glut1 receptor and the transcription of glycolytic enzymes [151], including glyceraldehyde-3-phosphate dehydrogenase (GADPH) (Fig. 3-1B), a critical metabolic switch implicated in glycolytic activity, which we also quantified.

To investigate how the TCA cycle is regulated in activated T cells, we evaluated the expression of citrate synthase (CS) (Fig. 3-1B), the first step of the cycle, which is directly regulated by the NAD+/NADH ratio, ADP/ATP ratio, and succinyl-coA levels [152]. As branched chain amino acid metabolism has been demonstrated to be critical for effective T cell activation [153], we sought to understand this process by measuring the large neutral amino acid transporter (LAT1) chaperone CD98 (Fig. 3-1A), a key mediator of the import of these essential nutrients [154–156].

Previous work has described a reciprocal relationship between aerobic glycolysis and OXPHOS, the latter of which is associated with memory T cell differentiation. Therefore, we sought to understand this regulation at the single-cell level by measuring CPT1α, an enzyme that catalyzes the transport of LCFA from the cytoplasm to the mitochondria and that is critical for memory T cell function [137]. Additionally, we measured the mitochondrial trifunctional complex, also known as hydroxyacyl-CoA dehydrogenase (HADHA), which catalyzes the final three steps of LCFA oxidation to acetyl-CoA in the mitochondria [157]. As the role of β-oxidation of medium-chain fatty acids in T cell function has not been extensively evaluated [158], we also measured the expression of medium-chain acyl-CoA dehydrogenase (ACADM), an essential enzyme that catalyzes the initial step of this process (Fig. 3-1B). Moreover, we measured key components of the electron transport chain, including cytochrome C (CytoC) and ATP synthase (ATP5a) (Fig. 3-1B). To understand the counterregulatory processes governing OXPHOS activity and overall energy, we measured voltage-dependent ion channel 1 (VDAC1), a critical regulator controlling cytoplasmic-mitochondrial cross-talk (Fig. 3-1B)[159,160].

The cell signaling pathways that mediate mitochondrial fusion and biogenesis include MAP kinase and NFκB, which are activated during T cell priming [130,161,162]; therefore, we measured the levels of phosphorylated (p) ERK and p-p38 MAP kinases in addition to the total levels of NFκB inhibitor alpha (IκBα). Calcium signaling, triggered by TCR ligation, has also been implicated in this process [163,164]. Therefore, we additionally measured pCREB levels (Fig. 3-1A).

It has been proposed that the activity of metabolic pathways induces the activity epigenetic regulators such as Ezh2, which directly impact T cell fate and function [165,166]. Therefore, we included a full range of well-characterized surface markers and transcription factors to subset T cells into naïve, central memory, effector memory, and terminal effector populations. Finally, to measure the impact on all of these factors on T cell proliferation during clonal expansion, we measured expression of cyclinB1 and Ki67. To assess production of cytotoxic mediators, we also measured granzyme B (Fig. 3-1A).

3.5.2 Mass cytometry recapitulates metabolic phenotypes of CD8 T cell differentiation *in vitro*

In order to query the metabolic program underlying antigen-specific CD8 T cell activation *in vitro,* we first stimulated TCR transgenic OT-1 splenocytes in the presence of their cognate antigen (the SIINFEKL peptide from ovalbumin) and IL-2 for 72 hours. After this initial priming period, antigen was removed, and cells were polarized in IL-2 or IL-7 for an additional 4 days to generate effector (OT-1$_{\text{eff}}$) or central memory cells (OT-1$_{\text{mem}}$), as described previously [125,137,167].

We analyzed the resulting cells by mass cytometry and real-time metabolic profiling by Seahorse assay (Fig. 3-1C, 3-2B-D). In keeping with prior studies [125,137], OT-1_{eff} exhibited higher rates of extracellular acidification associated with glycolytic activity, while OT-1_{mem} possessed marked spare respiratory capacity (Fig. 3-1C).

Consistent with these results, OT-1_{eff} expressed elevated levels of glycolytic proteins at day 7 of activation, as evidenced by robust upregulation of Glut1 and GAPDH (Fig. 3-1D, Fig 3-2A), suggestive of active glucose uptake and utilization. The expression of targets of the PI3K/mTORC1 pathway, including p4EBP1 and HIF1α, were likewise elevated in $OT1_{eff}$ (Fig. 1D), consistent with the promotion of aerobic glycolysis. Also in keeping with previous data [153], the amino acid transporter CD98 was more highly expressed in $OT1_{eff}$ relative to OT-1_{mem} (Fig. 3-1D). In contrast to their effector counterparts, OT-1_{mem} did not demonstrate this glycolytic profile, but instead upregulated CPT1α (Fig. 3-1D, 3-2A), which promotes OXPHOS in memory T cells [137].

3.5.3 Dynamic metabolic changes in canonical subsets of activated CD8 T cells *in vivo*

To understand the metabolic changes during CD8 T cell differentiation in a more physiologic context, we next evaluated the trajectory of the response to acute infection *in vivo*. C57BL/6 mice were infected with *Listeria monocytogenes* expressing whole cytoplasmic ovalbumin (Lm-OVA), a well-characterized model of CD8 T cell differentiation and metabolism [125,133,137]. Splenocytes were harvested daily over the first nine days post-infection for analysis by mass cytometry. We began by identifying canonical T cell differentiation states and investigating changes in metabolic enzyme and transporter expression over the course of the immune response (Fig.3-3A, 3-4A). Unsupervised clustering analysis revealed considerable heterogeneity and dynamic functional changes across all major canonical T cell subsets over the course of the primary immune response to *Listeria monocytogenes* (Fig. 3-3A-B).

At baseline, most naïve cells were predominantly contained within cluster Naïve 1, characterized by the expression of ACADM, pCREB, p-p38, NRF1, and weak expression of GAPDH (Fig. 3-3C). However, three new clusters, Naïve 2 and Naïve 3, emerged at days 1 and 2 post-infection (p.i.) (Fig. 3-3D-E), all characterized by the downregulation of all of the above metabolic and signaling markers (Fig. 3-3C, 3-4A). Interestingly, these clusters demonstrated low IκB expression, suggestive of signaling through NFκB pathway (Fig. 3-3C, 3-3F, 3-4A-B). While most naïve T cells were contained within the Naïve 2 cluster at day 1 post-infection (p.i.) (Fig. 3-3D-E), this gave way to a predominance of the Naïve 3 cluster and days 2 and 3 p.i. (Fig. 3-3D-E). By day 4 p.i., all these new clusters as well as an additional cluster, Naïve 4, were present in similar proportions (Fig. 3-3D-E). Notably, the Naïve 1 cluster began to re-emerge at day 6 p.i., and ultimately dominated the naïve pools from day 7 p.i. onwards (Fig. 3-3D-E). This predominance was associated with the involution of clusters Naïve 2, Naïve 3, and Naïve 4, which became nearly undetectable by day 7 p.i. (Fig. 3-3E). These findings are consistent with activation of both bystander and antigen specific T cells in the early stages of acute infection [168,169] but reveal the metabolic adaptations that these cells undertake. Overall, these data support previous reports of a metabolically quiescent profile of naïve T cells, but they suggest heterogeneity and transitions within even these cells.

Evaluation of the central memory cells over the course of infection revealed a similar pattern, starting with cluster $T_{CM}1$, characterized by intermediate expression of expected markers of LCFA and OXPHOS including p-p38, pCREB, ACADM, HADHA, NRF1, and dim expression of ATP5a, CPT1α, pErk, and CytoC (Fig. 3-3C). Interestingly, this cluster also expressed GAPDH and pS6, but dimly expressed HIF1α compared to effector subsets (Fig 3-3C, 3-4A). However, days 1-2 p.i., were marked by emergence of cluster $T_{CM}2$ (Fig. 3-3D-E), which downregulated all of these metabolic and signaling factors, with only weak expression of HADHA and pS6 and upregulation of ATP5a (Fig. 3-3C, 3-3G, 3-4C). This cluster predominated at days 2 through 4 p.i. Notably, day 2 p.i. was also marked the emergence of cluster $T_{CM}3$ (Fig. 3-3D-E), defined by expression of enzymes of fatty acid oxidation (FAO), including CPT1α, HADHA, ACADM, along with oxidative proteins, such as CS, ATP5a, VDAC1, and CytoC (Fig. 3-3C, 3-4A). These cells also expressed less pS6 and GAPDH, suggestive of a state predominantly fueled by FAO (Fig. 3-3C). Commensurate with this oxidative profile, cells in this cluster also expressed p-p38, pErk, and pCREB (Fig. 3-3C, 3-4A). While cells in $T_{CM}3$ also demonstrated expression of downstream intermediates of the PI3K cascade, such as p4EBP1 and pS6, along with transcription factors associated with aerobic glycolysis, such as HIF1α, these were associated with lower GADPH expression (Fig. 3-3C, 3-4A). This metabolically active T_{CM} cluster was transient, completely regressing by day 7 p.i. (Fig. 3-3D-E). Notably $T_{CM}1$ reemerged at day 5 p.i. and remained the predominant T_{CM} cluster from days 6 through 9 p.i. (Fig. 3-3D). These data confirm the previously oxidative profile of central memory cells, but also reveal dynamic metabolic changes within these subsets over the course of an immune response.

Effector memory cells (T_{EM}) uniformly constituted cluster $T_{EM}1$, which emerged at day 5 p.i. and maintained stable frequency through day 9 p.i. (Fig. 3-3D-E). These cells demonstrated a more glycolytic metabolic profile, with upregulation of GAPDH, Glut1, and HIF1a, and dim oxidative and FAO marker expression (Fig. 3-3C, 3-4A). Meanwhile, SLECs comprised clusters SLEC1 and SLEC2 and emerged at days 5 and 6 p.i., respectively (Fig. 3-3D-E). These two clusters demonstrated distinctive metabolic phenotypes. The first population to appear, SLEC1, demonstrated expression of p4EBP1, pS6, HIF1α, Glut1, and GAPDH suggestive of a glycolytic profile (Fig. 3-3C, 3-3H, 3-4A, 3-4D). Recent studies have demonstrated that early effector cells continue TCA cycle engagement fueled by the uptake of amino acids and LCFA [153,170]; consistently, cells in this cluster also expressed HADHA, CD98, CS, and VDAC1 (Fig. 3-3C, 3-3H, 3-4A, 3-4D). However, ATP5a and CPT1α levels in this cluster were lower than those observed in the more active T_{CM} clusters, such as $T_{CM}3$, distinguishing them from these more classically oxidative pools (Fig. 3-3C, 3-4A). In comparison, cluster SLEC2 demonstrated a more muted metabolic profile, downregulating expression of all metabolic mediators except HIF1α, GAPDH, and CS, taking on the terminal glycolytic state observed in previous studies (Fig. 3-3C, 3-3H, 3-4A, 3-4D). As expected, the more metabolically active cells in cluster SLEC1 expressed higher levels of Ki67 and granzyme B compared to cluster SLEC2 (Fig. 3-3C, 3-4A). Taken together, these findings agree with previous reports of a predominantly glycolytic terminal effector state.

3.5.4 Early activated T cells exhibit maximal expression of glycolytic and oxidative proteins

In addition to these well-characterized cell subsets, unsupervised high-dimensional analysis also revealed a group of early activated T cells that emerged at day 4 post-infection (Fig. 3-3D-E). These cells had high expression of Ki67, indicative of proliferation, and expressed high levels of CD44, CD27, and ICOS, but low levels of CD62L (Fig. 3-3C, 3-4A). This early activated cluster was most abundant at day 5, when it comprised nearly 20% of the CD8 T cell population, and it nearly completely disappeared by day 7 (Fig. 3-3D-E). As ICOS has been found to signal through the PI3K cascade [171], we anticipated that this population would be glycolytic. Indeed, these early activated cells expressed the highest levels of Glut1 and GAPDH across all CD8 T cells (Fig. 3-3C). However, these cells simultaneously exhibited peak expression of oxidative markers, including CPT1α, HADHA, ACADM, and ATP5a (Fig. 3-3C, 3-4A). Commensurate with this observation, the signaling program of this population was marked by maximal expression of both pS6 and pCREB as well as minimal expression of IκB, reflecting simultaneous activity of both the PI3K/mTORC1 and NFκB pathways (Fig. 3-3C, 3-4A). In contrast to SLEC and memory cells, these early activated cells also expressed maximal expression of the amino acid transporter CD98 (Fig. 3-3C, 3-4A).

Given the unique metabolic expression profile of these early activated cells, we sought to confirm these observations through direct inspection of the primary data. We undertook further phenotypic analysis of these cells, which identified the high-affinity IL-2 receptor subunit, CD25, as another surface marker co-expressed by this population of interest, consistent with their recent activation (Fig. 3-5A). Consistent with the clustering analysis, we found that these manually gated cells peaked in frequency at day 5 followed by a rapid decline in abundance (Fig. 3-5B). Moreover, in comparison to all other CD8 T cells present in the animals at day 5, these cells clearly expressed elevated levels of both glycolytic and oxidative proteins (Fig. 3-5C, 3-6A). Therefore, early activated T cells exhibited peak expression of metabolic mediators of oxidative and glycolytic pathways.

3.5.5 Early activated T cells demonstrate peak glycolytic activity and increased mitochondrial activity and mass

Because these early activated T cells were distinguished by simultaneously elevated levels of glycolytic and oxidative enzymes, we posited that this expression profile would translate to greater metabolic activity along these pathways when compared to their SLEC counterparts. To assess real-time bioenergetic flux through oxidative and glycolytic pathways, we sorted naïve, early activated, and SLEC T cells for analysis by Seahorse assay (Fig 3-6B). As expected, SLECs demonstrated significantly higher baseline and maximum ECAR compared to their naïve counterparts (Fig. 3-5D), confirming a predominantly glycolytic program driving the terminal effector state *in vivo*. However, in accordance with their enzymatic expression profile by mass cytometry, early activated T cells exhibited significantly higher basal and maximal ECAR, even compared to SLECs (Fig. 3-5D).

Moreover, baseline and maximal OCR did not significantly differ between the SLEC and naive pools, as described previously [137] (Fig. 3-5E-F). However, early activated T cells did indeed exhibit significantly higher oxidative activity compared to both the SLEC and naïve cells (Fig. 3-5E-F). Since these cells exhibited maximal expression of CPT1α and electron transport complexes, we hypothesized that that this population would possess SRC, in keeping with previous reports studying memory T cells that upregulate these enzymes [137]. Indeed, while neither the naïve or SLEC pools were capable of surpassing their baseline OCR upon FCCP administration, the OCR of early activated T cells nearly doubled (Fig. 3-5E-F). As SRC has been associated with greater mitochondrial mass [133], we sought to quantify the mitochondrial content of these cells using MitoTracker Deep Red, a fluorescent dye staining mitochondria in live cells. Consistent with our mass cytometry and Seahorse data, the early activated T cells contained significantly more mitochondrial mass than the SLEC or naïve pools based on MitoTracker staining (Fig. 3-5G). Overall, these observations confirmed the unique, simultaneously oxidative and glycolytic profile in early activated T cells.

3.5.6 Antigen-specific CD8 T cells transit through the early activation state commensurate with the onset of proliferation

In order to query the antigen-specificity of these metabolic adaptations of early T cell activation, we adoptively transferred OT-1 T cells into congenic hosts, which were then infected with Lm-OVA. Splenocytes were analyzed daily from days 3 through 7 p.i. for metabolic analysis by mass cytometry (Fig. 3-7A-B, 3-8A). Indeed, unsupervised clustering analysis of adoptively transferred OT-1 T cells revealed early activated cells with an analogous state of metabolic activity, arising in small numbers at day 3 p.i. and peaking at day 4 before rapidly regressing by day 5 (Fig. 3-7A-B, 3-8A). The kinetics of the emergence of this cluster were slightly earlier compared to the previously characterized endogenous cells, perhaps a result of higher TCR affinity or increased frequency of antigen-specific precursor cells. Consistent with our findings in endogenous CD8 T cells (Fig. 3-3C, 3-5C), cells comprising this cluster exhibited simultaneous peak expression of markers of glycolysis, OXPHOS, and LCFA oxidation (Fig. 3-7C, 3-8A). We hypothesized that these metabolic adaptations were undertaken in support of clonal expansion of antigen-specific populations. Therefore, we assessed the proliferation of CFSE-labeled adoptively transferred OT-1 T cells on days 3 through 7 p.i. by flow cytometry. Commensurate with the emergence of this early activated metabolic state, the first antigen-specific T cells to divide did so at day 4 p.i. (Fig. 3-7D). By day 5 p.i., all adoptively transferred cells had divided multiple times (Fig. 3-7D). Consistent with this finding, the total number of OT1 T cells only modestly increased between days 3 and 4 p.i., but they subsequently rapidly expanded between days 4 and 5 p.i. before plateauing thereafter (Fig. 3-7E). These observations collectively suggest that early activated antigen-specific CD8 T cells undergo a transition to a metabolic state characterized by peak OXPHOS and glycolytic activity at the same time as they begin blasting, supporting the dramatic expansion of these cells during productive immune responses.

3.5.7 Transient expression of metabolic proteins in early activated T cells

As early activated CD8 T cells with peak metabolic protein expression were highly transient, only detectable for a few days during the immune response, we investigated the changes that take place in these cells thereafter. We sorted early activated T cells and transferred them into congenic hosts before isolating splenic T cells four days later (Fig. 3-7F). At the end of this period of time, the transferred early activated cells had given rise to a mixture of cells with phenotypes consistent with SLECs ($CD44^+$ $KLRG1^+$), as well as memory cells ($CD44^+$ $KLRG1^-$). Given the transient, elevated expression of cell cycle markers by the early activated cells (Fig. 3-3C), we hypothesized that these cells would proliferate briefly upon adoptive transfer. Indeed, these cells expanded, but lost expression of Ki67 over the course of the four days (Fig. 3-7H, 3-8B). These early activated T cells also downregulated expression of CD25 and ICOS, as well as granzyme B by this later time point (Fig. 3-7H, 3-8C). Consistent with a transient burst of metabolic activity, these cells exhibited markedly lower expression of both glycolytic and oxidative markers compared to the early activated T cells from which they originated (Fig. 3-7H, 3-8C). Collectively, these data indicate that during CD8 T cell differentiation, early activated antigen-specific T cells undergo a transient period of peak metabolic activity. Thereafter, downregulation of glycolytic and oxidative pathways takes place coordinate with differentiation into short-lived or memory cells.

3.6 Discussion

Mass cytometry permits broad-spectrum characterization of immune responses in healthy and diseased states [172]. To date, this approach has been used to query the phenotypic and signaling adaptations undertaken by cells during differentiation [173,174]. However, until now, the coordinated downstream metabolic cues supporting these programs have remained incompletely understood at the single-cell level. Here, we directly measured the expression levels of essential nutrient receptors, enzymes, signaling intermediates, and markers of cellular differentiation and effector function at the proteomic level. This allowed us to more thoroughly characterize CD8 T cell responses during acute infection, highlighting the metabolic adaptations of canonical T cell subsets and capturing a unique metabolic state in rare, early activated T cells.

Previous models of the naïve-to-effector transition based on polyclonal population data have proposed a process in which OXPHOS is repressed to promote aerobic glycolysis [129,175]. However, a recent study of intracellular flux in activated T cells has reported that effector T cells may use oxidative phosphorylation *in vivo* [143]. Additionally, it has been observed that effector T cells engage in more active LCFA uptake than their memory cell counterparts, which instead have been shown to mobilize these substrates from lysosomal triglycerides [176]. It is, therefore, feasible that fatty acid uptake may provide additional substrate for OXPHOS early in the course of T cell activation. Our data unify these observations, supporting a coordinated program in which glycolysis and OXPHOS are maintained simultaneously in individual cells during an earlier stage of T cell activation.

Our approach to metabolic profiling by mass cytometry affords investigators the opportunity to functionally characterize the metabolic adaptations of rare cellular populations, such as antigen-specific T cells. These cells would be otherwise difficult to analyze by current standard metabolomics assays due to the prohibitively large number of cells and extensive processing and *ex vivo* culture techniques required for these studies [177,178]. Here, we were able to characterize the metabolic, signaling, and phenotypic progeny of adoptively transferred cells with single-cell resolution. This approach revealed a diversification during CD8 T cell differentiation in the context of acute infection, with a highly metabolically active and proliferative state in T cells early in the course of their response, which later give rise to cells with both memory and terminal effector phenotypes.

The maximal expression of metabolic proteins early after T cell activation suggests a potential role for TCR ligation and/or co-stimulation during CD8 T cell priming. Notably 4-1BB ligation during co-stimulation has been shown to induce mitochondrial fusion via TRAF2-mediated signaling through p38 and PGC1α [130,161]. Similarly, CD28 ligation has been demonstrated to induce CPT1α expression *in vitro* [179]. Whether these signals potentiate the observed spare respiratory capacity and increased mitochondrial mass in early activated T cells will be important to determine. As Drp1-mediated mitochondrial fission has been described in effector cells during metabolic reprogramming to the aerobic glycolytic program [133], it is possible that the absence of co-stimulation and loss of IL-2 signaling upon pathogen clearance may result in mitophagy and/or mitochondrial fission, repressing oxidative activity in terminal effector subsets.

As the importance of metabolism to immune cell fate and function is increasingly appreciated, methods to evaluate these pathways in models of productive and dysregulated immune responses will be critical. The approach presented here may be adapted to any cell type of interest, including both immune cells and non-immune cells, such as interacting epithelial tissues or tumors. This methodology should enable investigators to query the functional programs underlying the development of the full spectrum of immune cell lineages and their compromised state in the context of autoimmunity or malignancy. Additionally, integrated functional analysis of rare cellular subsets will permit simultaneous evaluation of the effects of various treatments on rare populations, such as tumor-infiltrating lymphocytes or neoantigen-specific T cells.

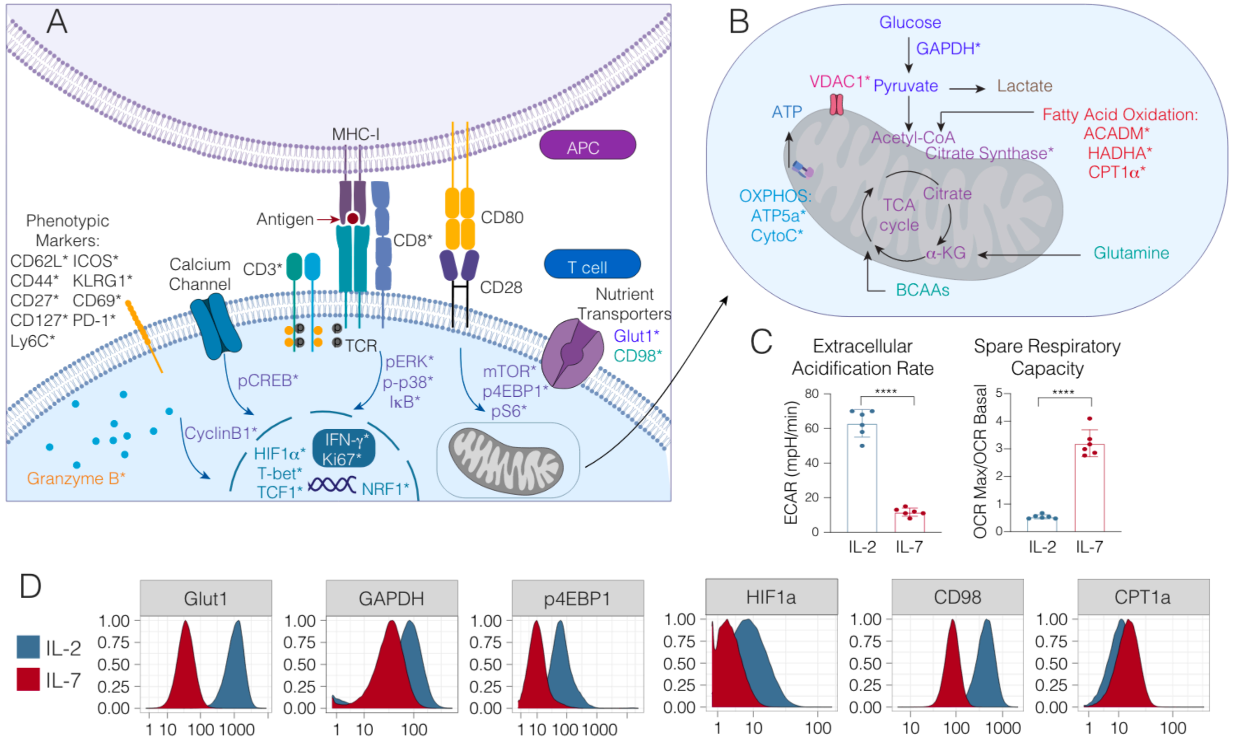

Figure 3-1: Querying the integrated functional program of CD8 T cell activation
Panel schematic depicting signaling, metabolic, effector and phenotypic targets interrogated by mass cytometry. Cell surface, cytosolic and nuclear markers are depicted in (A) and mitochondrial markers are denoted in (B). Markers directly measured by mass cytometry are demarcated by an asterisk (*). OT-1 transgenic CD8 T cells were stimulated with cognate peptide (SIINFEKL) in the presence of IL-2 (100 U/ml) for 72 hours, followed by 3 washes to remove antigen and polarization in IL-2 or IL-7 (both 10 ng/mL) to generate OT-1$_{\text{eff}}$ or OT-1$_{\text{mem}}$. Samples were harvested at day 7 for metabolic analysis by mass cytometry and Seahorse assay analysis by Mitochondrial Stress Test. (C) Mass cytometry expression profiles of day 7 OT1$_{\text{eff}}$ and OT1$_{\text{mem}}$ for key metabolic enzymes as depicted by histograms. (D) Extracellular acidification rate and oxygen consumption rate by Seahorse Assay depicted in bar plots and with significance analysis by student's t-test ($p<.001$ ****). Error bars represent standard error of the mean (SEM). Data are representative of 3 independent experiments.

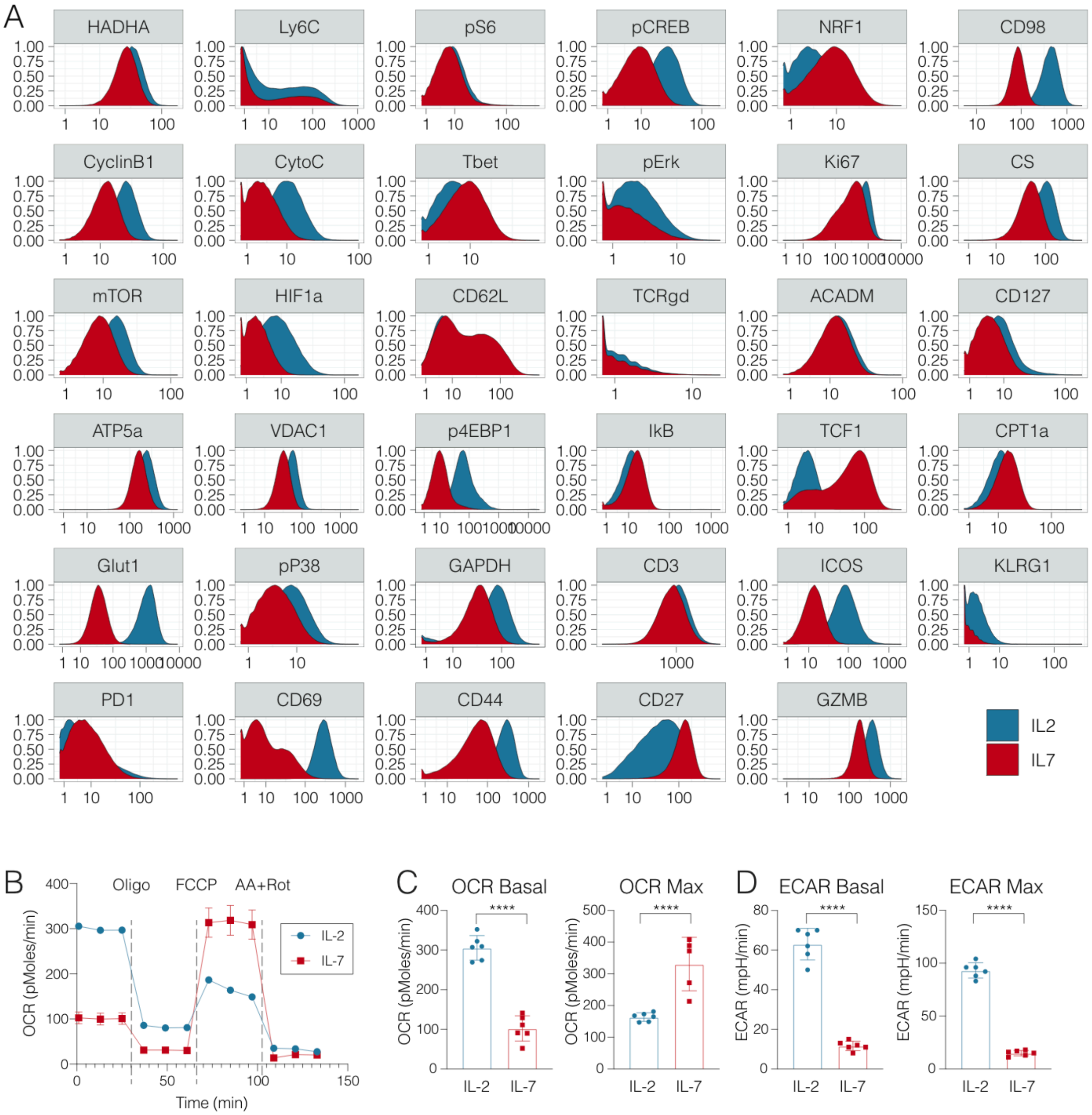

Figure 3-2: Assessing the integrated functional program of antigen specific CD8 T cell activation *in vitro*

A) OT-1 transgenic CD8 T cells were stimulated with cognate peptide (SIINFEKL) in the presence of IL-2 (100 U/ml) for 72 hours, followed by 3 washes to remove antigen and polarization in IL-2, IL-7, or IL-15 (all 10 ng/mL) to generate OT-1effor OT-1mem. Samples were fixed for mass cytometry at all time points depicted and cells were harvested at day 7 for Seahorse assay analysis by Mitochondrial Stress Test. Mass cytometry expression data for key metabolic, signaling and effector markers of interest.(B) OCR tracings as quantified by Seahorse. (C) Basal and maximal OCR readings and (D)basal and maximal ECAR readings as quantified by Seahorse. Significance analysis by paired two-tailed student's t-test ($p<0.05$ *, $p<0.01$ **, $p=0.0001$***, $p<0.0001$****). Error bars represent SEM. Data are representative of at least 2 independent experiments.

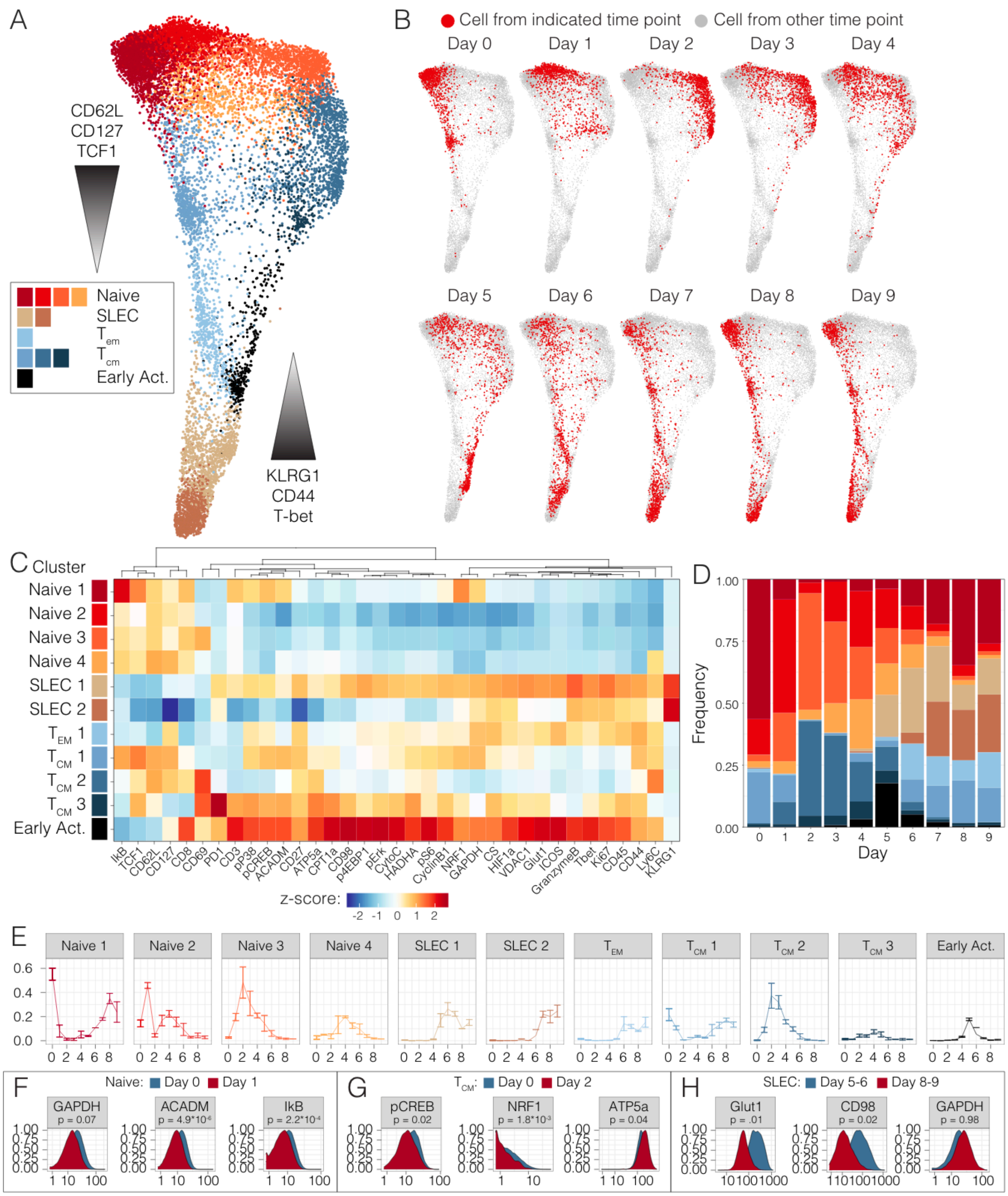

Figure 3-3: Single-cell analysis of the CD8 T cell effector program in vivo. **(A)** Pooled CD8 T cells from mice at days 0 to 9 of Lm-OVA infection (n=2-3 mice per time point) clustered by Phenograph and visualized by a force-directed graph. **(B)** Force-directed graphs indicating cellular distribution by time point. **(C)** Functional and phenotypic median expression profiles for each CD8 T cell cluster**.** **(D)** Cluster proportion by time point **(E)** Individual cluster frequency profiles at days 0 to 9 p.i. (**F)** Expression profiles of metabolic and

signaling in naïve clusters between days 0 and 1 p.i. (**G)** Histograms depicting the expression of functional markers in central memory cells between days 0 and 2 p.i. (**H)** Metabolic expression profiles of SLEC clusters between days 5-6 and 8-9 p.i. Significance analysis of all medians by two-tailed student's t-test ($p<0.05$ *, $p<0.01$ **) is displayed.

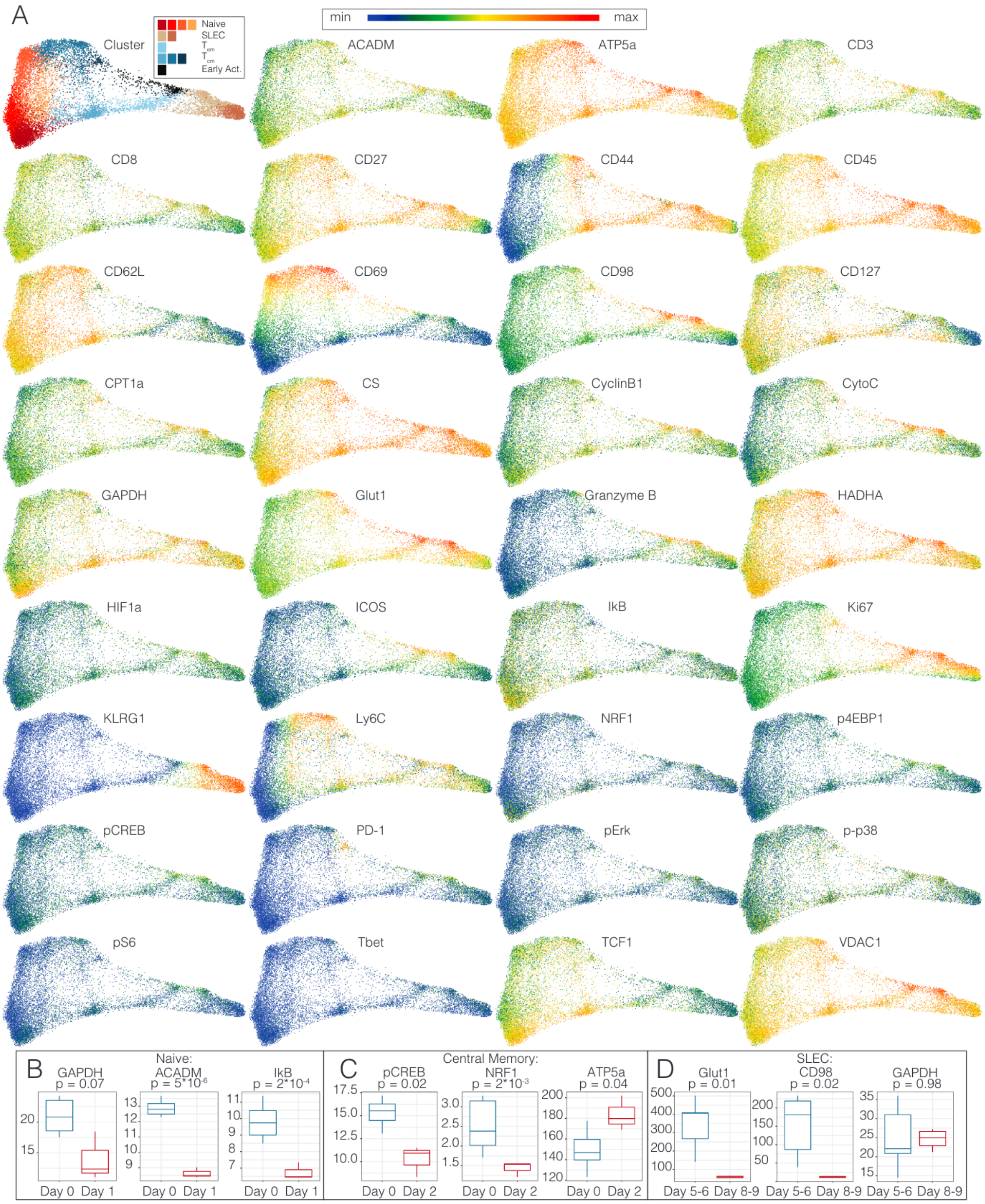

Figure 3-4: Single-cell metabolic analysis of the primary CD8 T cell response *in vivo.*

(A)Pooled CD8 T cells from mice at days 0 to 9 of Lm-OVA infection (n=2-3 mice per time point) clustered by Phenograph and visualized by force-directed graphs. Force-directed graphs of single-cell expression profiles of individual markers are depicted. Box plots of marker expression of (B) naïve, (C) central memory, and (D)SLECs at specified time points post-infection with *Listeria monocytogenes*. Significance analysis by paired two-tailed student's t-test. Whiskers represent 1.5 * IQR.

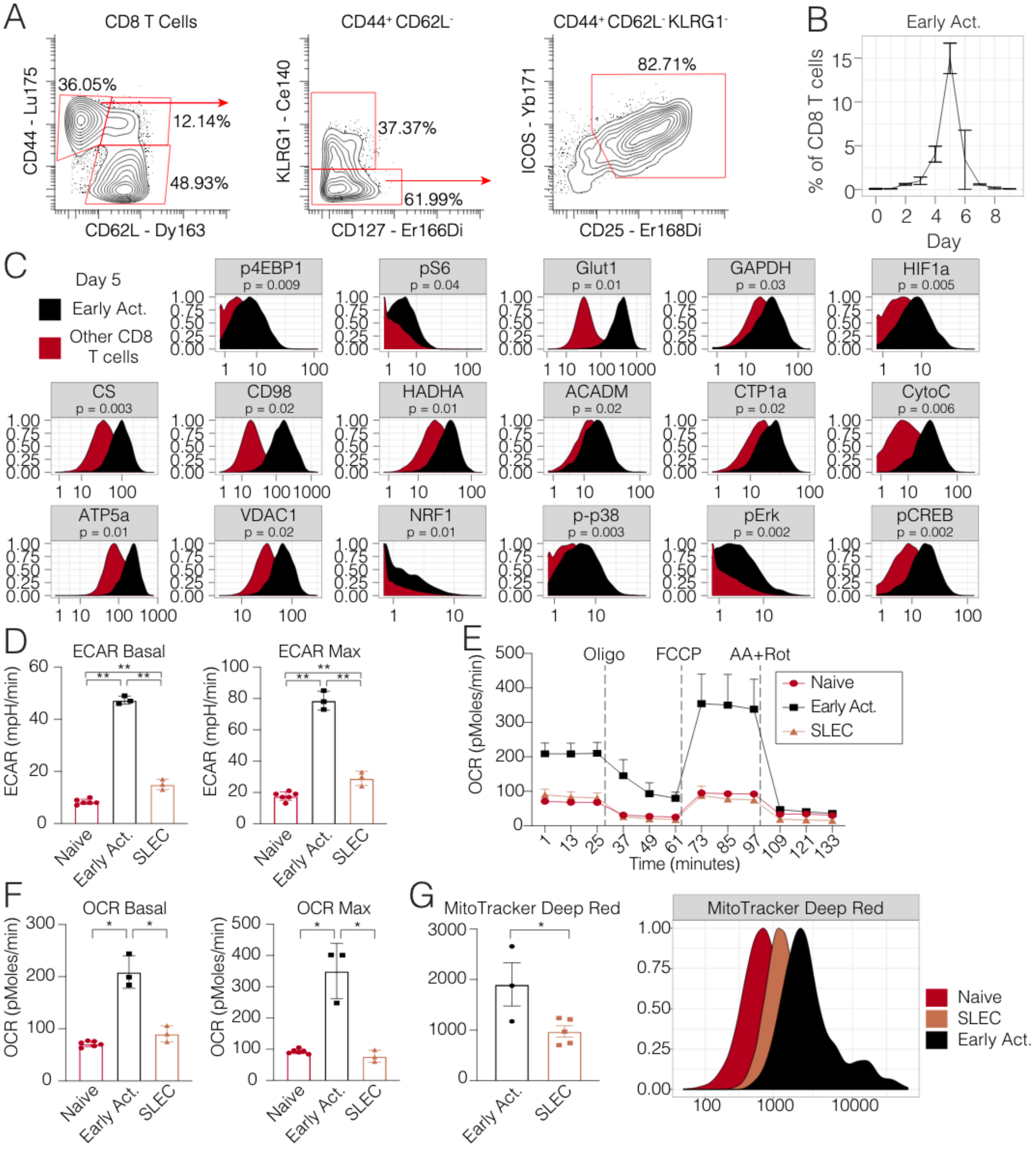

Figure 3-5: Early activated T cells exhibit a distinctive metabolic profile characterized by peak oxidative and glycolytic activity.

(A) Biaxial scatter plots indicating surface marker expression profile of the early activated T cell pool. **(B)** Frequency of early activated cells during days 0 to 9 p.i. **(C)** Metabolic expression profiles of metabolic and signaling markers in early activated T cells in comparison to all other CD8 T cells during days 0 to 9 p.i. as depicted by histograms. Significance analysis of all medians by paired two-tailed student's t-test ($p<0.05$ *, $p<0.01$ **) is displayed. CD8 T cell subsets of interest were sorted at days 5 (including, naïve cells, early activated cells) and 8 (SLECs) p.i. and analyzed by Mitochondrial Stress Test (n=5 mice per time point). **(D)** Basal

ECAR and maximal ECAR measured upon oligomycin administration**.** **(E)** OCR over time. **(F)** Basal and maximal OCR readings obtained upon FCCP administration. **(G)** MitoTracker signal in each subset (n=5 mice per subset). Significance analysis by paired two-tailed student's t-test ($p<0.05$ *, $p<0.01$ **). Error bars represent SEM. Data are representative of at least 2 independent experiments.

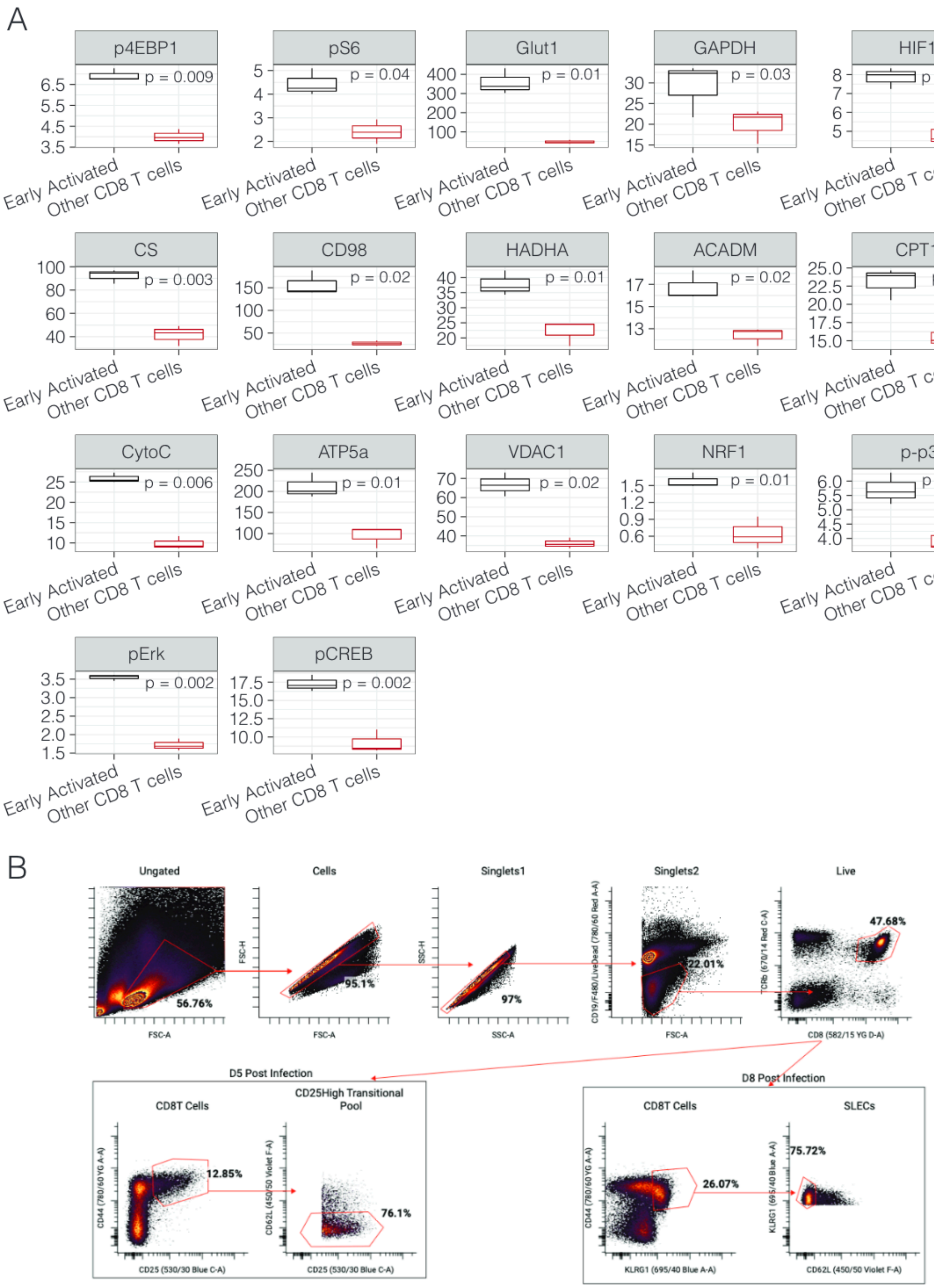

Figure 3-6: Single-cell metabolic analysis by mass cytometry reveals the unique metabolic profile of early activated CD8 T cells

(A) Box plots of marker expression of early activated T cells compared to all other CD8 T cells at day 5 p.i. with *Listeria monocytogenes*. Significance analysis by paired two-tailed student's t-test. Whiskers represent 1.5 * IQR.(B)Sorting strategy for isolation of naïve (CD62L$_{hi}$CD44$_{low}$KLRG1$_{low}$CD25$_{lo}$), transitional effectors(CD62L$_{low}$CD44$_{hi}$CD25$_{hi}$) at day 5 post-infection and SLECs (CD62L$_{low}$CD44$_{hi}$KLRG1$_{hi}$CD25$_{low}$) and day 8 post-infection is depicted by biaxial plots.

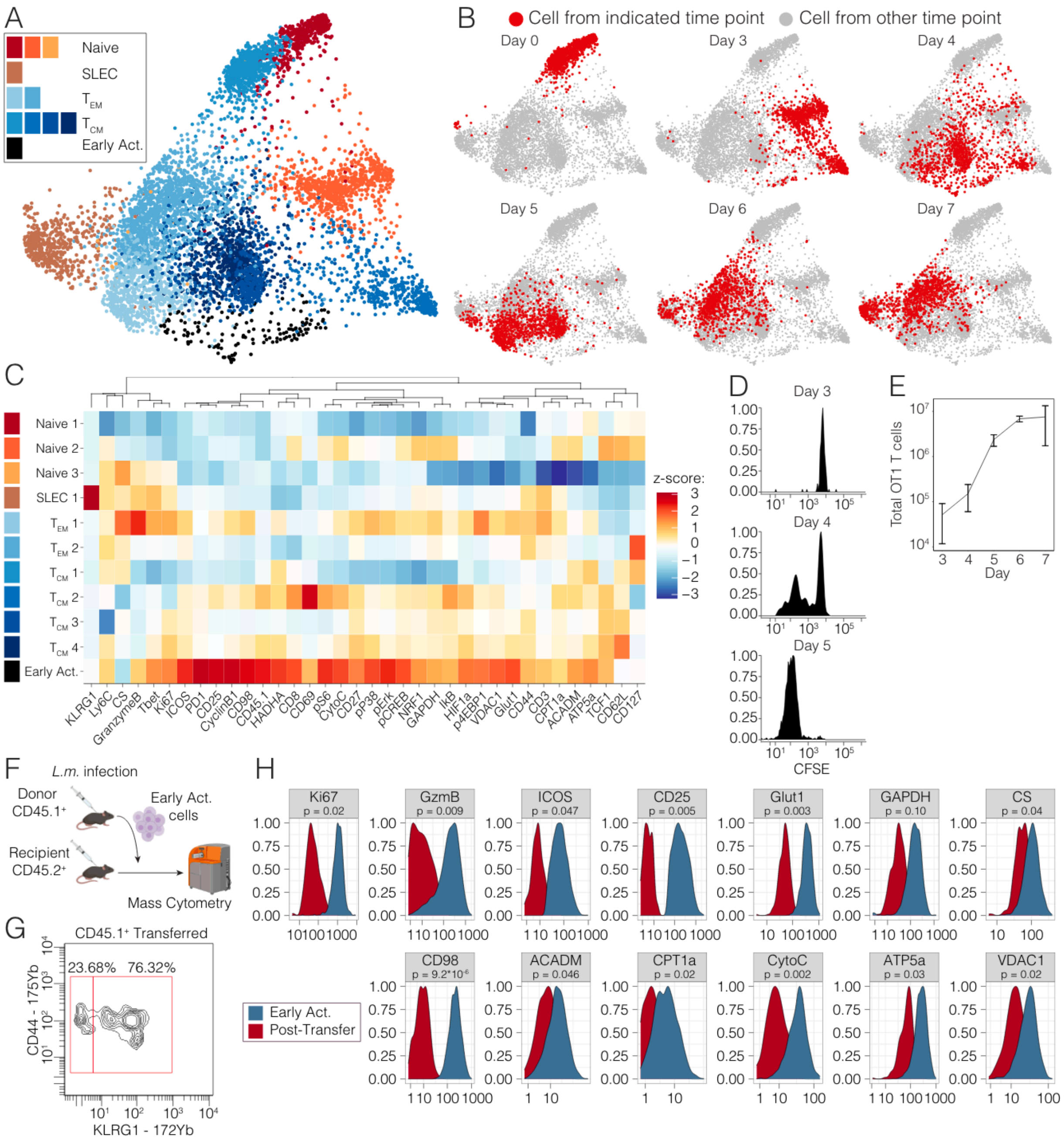

Figure 3-7: The early activated metabolic state is antigen specific and transient. OT-1 T cells were adoptively into congenic hosts, which were then infected with 5 x 10^4 CFU *Lm-OVA*. Splenocytes were harvested daily on days 3 through 7 p.i. for metabolic analysis by mass cytometry. **(A)** Pooled OT1 cells from mice at days 3 to 7 of Lm-OVA infection (n=3 mice per time point except day 3 (n=1)) clustered by Phenograph and visualized by a force-directed graph. **(B)** Force-directed graphs indicating cellular distribution by time point. **(C)** Functional and phenotypic median expression profiles for each CD8 T cell cluster**. (D)** Proliferation of adoptively transferred OT1s as measured by CFSE dilution at days 3-5 p.i. and **(E)** absolute cell counts at days 3-7 p.i. **(F)** Early activated T cells were sorted from $CD45.1^+$ mice at day 5 p.i. and transferred into infected $CD45.2^+$ hosts at day 5 p.i. (n=2 per group) and sacrificed 4 days later for analysis by mass cytometry **(G)** Differentiation state of the transitional subset determined by

CD44 and KLRG1 expression at day 9 p.i. **(H)** Metabolic and signaling marker profiles before and after transfer at days 5 and 9 p.i. are represented by histograms. Significance analysis of the medians by two-tailed student’s t-test ($p<0.05$ *, $p<0.01$ **) is displayed.

3.7 Materials and Methods

Animals

All mice were housed in an American Association for the Accreditation of Laboratory Animal Care–accredited animal facility and maintained in specific pathogen-free conditions. Animal experiments were approved and conducted in accordance with AN157618. Wild-type female C57BL/6 mice and BoyJ CD45.1 between 8-10 weeks old were purchased from The Jackson Laboratory and housed at our facility. TCR Transgenic OT-I CD45.1 mice and heterozygous CD45.2,CD45.1 mice were bred at our facility. Animals were housed under standard SPF conditions with typical light/dark cycles and standard chow.

Infectious Agents

Listeria monocytogenes strain 10403s expressing OVA (Lm-OVA) was kindly provided by Shomyseh Sanjabi (UCSF). Lm-OVA stocks frozen at −80 C were grown overnight at 37˚C in BHI broth supplemented with 5 ug/ml erythromycin (Bio Basic, Amherst, New York). Then, overnight cultures were sub-cultured by diluting into fresh BHI broth supplemented with 5 ug/ml erythromycin and grown for 4 hours. Bacteria CFU was then quantified by measuring optical density at 600 nm. Bacteria were then diluted to 5×10^4 CFU / 100µl in sterile PBS and 100 µl was injected per mouse i.v. via the retroorbital vein.

Mass Cytometry Antibodies

Primary conjugates of mass cytometry antibodies were prepared using the MaxPAR antibody conjugation kit (Fluidigm, South San Francisco, CA) according to the manufacturer’s recommended protocol sourcing metals from Fluidigm (Fluidigm, South San Francisco, CA) or Trace Sciences International (Richmond Hill, Canada). Following labeling, antibodies were diluted in Candor PBS Antibody Stabilization solution (Candor Bioscience GmbH, Wangen, Germany) supplemented with 0.02% NaN_3 to between 0.1 and 0.3 mg/mL and stored long-term at 4°C. Each antibody clone and lot was titrated to optimal staining concentrations using primary mouse samples with all appropriate positive and negative controls: polyclonal murine CD8 T cells purified by positive selection kit (Stem Cell Technologies, Vancouver, Canada) stimulated with PMA/Ionomycin via eBioscience Cell Stimulation Cocktail (ThermoFisher Scientific, Waltham, Massachusetts) for 15 minutes, 3 hours and 6 hours or plate-bound anti-CD3 (145-2C11) and soluble anti-CD28 (37.51) antibodies (UCSF Monoclonal Antibody Core, San Francisco) for 3 days, OT-1 splenocytes at day 7 of IL-2 or IL-7 polarization as below, and appropriate CD8 T cell subsets (Naïve, Short-lived Effector and Central Memory) at day 8 of Lm-OVA infection. Titration results were cross-referenced to the literature as described in the text.

In vitro OT1 Stimulation and Polarization

OT-1 polarizations were carried out as previously described (Carrio *et al*., 2004). Briefly, splenocytes from OT-1 mice were cultured at $1*10^6$ cells/mL in 24 well-plates of complete RPMI-1640 (UCSF Media Core facility) supplemented with 10% FBS (Omega Scientific, Tarzana, California), 100 U/mL penicillin-streptomycin (Fisher Scientific, Hampton, New Hampshire), 2 mM L-glutamine (Sigma-Aldrich, St. Louis, Missouri) and 50 μM β-mercaptoethanol (Thermo Fisher Scientific, Waltham, Massachusetts) and 10 mM HEPES (UCSF Media Core Facility) in the presence of $OVA_{257-264}$ peptide (0.1 nM) (InVivoGen, San Diego, California) and IL-2 (100 U/ml) (Teceleukin) kindly provided by NCI, Frederick, MD. After 3 days in culture, activated cells were washed 3 times with RPMI-1640 and re-cultured in T25 culture flasks at 1×10^5 cells/mL in the presence of either IL-7, IL-15 (BioLegend, San Diego, California), or IL-2 (Teceleukin) kindly provided by NCI, Frederick, MD (all cytokines 10 ng/ml). After 2 additional days in culture, cells were passaged and re-cultured under the same conditions without peptide for an additional two days for total of 7 days in culture. Viability was confirmed by trypan blue exclusion (Thermo Fisher, Waltham, Massachusetts) or mass cytometry as described below.

Cell Preparation

All tissue preparations were performed simultaneously from each individual mouse, as previously reported (Spitzer et al. 2017). After euthanasia by CO_2 inhalation, spleens were collected and homogenized in PBS + 5mM EDTA at 4° C. All tissues were washed with PBS/EDTA and re-suspended 1:1 with PBS/EDTA and 100mM Cisplatin (Enzo Life Sciences, Farmingdale, NY) for 60 s before quenching 1:1 with PBS/EDTA + 0.5% BSA to determine viability as previously described (Spitzer et al., 2015). Cells were centrifuged at 500 x g for 5 min at 4° C and re-suspended in PBS/EDTA/BSA at a density between 1-10 x 10^6 cells/ml. Care was taken to maintain all samples at 4° C during all phases of tissue harvest and preparation except viability staining and fixation. Suspensions were fixed for 10 min at RT using 1.6% PFA in PBS (Fisher Scientific, Hampton, New Hampshire) and frozen at -80° C.

For experiments with adoptively transferred OT1 T cells, immunomagnetic enrichment was performed to facilitate the detection of extremely rare cells before proliferation. Following lysis of red blood cells with ACK lysis buffer (ThermoFisher Scientific, Waltham, Massachusetts), EasySep Streptavidin Negative Selection was used with the following biotinylated antibodies against: MHCII (AF6-120.1), CD11c (N418), Ly6C (RB6-8C5), B220 (RA3-6B2), CD4 (GK1.5), and Ter119 (TER-119).

Mass-Tag Cellular Barcoding

Mass-tag cellular barcoding was performed as previously described (Zunder et al., 2015). Briefly, 1 x 10^6 cells from each animal were barcoded with distinct combinations of stable Pd isotopes in 0.02% saponin in PBS. Samples from any given tissue from each mouse per experiment group were barcoded together. Cells were washed once with cell staining media (PBS with 0.5% BSA and 0.02% NaN_3), and once with 1X PBS, and pooled into a single FACS tube (BD Biosciences, San Jose, California). After data collection, each condition was deconvoluted using a single-cell debarcoding algorithm (Zunder *et al.,* 2015).

Mass Cytometry Staining and Measurement

Cells were resuspended in cell staining media (PBS with 0.5% BSA and 0.02% NaN_3), and antibodies against CD16 and CD32 (BioLegend, San Diego, California) were added at 20 μg/ml for 5 min at RT on a shaker to block Fc receptors. Surface marker antibodies were then added, yielding 500 uL final reaction volumes and stained for 30 min at RT on a shaker. Following staining, cells were washed 2 times with cell staining media, then permeabilized with methanol for at 10 min at 4°C. Cells were then washed twice in cell staining media to remove remaining methanol, and stained with intracellular antibodies in 500 uL for 1 hour at RT on a shaker. Cells were washed twice in cell staining media and then stained with 1 mL of 1:4000 191/193Ir DNA intercalator (Fluidigm, South San Francisco, CA) diluted in PBS with 4% PFA overnight. Cells were then washed once with cell staining media, once with PBS and once with Cell Acquisition Solution (Fluidigm, South San Francisco, CA). Care was taken to assure buffers preceding analysis were not contaminated with metals in the mass range above 100 Da. Mass cytometry samples were diluted in Cell Acquisition Solution containing bead standards (see below) to approximately 10^6 cells per mL and then analyzed on a Helios mass cytometer (Fluidigm, South San Francisco, CA) equilibrated with Cell Acquisition Solution. We analyzed 1-5 x 10^5 cells per animal per time point, consistent with generally accepted practices in the field. For adoptive transfer experiments, 1-4 x 10^6 cells per animal were analyzed.

Mass Cytometry Bead Standard Data Normalization

Data normalization was performed as previously described (Spitzer et al., 2017). Briefly, just before analysis, the stained and intercalated cell pellet was resuspended in freshly prepared Cell Acquisition Solution containing the bead standard at a concentration ranging between 1 and 2 x 10^4 beads/ml. The mixture of beads and cells were filtered through a filter cap FACS tubes (BD Biosciences) before analysis. All mass cytometry files were normalized together using the mass cytometry data normalization algorithm (Finck et al., 2013), which uses the intensity values of a sliding window of these bead standards to correct for instrument fluctuations over time and between samples.

Adoptive T Cell Transfer

For adoptive transfer of transitional cells and SLECs, T cells were sorted by flow cytometry from splenocytes harvested from WT CD45.2 C47Bl/6 mice or CD45.1 BoyJ mice 5 days post-infection. Then, viable sorted cells were counted by hemocytometer and trypan blue staining, resuspended in sterile PBS and transferred into infection-matched congenic mice intravenously via the retroorbital vein.

For adoptive transfer of pathogen specific T cells to validate the antigen specificity of transitional cells, CD8 T cells were immunomagnetically enriched from the spleens of CD45.1 OT1 TCR transgenic mice with EasySep Streptavidin Negative Selection using the following biotinylated antibodies against: MHCII (AF6-120.1), CD11c (N418), Gr1 (RB6-8C5), B220 (RA3-6B2), CD4 (GK1.5), Ter119 (TER-119). Viable cells were quantified by counting on a hemocytometer with Trypan blue staining. 1 x 10^6 cells were then resuspended in sterile PBS and transferred into naïve WT CD45.2 mice intravenously via the retroorbital vein.

Flow Cytometry and Cell Sorting

Cells were stained for viability with Zombie-NIR dye. Cell surface staining was performed in cell staining media (PBS with 0.5% BSA and 0.02% NaN_3) for 30 minutes at room temperature. The following anti-mouse antibodies were used: TCRβ – APC (H57-597), CD8 – PE (53-5.8), CD62L - BV421 (MEL-14), KLRG1 – BV510 (2F1/KLRG1), CD44 – PE-Cy7 (IM7), CD25 – FITC (3C7), CD19 – APC-Cy7 (1D3/CD19), and F480 APC-Cy7 (BM8). Stained cells were analyzed with an LSR II flow cytometer (BD Biosciences). MitoTracker Deep Red (Thermo Fisher, Waltham, Massachusetts) staining was performed per manufacturer’s instructions and as previously (Scharping *et al*., 2016). For MitoTracker Deep Red experiments, Zombie-UV dye was used (BioLegend, San Diego, California).

For sorting experiments, cells were prepared as described for flow cytometry and then sorted into media (RPMI-1640, 20% FBS, 1% HEPES, 100 μg/mL penicillin/streptomycin) using a FACSAria II (BD Biosciences).

Seahorse Assays

Seahorse Assays were carried out using an Agilent Mitochondrial Stress Test kit as previously (van der Windt *et al.*, 2012) and per the manufacturer's instructions. Oxygen consumption rates (OCR) and extracellular acidification rates (ECAR) were measured in XF media (non-buffered RPMI-1640 containing 10 mM glucose, 2 mM L-glutamine, and 1 mM sodium pyruvate) under basal conditions and in response to 1 μM oligomycin, 1 μM fluoro-carbonyl cyanide phenylhydrazone (FCCP), and 100 nM rotenone + 1 μM antimycin A (all from Agilent, Santa Clara, California) using a 96-well XF Extracellular Flux Analyzer (EFA) (Agilent, Santa Clara, California).

Statistical Analysis

All significance analysis of Seahorse data and cellular frequency was performed by paired two-sided student's t-test with error bars representing SEM in Prism v8. (GraphPad, San Diego, California). Analysis of median protein expression was performed by paired or unpaired (as indicated) two-sided student's t-test in R.

Unsupervised Clustering Analysis

Cell clusters were identified using the Phenograph algorithm as implemented in the 'cytofkit' package in R. Standard settings were used (with k = 30 for endogenous CD8 T cells and k = 100 for OT1 T cells).

Data Visualization

Unsupervised force-directed graphs were generated as previously reported (Spitzer *et al.*, 2015) with the following modifications. Single cells were down-sampled to n = 1,000 cells from each condition. All cells were combined in a single graph with edge weights defined as the cosine similarity between the vectors of marker values of each cell. All the pairwise distances were calculated and for each node only the 10 edges of highest weight were retained. The graph was then laid out using the ForceAtlas2 algorithm in Gephi.

Data Availability

Mass cytometry data will be made publicly available as a report on Cytobank (www.cytobank.org) with linked flow cytometry standard (.fcs) files upon acceptance of the manuscript.

Chapter 4 Late priming in acute bacterial infection drives memory T cell differentiation

Kamir J. Hiam-Galvez[1,2], Rachel DeBarge[1,,2], and Matthew H. Spitzer[1,2]

[1]Graduate Program in Biomedical Sciences, University of California, San Francisco, San Francisco, CA, USA

[2]Departments of Otolaryngology and Microbiology & Immunology, Helen Diller Family Comprehensive Cancer Center, Parker Institute for Cancer Immunotherapy, Chan Zuckerberg Biohub, University of California, San Francisco, San Francisco, CA, USA

Chapter 4 is reprinted as a manuscript in preparation

4.1 Author contributions

K.J.H-G and M.H.S. conceptualized this study and designed experiments. K.J.H-G and RD performed experiments. K.J.H-G. performed data analysis. K.J.H-G. wrote the manuscript. M.H.S. supervised the study.

4.2 Acknowledgements

We would like to thank the members of the Spitzer lab, Vinh Ngyuen, Stanley Tamaki, Lewis Lanier, Lawrence Fong, Clifford Lowell, and Carlos Castellanos for their experimental contributions and helpful discussions. *Listeria monocytogenes* strain 10403s expressing OVA (Lm-OVA) was kindly provided by Shomyseh Sanjabi (UCSF). We acknowledge the Parnassus Flow Cytometry Core Facility supported in part by NIH Grants P30DK063720, S10OD018040, S10OD018040, and S10OD021822.

This work was supported by NIH grants DP5OD023056 to M.H.S.. M.H.S. is a Chan Zuckerberg Biohub investigator and a Parker Institute for Cancer Immunotherapy investigator.

4.3 Abstract

Immune responses to infection are dynamic, yet the precise coordination of all immune cell states and fates throughout the course an infection remain poorly defined. Using mass cytometry, we mapped the cellular dynamics of all immune lineages during acute infection with *Listeria monocytogenes* (*Lm*). We identified highly transient dendritic cell activation 2 days post-infection that functions as a critical time window for priming effector T cells. Regulation of this transient state was mediated by dendritic cell (DC) extrinsic IFNγ provided by T cells. Furthermore, antigen-specific T cells that arrive late to the site of priming and miss peak DC activation acquire only memory T cell fates. This temporal regulation of fate is recapitulated by CD8 DCs *ex vivo* suggesting shifts in activation state of a single antigen presenting cell population alter T cell fates. These results uncover a novel mechanism for temporal regulation of T cell differentiation during a dynamic immune response to infection.

4.4 Introduction

One of the most important cellular interactions mediating protective adaptive immune responses is the priming of CD8 T cells by DCs. Upon recognition of cognate antigen presented on Major Histocompatibility Complex class I (MHCI) by DCs, CD8 T cells rapidly divide and differentiate into multiple mature effector populations[60]. Early decisions in T cell fate lead to the acquisition of functionally distinct differentiation states including memory and cytotoxic effector phenotypes[60]. Intriguingly, single cells are committed to specific fates very early after priming by DCs[61,62]. Because strength of signaling during priming dramatically alters fate acquisition[138], this suggests stochasticity in the strength of signals received by T cells during the priming process.

Previous studies have shown that CD8 T cells that are primed after the onset of a chronic viral infection divide less and acquire memory fates[65,180]. Similar results have also been observed for CD4 T cells in a vaccination model[181]. An elegant study transferring CFSE-labeled TCR transgenic T cells at 12 hour intervals of acute *Listeria monocytogenes* (*Lm)* infection showed striking differences in level of proliferation when cells were removed 48 hours after transfer[182]. These data led us to hypothesize that CD8 T cells might receive dramatically different strength of signals through changing antigen abundance at different timepoints early in infection, which we sought to test experimentally.

Here we used mass cytometry to generate a comprehensive map of immune cell activation in the spleen over the first 9 days of infection with *Lm*. Unsupervised analysis of these data allowed for the identification of highly transient cell states across lineages. DC activation transiently peaked at day 2 post-infection and was rapidly downregulated thereafter, a process supported by T cell-derived IFNγ. T cells primed after day 2 post-infection acquired memory fate very early during differentiation. This finding was recapitulated by DCs from different days of infection *ex vivo*, suggesting that rapid temporal changes in DC activation state are sufficient to drive alternative T cell fate acquisition. These findings have important implications for how natural immune responses induce the differentiation of diverse T cell fates and how this might be therapeutically manipulated in different contexts.

4.5 Results

4.5.1 Acute infection drives rapid phenotypic and frequency shifts across all immune lineages in the spleen

To map the complete immune response to acute infection with *Lm* expressing the model antigen ovalbumin (*LmOVA*), wild type C57BL/6 mice were infected intravenously, and spleen tissue was harvested every day for the first 9 days of infection. Mass cytometry was then performed using an antibody panel optimized to detect all major mature immune cell lineages, as well as their activation states. Unsupervised clustering revealed distinct cell states across all immune lineages (Figure 4.1 A-B). Frequencies and phenotypes of all immune lineages shifted dramatically every single day of infection, which was characterized by early increases in neutrophil and B cell populations and decreases in many T cell populations, ultimately leading to T cell expansions (Figure 4.1 C-D, Figure 4.2 E). Immune landscapes were defined in each sample as a composite of unsupervised cluster frequencies. Principal component analysis and clustering of the samples identified 4 distinct phases of immune activation that we deemed as a Baseline cluster (D0, D1), Innate Activation cluster 1 (D2, D3), Innate Activation cluster 2 (D4, D5), and T Cell Activation cluster (D6, D7, D8, D9) (Figure 4.1 E-F). Early increases in neutrophil frequencies coincided with increased circulating G-CSF, which peaked at 2 days post-infection (Figure 4.2 A). A second wave of neutrophil expansion that exceeded the initial wave in cell frequency peaked at day 5 post-infection and coincided with another increase in circulating G-CSF (Figure 4.2 A). The key antigen-presenting cells for priming CD8 T cell responses, DC1s, reached a transient peak activation at 2 days post-infection, as indicated by expression of CD80, CD86, PDL1, and CD69, before rapidly downregulating the expression of these proteins (Figure 4.2 B). Macrophages and cDC2s also exhibited a peak in activation at day 2 post-infection, but underwent more variable activation as indicated by subsequent increases in CD86 and CD80 after this time point. Macrophages in particular continued increased CD80 expression until reaching a dramatic decrease 6 days post-infection (Figure 4.2 B). Early evidence of T cell activation was observed at the end of the Innate Activation cluster 2, as a unique differentiation state of CD8 T cells expressing CD25 and ICOS reached a transient peak on day 5 post-infection (Figure 4.2 C). Early T cell activation preceded a large expansion of KLRG1+ short lived effector cells (SLECs) that peaked at 7 days post-infection (Figure 4.2 D).

4.5.2 Peak dendritic cell activation occurs 2 days post-infection and is regulated by T cell derived IFNγ

CD8+ cDC1s are the critical DC subset required for priming CD8 T cells in response to many challenges including *Lm*[183]. To validate previous findings, we infected wild type and *Batf3*$^{-/-}$ mice which lack cDC1s. At 7 days post-infection, the frequency of KLRG1+granzymeB+ CD8 T cells was significantly reduced in *Batf3*$^{-/-}$ mice (Figure 4.3

A). To further assess the activation of cDC1s over time, we calculated a composite activation score based on the expression of 8 molecules associated with activation (CD54, CD80, CD83, CD86, MHCII, CD69, PDL1, and PDCA1). This score identified that cDC1s acquire a peak activation state 2 days post-infection that is significantly higher than any other day of infection, including the day preceding and following this state, highlighting the transient nature of cDC1 activation (Figure 4.3 B). To identify potential cell extrinsic regulators of cDC1 activation, we quantified cytokines from spleen tissue homogenate over the first 3 days of infection and found that IFNγ levels followed a pattern strikingly similar to cDC1 activation, with a peak at 2 days post-infection (Figure 4.3 C). The STAT1 signaling pathway is a prototypically activated by IFNγ[184]. We, therefore, quantified levels of phosphorylated STAT1 (pSTAT1) at 2 days post-infection and found that cDC1s showed the highest fold-change in pSTAT1, suggesting that IFNγ signaling was acting directly on cDC1s (Figure 4.3 D). In order to identify the cellular source of IFNγ, we depleted either NK cells or T cells (Figure 4.3 E). We found that splenic IFNγ was significantly reduced by T cell depletion, but not NK cell depletion (Figure 4.3 F). Furthermore, peak cDC1 activation at 2 days post-infection was significantly decreased when T cells or IFNγ was depleted (Figure 4.3 G). Together, these results demonstrate that peak DC activation at day 2 post-infection is regulated in a cell extrinsic manner through T cell-derived IFNγ.

4.5.3 Late primed T cells acquire memory fate

To assess the functional consequences of the peak cDC1 activation state at 2 days post-infection, we adoptively transferred TCR transgenic OT1 T cells at 0, 1, 2, 3, or 4 post-infection *LmOVA* and then harvested cells for analysis 7 days after adoptive transfer (Figure 4.4 A). CD8 T cells underwent significantly less proliferation when transferred in 2-4 days post-infection and also underwent significant alterations in fate. We saw a decreased proportion of KLRG1+CD62L- cytotoxic effector cells when cells were transferred at 1 or 2 days post-infection compared to cells transferred at the onset of infection. Strikingly, cells transferred after 2 days post-infection failed to acquire KLRG1+CD62L- fate and differentiated almost exclusively into CD62L+KLRG1- central memory cells (Figure 4.4 B).

To further assess the mechanistic underpinnings of memory fate acquisition in late primed cells, we adoptively transferred CFSE-labeled OT1 T cells at 0 (Early) or 3 (Late) days post-infection and sorted cells for RNA sequencing 72 hours post-adoptive transfer. Intriguingly, we found that late-primed cells had proliferated more at this time point (Figure 4.4 C). This may be because priming occurred immediately as the cells entered the host, whereas priming may not occur immediately for early-primed cells. Nonetheless, we found that late-primed cells began to re-express CD62L after 5 divisions whereas early-primed cells did not (Figure 4.4 D). Furthermore, RNA-seq confirmed that early- and late-primed cells have divergent transcriptional programs that match cytotoxic effector and memory states, respectively (Figure 4.4 E). Late-primed cells expressed higher levels of prototypical memory genes including *Ccr7*, *Tcf7*, and *Sell* whereas early-primed cells expressed higher levels of canonical effector genes such as *Ifng*, *Gzmb*, *Pdcd1*, and *Fasl* (Figure 4.4E).

To further test the mechanisms of late-primed memory differentiation, we sorted cDC1s from D1 or D2 post *LmOVA* infection, co-cultured them *ex vivo* with naïve OT1 CD8 T cells for 3 days, and then assessed T cell fate (Figure 4.4 F). Consistent with our previous data, we found that DCs from later in infection primed significantly more memory T cell fates, as indicated by expression of CD62L by activated CD8 T cells (Figure 4.4 G).

4.6 Discussion

This study is, to the best of our knowledge, the first high-dimensional single-cell time course of a response to acute infection in a lymphoid organ. Recent research in other contexts includes studies assessing immune cells in peripheral blood in response to infection and whole organ transcriptomics in response to vaccination[57,185]. While these studies also suggest that immune responses are highly dynamic in nature, they did not identify the transient activation of antigen-presenting cells described here, likely because the studies sampling peripheral blood did not capture antigen presentation that occurs in lymphoid organs, and whole tissue transcriptomics does not have the single-cell resolution to determine the activation state of extremely rare DC populations. Transient DC activations states have also been described in the response of mice to infection with acute and chronic LCMV[186], as well as MCMV[187], suggesting that this state is a hallmark of acute infection, though these studies did not investigate the consequences for T cell priming. This study is the first to mechanistically link temporal changes in DC activation to regulation of T cell differentiation. Importantly, our data suggest that memory fate is acquired very early during the differentiation trajectory of late-primed cells and is due to the temporal shifts in signals received from DCs rather than through clonal competition. We envision this study as a conceptual framework for studying immune responses as rapid time courses of high-dimensional single-cell data that can reveal novel mechanistic insights for how the immune system makes decisions.

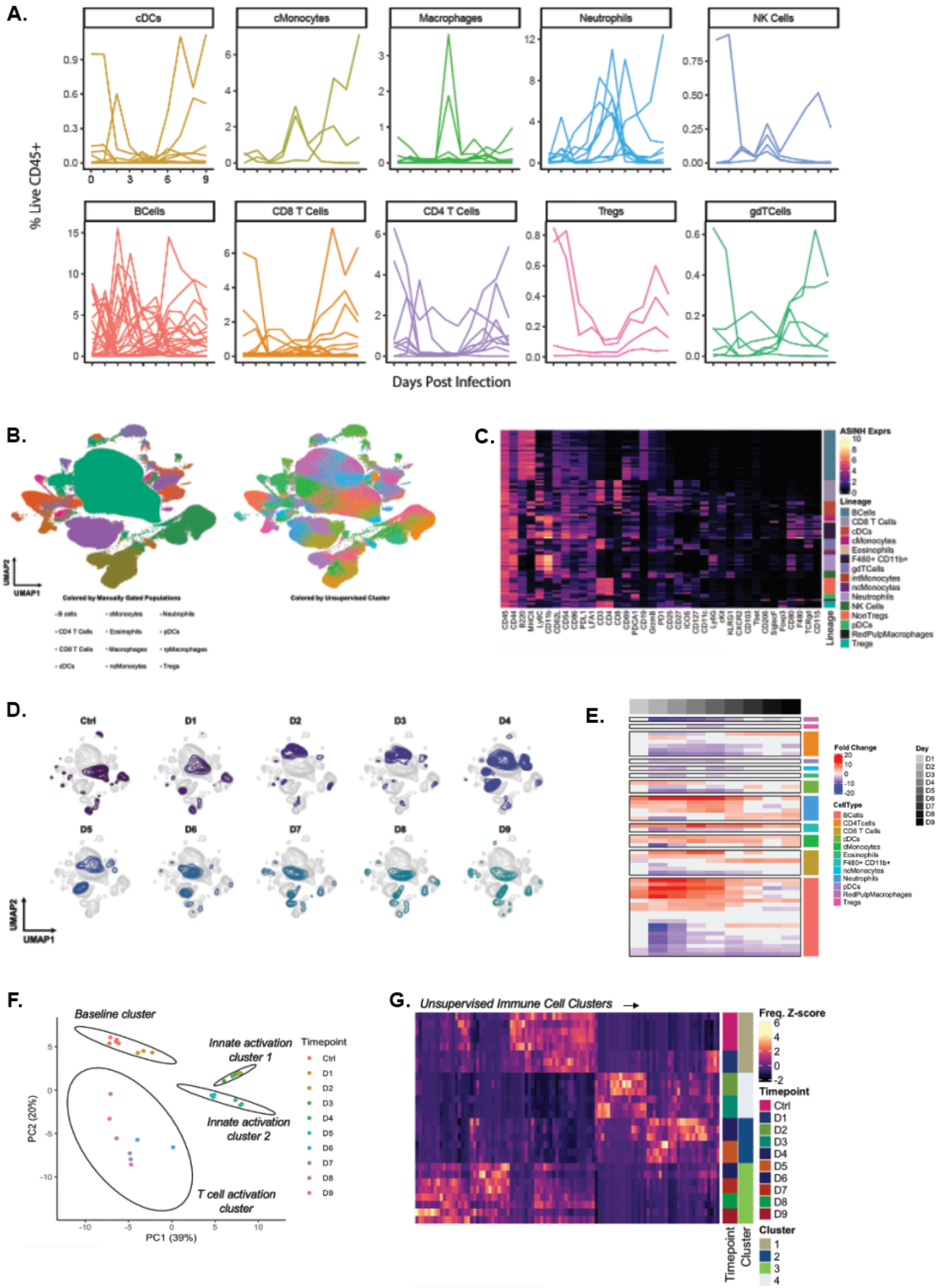

Figure 4-1: Unsupervised clustering identifies dramatic shifts in immune cell frequencies and phenotypes during infection.
(A) Unsupervised clusters from all major lineages are plotted as a frequency of total live CD45+ splenic immune cells at all days of infection. **(B)** All live CD45+ cells are plotted

in UMAP dimensionality reduced space and colored by major cell type, as well as unsupervised cluster. **(C)** Heatmap for median expression in each unsupervised cluster. **(D)** Density of cells in UMAP dimensionality reduced space overlaid on the entire immune landscape at each timepoint. **(E)** Fold-change in frequency (as percent of live CD45+) of each unsupervised cluster compared to frequency in uninfected mice. **(F)** Principal component analysis of single mice as a composite of unsupervised cluster frequency and k-means clusters of samples are circled. **(G)** Heatmap of all unsupervised cluster frequencies in each mouse.

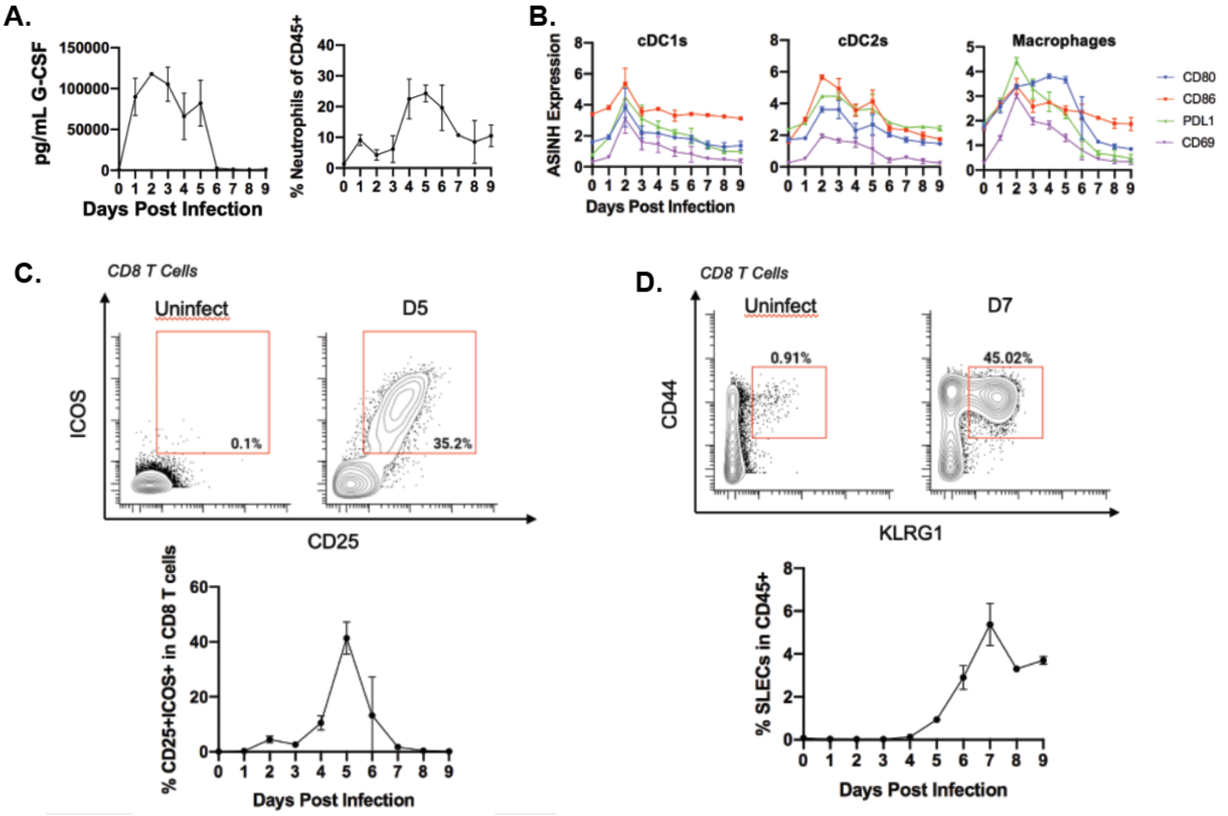

Figure 4-2: Neutrophil, antigen-presenting cell, and CD8 T cell dynamics during infection

(A) Circulating plasma G-CSF levels and neutrophil frequencies across infection time. **(B)** Expression of CD80, CD86, PDL1, and CD69 on cDC1s, cDC2s, and macrophages from all days throughout infection. **(C)** Transitional CD25+ICOS+ CD8 T cells that peak at 5 days post-infection. **(D)** KLRG1+ SLEC frequency over the course of infection.

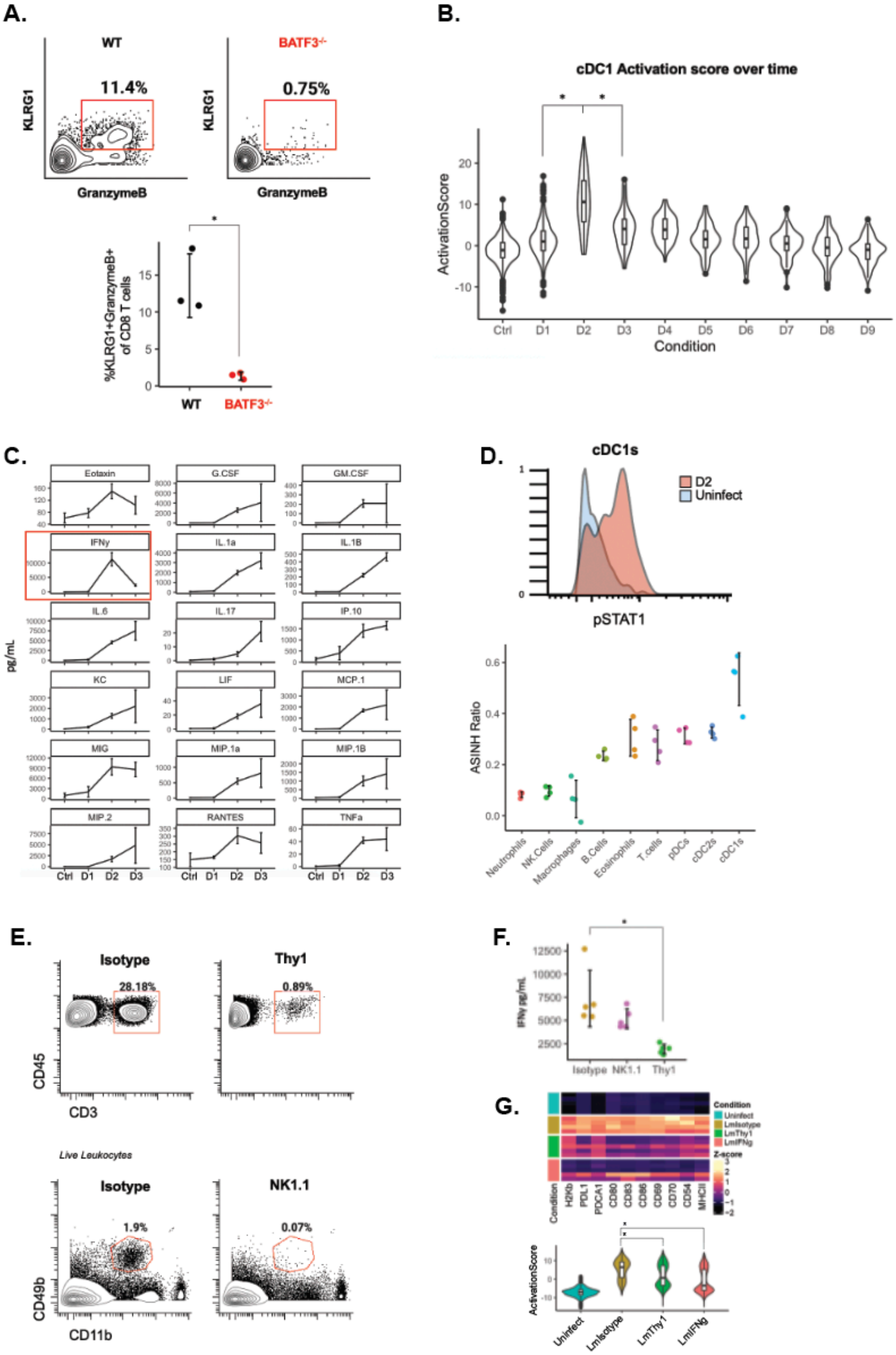

Figure 4-3: Peak dendritic cell activation is supported by T cell-derived IFNg
(A) Frequency of cytotoxic CD8 T cells in the spleen of WT and *Batf3*$^{-/-}$ mice infected with *LmOVA* at D7 post-infection. **(B)** Composite activation score (CD80, CD86, CD83,

CD54, CD69, PDCA1, and PDL1) in single cDC1s plotted at each time point over activation **(C)** Cytokine quantification from the spleen homogenate on D0-D3 post-infection. Significance p<0.01. **(D)** PhosphoSTAT1 quantification in all major immune lineages with fold-change calculated from the median of uninfected mouse samples. **(E)** Antibody-mediated depletion of T cells by anti-Thy1 or NK cells by anti-NK1.1. **(F)** Quantification of IFNg from the spleen homogenate at D2 post-infection in mice depleted of T cells or NK cells. **(G)** Heatmap showing expression of key proteins in splenic cDC1s from uninfected, D2 isotype-matched control Ig treated mice, D2 anti-Thy1-treated mice, or anti-IFNg treated mice. Activation score calculated for cDC1s from each condition. Significance p<0.01.

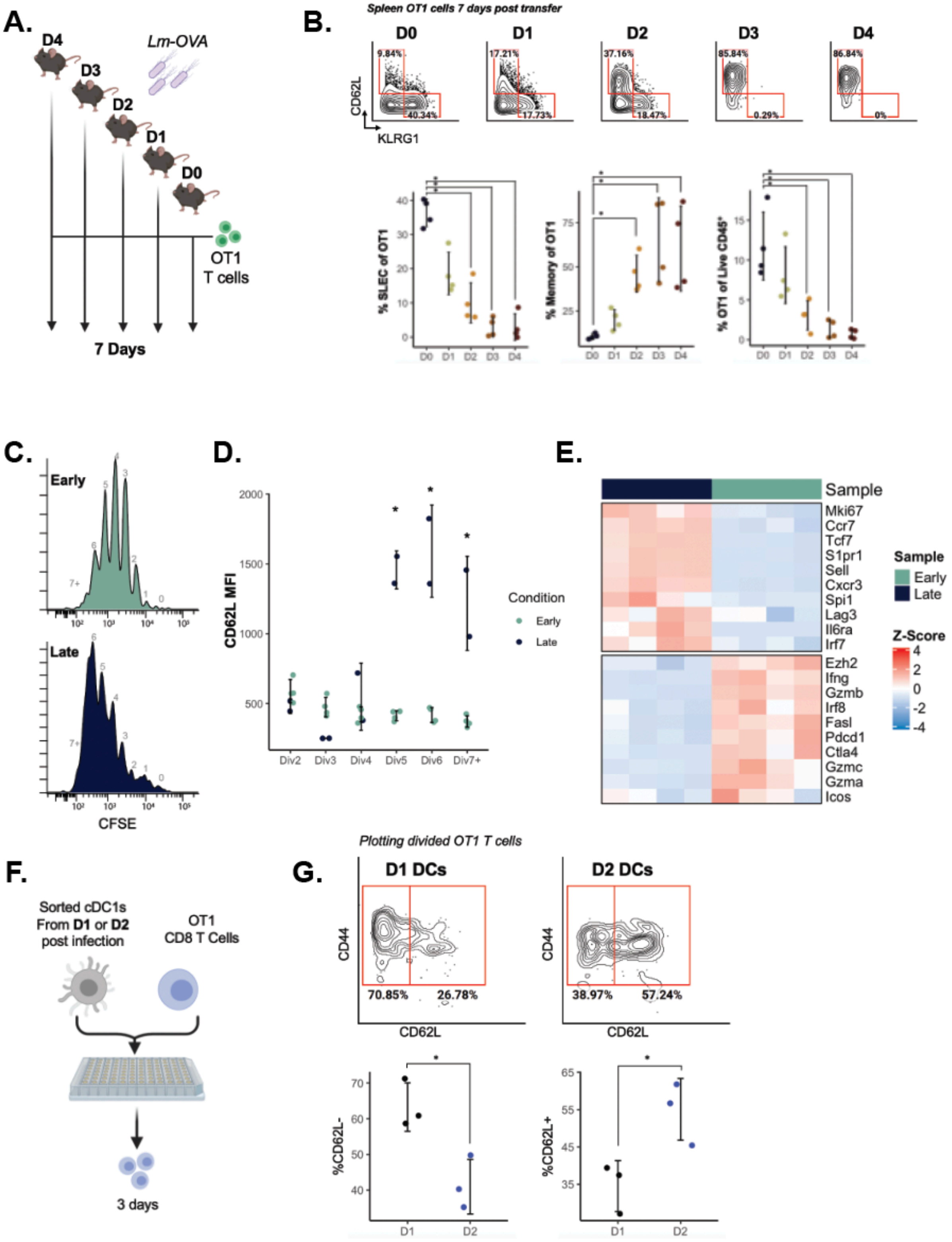

Figure 4-4: Late-arriving T cell acquire memory fate
(A) Schematic of experimental design to transfer OT1 T cells at different stages of infection with *LmOVA* and to analyze cells 7 days after transfer. **(B)** SLEC and Central

Memory cell gating and quantification of antigen specific cells 7 days after adoptive transfer. **(C)** CFSE dye dilution in OT1 T cells transferred at D0 (Early) or D3 (Late) and sorted 72 hours later. **(D)** Quantification of CD62L MFI on cells at specific numbers of divisions gated through CFSE dye stain. Significance $p<0.01$. **(E)** Heatmap of RNA-seq in early- and late-primed cells highlighting differentially expressed genes associated with memory and cytotoxic effector fates. **(F)** Schematic of experimental design to sort cDC1s from D1 or D2 post-infection, coculturing with naïve OT1 CD8 T cells and analyzing 3 days later. **(G)** Gating of CD44 and CD62L in representative divided OT1 T cells and quantification of CD62L$^+$ and CD62L$^-$ divided OT1 T cells.

4.7 Materials and Methods

Animals

All mice were housed in an American Association for the Accreditation of Laboratory Animal Care–accredited animal facility and maintained in specific pathogen-free conditions. Animal experiments were approved and conducted in accordance with AN157618. Wild-type female C57BL/6 mice and BoyJ CD45.1 between 8-10 weeks old were purchased from The Jackson Laboratory and housed at our facility. TCR Transgenic OT-I CD45.1 mice and heterozygous CD45.2,CD45.1 mice were bred at our facility. Animals were housed under standard SPF conditions with typical light/dark cycles and standard chow.

Infectious Agents

Listeria monocytogenes strain 10403s expressing OVA (Lm-OVA) was kindly provided by Shomyseh Sanjabi (UCSF). Lm-OVA stocks frozen at −80^{o} C were grown overnight at 37˚ C in BHI broth supplemented with 5 ug/ml erythromycin (Bio Basic, Amherst, New York). Then, overnight cultures were sub-cultured by diluting into fresh BHI broth supplemented with 5 ug/ml erythromycin and grown for 4 hours. Bacteria CFU was then quantified by measuring optical density at 600 nm. Bacteria were then diluted to 5×10^4 CFU / 100µl in sterile PBS and 100 µl was injected per mouse i.v. via the retroorbital vein.

Mass Cytometry Antibodies

Primary conjugates of mass cytometry antibodies were prepared using the MaxPAR antibody conjugation kit (Fluidigm, South San Francisco, CA) according to the manufacturer’s recommended protocol sourcing metals from Fluidigm (Fluidigm, South San Francisco, CA) or Trace Sciences International (Richmond Hill, Canada). Following labeling, antibodies were diluted in Candor PBS Antibody Stabilization solution (Candor Bioscience GmbH, Wangen, Germany) supplemented with 0.02% NaN_3 to between 0.1 and 0.3 mg/mL and stored long-term at 4° C. Each antibody clone and lot was titrated to optimal staining concentrations using primary mouse samples with all appropriate positive and negative controls.

Cell Preparation

All tissue preparations were performed simultaneously from each individual mouse, as previously reported (Spitzer et al. 2017). After euthanasia by CO_2 inhalation, spleens were collected and homogenized in PBS + 5 mM EDTA at 4° C. All tissues were washed with PBS/EDTA and re-suspended 1:1 with PBS/EDTA and 100 mM cisplatin (Enzo Life Sciences, Farmingdale, NY) for 60 s before quenching 1:1 with PBS/EDTA + 0.5% BSA to determine viability as previously described (Spitzer *et al.,* 2015). Cells were centrifuged at 500 x g for 5 min at 4° C and re-suspended in PBS/EDTA/BSA at a density between 1-10 x 10^6 cells/ml. Care was taken to maintain all samples at 4° C during all phases of tissue harvest and preparation except viability staining and fixation. Suspensions were fixed for 10 min at RT using 1.6% PFA in PBS (Fisher Scientific, Hampton, New Hampshire) and frozen at -80° C.

Mass-Tag Cellular Barcoding

Mass-tag cellular barcoding was performed as previously described (Zunder *et al.,* 2015). Briefly, 1 x 10^6 cells from each animal were barcoded with distinct combinations of stable Pd isotopes in 0.02% saponin in PBS. Samples from any given tissue from each mouse per experiment group were barcoded together. Cells were washed once with cell staining media (PBS with 0.5% BSA and 0.02% NaN_3), and once with 1X PBS, and pooled into a single FACS tube (BD Biosciences, San Jose, California). After data collection, each condition was deconvoluted using a single-cell debarcoding algorithm (Zunder *et al.,* 2015).

Mass Cytometry Staining and Measurement

Cells were resuspended in cell staining media (PBS with 0.5% BSA and 0.02% NaN_3), and antibodies against CD16 and CD32 (BioLegend, San Diego, California) were added at 20 μg/ml for 5 min at RT on a shaker to block Fc receptors. Surface marker antibodies were then added, yielding 500 uL final reaction volumes and stained for 30 min at RT on a shaker. Following staining, cells were washed 2 times with cell staining media, then permeabilized with methanol for at 10 min at 4° C. Cells were then washed twice in cell staining media to remove remaining methanol, and stained with intracellular antibodies in 500 uL for 1 hour at RT on a shaker. Cells were washed twice in cell staining media and then stained with 1 mL of 1:4000 191/193Ir DNA intercalator (Fluidigm, South San Francisco, CA) diluted in PBS with 4% PFA overnight. Cells were then washed once with cell staining media, once with PBS and once with Cell Acquisition Solution (Fluidigm, South San Francisco, CA). Care was taken to assure buffers preceding analysis were not contaminated with metals in the mass range above 100 Da. Mass cytometry samples were diluted in Cell Acquisition Solution containing bead standards (see below) to approximately 10^6 cells per mL and then analyzed on a Helios mass cytometer (Fluidigm, South San Francisco, CA) equilibrated with Cell Acquisition Solution. We analyzed 1-5 x 10^5 cells per animal per time point, consistent with generally accepted practices in the field. For adoptive transfer experiments, 1-4 x 10^6 cells per animal were analyzed.

Mass Cytometry Bead Standard Data Normalization

Data normalization was performed as previously described (Spitzer *et al.,* 2017). Briefly, just before analysis, the stained and intercalated cell pellet was resuspended in freshly prepared Cell Acquisition Solution containing the bead standard at a concentration ranging between 1 and 2 x 10^4 beads/ml. The mixture of beads and cells were filtered through a filter cap FACS tubes (BD Biosciences) before analysis. All mass cytometry files were normalized together using the mass cytometry data normalization algorithm (Finck *et al.,* 2013), which uses the intensity values of a sliding window of these bead standards to correct for instrument fluctuations over time and between samples.

Adoptive T Cell Transfer

For adoptive transfer of pathogen specific T cells to validate the antigen specificity of transitional cells, CD8 T cells were immunomagnetically enriched from the spleens of CD45.1 OT1 TCR transgenic mice with EasySep Streptavidin Negative Selection using the following biotinylated antibodies against: MHCII (AF6-120.1), CD11c (N418), Gr1 (RB6-8C5), B220 (RA3-6B2), CD4 (GK1.5), and Ter119 (TER-119). Viable cells were quantified by counting on a hemocytometer with trypan blue staining. 1×10^6 Cells were then resuspended in sterile PBS and transferred into naïve WT CD45.2 mice intravenously via the retroorbital vein. In some cases cells were also stained with CFSE.

Flow Cytometry, Cell Sorting

Cells were stained for viability with Zombie-NIR dye. Cell surface staining was performed in cell staining media (PBS with 0.5% BSA and 0.02% NaN_3) for 30 minutes at room temperature. The following anti-mouse antibodies were used: TCRβ – APC (H57-597), CD8 – PE (53-5.8), CD62L - BV421 (MEL-14), CD45.2 – PE-Cy7 (104), CD45.1 – FITC (A20), and CD19 – APC-Cy7,. (1D3/CD19). Stained cells were analyzed with an LSR II flow cytometer (BD Biosciences).

For sorting experiments, cells were prepared as described for flow cytometry and then sorted into lysis buffer (1X Takara single-cell lysis buffer) using a FACSAria II (BD Biosciences).

Statistical Analysis

All significance analysis was performed by paired or unpaired (as indicated) two-sided student's t-test in R.

Unsupervised Clustering Analysis and Data Visualization

Cell clusters were identified using the CLARA algorithm with 100 clusters as implemented in the 'cluster' package in R.

Data Availability

Mass cytometry data will be made publicly available as a report on Cytobank (www.cytobank.org) with linked flow cytometry standard (.fcs) files upon acceptance of the manuscript.

Chapter 5 Closing and Future Directions

Establishing that the peripheral immune macroenvironment is significantly perturbed in cancer has opened many potential new areas of investigation. Because Type 1 immune responses are blunted in the spleen of AT3 tumor-bearing mice, it would be prudent to evaluate these responses in other tumor models. Another essential question is to assess how Type 1 immune responses develop in non-lymphoid organs of tumor-bearing mice such as the response to *Lm* infection in the liver, lung, and tumor itself. Furthermore, it is important to continue deciphering the emergent properties of the tumor-burdened immune system by driving tumor *de novo* immune responses to a diverse range of challenges including vaccines, parasites, allergens, and commensals. Finally, the precise mechanisms that drive impaired DC activation remain elusive. Identifying whether this defect is intrinsic to precursor and mature DCs or rather driven by a secondary interaction is a sensible next step.

Single-cell metabolic analysis has also provided a new experimental toolset for many new potential areas of investigation[188]. The early-activated CD8 T cell state that uses oxidative phosphorylation and glycolysis simultaneously should be assessed in other diverse contexts such as in antiviral as well as natural and therapeutically induced antitumor responses. Furthermore, preliminary data suggest that CD4 T cells undergo a similar metabolic transition that requires experimental validation through orthogonal metabolic assays. This general technique of measuring metabolic state through antibodies targeting key metabolic mediators may also be applied to recent multimodal single cell technologies such as ASAP-seq, which combines single cell chromatin accessibility and intracellular quantification of antibody targets.

The precise timing of priming during infection and how infectious dose alters this also warrants further investigation. Preliminary data suggest that transient DC activation is not driven through transcriptional regulation ;therefore, this transient state may be regulated post-transcriptionally. Manipulating DC transience may provide a therapeutic approach to tune the type of T cell response elicited. Future studies may use chemokines or treatments to modulate T cell migration to optimize T cell responses to vaccines. Alternatively, vaccination through the implantation of synthetic antigen-loaded discs could be paired with migration modulators to facilitate memory T cell responses to cancer[189].

Together, these studies each interrogate key aspects of immunological coordination across diverse contexts. While immune responses have been studied at the single-cell level by flow cytometry for decades, the majority of previous studies have been technologically limited to only measuring fractions of immune cells, processes, and interactions. To advance basic and translational immunology, we must develop comprehensive maps of immune responses that delineate the full breadth and chronology of dynamic immune coordination. These three studies establish new experimental and computational frameworks for studying the development of multi-lineage immune responses over time. These frameworks can be applied to any complex immunological context to continue deciphering mysteries of basic immunology and informing rational design of therapeutics. Combining recent advances in single-cell multimodal (RNA+ATAC or Protein+ATAC or Protein+RNA) measurements with these frameworks will provide an unprecedented new window into the regulation of dynamic immune responses.

References

1. McAllister, S. S. & Weinberg, R. A. The tumour-induced systemic environment as a critical regulator of cancer progression and metastasis. *Nat. Cell Biol.* **16**, 717–727 (2014).
2. Hegde, P. S. & Chen, D. S. Top 10 Challenges in Cancer Immunotherapy. *Immunity* (2020) doi:10.1016/j.immuni.2019.12.011.
3. De Kleer, I., Willems, F., Lambrecht, B. & Goriely, S. Ontogeny of myeloid cells. *Front. Immunol.* (2014) doi:10.3389/fimmu.2014.00423.
4. Mempel, T. R., Henrickson, S. E. & Von Andrian, U. H. T-cell priming by dendritic cells in lymph nodes occurs in three distinct phases. *Nature* (2004) doi:10.1038/nature02238.
5. Hanahan, D. & Coussens, L. M. Accessories to the Crime: Functions of Cells Recruited to the Tumor Microenvironment. *Cancer Cell* (2012) doi:10.1016/j.ccr.2012.02.022.
6. Gabrilovich, D. I., Ostrand-Rosenberg, S. & Bronte, V. Coordinated regulation of myeloid cells by tumours. *Nature Reviews Immunology* (2012) doi:10.1038/nri3175.
7. Jaillon, S. *et al.* Neutrophil diversity and plasticity in tumour progression and therapy. *Nature Reviews Cancer* (2020) doi:10.1038/s41568-020-0281-y.
8. Canè, S. *et al.* The endless saga of monocyte diversity. *Frontiers in Immunology* (2019) doi:10.3389/fimmu.2019.01786.
9. Almand, B. *et al.* Increased Production of Immature Myeloid Cells in Cancer Patients: A Mechanism of Immunosuppression in Cancer. *J. Immunol.* (2001) doi:10.4049/jimmunol.166.1.678.
10. Casbon, A. J. *et al.* Invasive breast cancer reprograms early myeloid differentiation in the bone marrow to generate immunosuppressive neutrophils. *Proc. Natl. Acad. Sci. U. S. A.* (2015) doi:10.1073/pnas.1424927112.
11. Wu, W. C. *et al.* Circulating hematopoietic stem and progenitor cells are myeloid-biased in cancer patients. *Proc. Natl. Acad. Sci. U. S. A.* (2014) doi:10.1073/pnas.1320753111.

12. Kersten, K. *et al.* Mammary tumor-derived CCL2 enhances pro-metastatic systemic inflammation through upregulation of IL1β in tumor-associated macrophages. *Oncoimmunology* (2017) doi:10.1080/2162402X.2017.1334744.
13. Coffelt, S. B. *et al.* IL-17-producing γδ T cells and neutrophils conspire to promote breast cancer metastasis. *Nature* (2015) doi:10.1038/nature14282.
14. Shojaei, F. *et al.* G-CSF-initiated myeloid cell mobilization and angiogenesis mediate tumor refractoriness to anti-VEGF therapy in mouse models. *Proc. Natl. Acad. Sci. U. S. A.* (2009) doi:10.1073/pnas.0902280106.
15. Morales, J. K., Kmieciak, M., Knutson, K. L., Bear, H. D. & Manjili, M. H. GM-CSF is one of the main breast tumor-derived soluble factors involved in the differentiation of CD11b-Gr1-bone marrow progenitor cells into myeloid-derived suppressor cells. *Breast Cancer Res. Treat.* (2010) doi:10.1007/s10549-009-0622-8.
16. Bayne, L. J. *et al.* Tumor-Derived Granulocyte-Macrophage Colony-Stimulating Factor Regulates Myeloid Inflammation and T Cell Immunity in Pancreatic Cancer. *Cancer Cell* (2012) doi:10.1016/j.ccr.2012.04.025.
17. Raccosta, L. *et al.* The oxysterol-cxcr2 axis plays a key role in the recruitment of tumor-promoting neutrophils. *J. Exp. Med.* (2013) doi:10.1084/jem.20130440.
18. Dominguez, C., McCampbell, K. K., David, J. M. & Palena, C. Neutralization of IL-8 decreases tumor PMN-MDSCs and reduces mesenchymalization of claudin-low triple-negative breast cancer. *JCI Insight* (2017) doi:10.1172/jci.insight.94296.
19. Wellenstein, M. D. *et al.* Loss of p53 triggers WNT-dependent systemic inflammation to drive breast cancer metastasis. *Nature* (2019) doi:10.1038/s41586-019-1450-6.
20. Banchereau, J. *et al.* Immunobiology of dendritic cells. *Annual Review of Immunology* (2000) doi:10.1146/annurev.immunol.18.1.767.
21. Mastelic-Gavillet, B. *et al.* Quantitative and qualitative impairments in dendritic cell subsets of patients with ovarian or prostate cancer. *Eur. J. Cancer* (2020)

doi:10.1016/j.ejca.2020.04.036.

22. Santegoets, S. J. A. M. *et al.* Myeloid derived suppressor and dendritic cell subsets are related to clinical outcome in prostate cancer patients treated with prostate gvax and ipilimumab. *J. Immunother. Cancer* (2014) doi:10.1186/s40425-014-0031-3.

23. Della Bella, S. *et al.* Altered maturation of peripheral blood dendritic cells in patients with breast cancer. *Br. J. Cancer* (2003) doi:10.1038/sj.bjc.6601243.

24. Almand, B. *et al.* Clinical significance of defective dendritic cell differentiation in cancer. *Clin. Cancer Res.* (2000).

25. Failli, A., Legitimo, A., Orsini, G., Romanini, A. & Consolini, R. Numerical defect of circulating dendritic cell subsets and defective dendritic cell generation from monocytes of patients with advanced melanoma. *Cancer Lett.* (2013) doi:10.1016/j.canlet.2013.05.013.

26. Tabarkiewicz, J., Rybojad, P., Jablonka, A. & Rolinski, J. CD1c+ and CD303+ dendritic cells in peripheral blood, lymph nodes and tumor tissue of patients with non-small cell lung cancer. *Oncol. Rep.* (2008) doi:10.3892/or.19.1.237.

27. Van Cruijsen, H. *et al.* Sunitinib-induced myeloid lineage redistribution in renal cell cancer patients: CD1c+ dendritic cell frequency predicts progression-free survival. *Clin. Cancer Res.* (2008) doi:10.1158/1078-0432.CCR-08-0656.

28. Meyer, M. A. *et al.* Breast and pancreatic cancer interrupt IRF8-dependent dendritic cell development to overcome immune surveillance. *Nat. Commun.* (2018) doi:10.1038/s41467-018-03600-6.

29. Lin, J. H. *et al.* Type 1 conventional dendritic cells are systemically dysregulated early in pancreatic carcinogenesis. *J. Exp. Med.* (2020) doi:10.1084/jem.20190673.

30. Tjomsland, V. *et al.* Semi mature blood dendritic cells exist in patients with ductal pancreatic adenocarcinoma owing to inflammatory factors released from the tumor. *PLoS One* (2010) doi:10.1371/journal.pone.0013441.

31. Dudek, A. M., Martin, S., Garg, A. D. & Agostinis, P. Immature, semi-mature, and fully

mature dendritic cells: Toward a DC-cancer cells interface that augments anticancer immunity. *Frontiers in Immunology* (2013) doi:10.3389/fimmu.2013.00438.

32. Ray-Coquard, I. *et al.* Lymphopenia as a prognostic factor for overall survival in advanced carcinomas, sarcomas, and lymphomas. *Cancer Res.* (2009) doi:10.1158/0008-5472.CAN-08-3845.
33. Manuel, M. *et al.* Lymphopenia combined with low TCR diversity (divpenia) predicts poor overall survival in metastatic breast cancer patients. *Oncoimmunology* (2012) doi:10.4161/onci.19545.
34. Liu, Y. Y. *et al.* Characteristics and prognostic significance of profiling the peripheral blood T-cell receptor repertoire in patients with advanced lung cancer. *Int. J. Cancer* (2019) doi:10.1002/ijc.32145.
35. Cui, J. H. *et al.* TCR repertoire as a novel indicator for immune monitoring and prognosis assessment of patients with cervical cancer. *Front. Immunol.* (2018) doi:10.3389/fimmu.2018.02729.
36. Tumeh, P. C. *et al.* PD-1 blockade induces responses by inhibiting adaptive immune resistance. *Nature* (2014) doi:10.1038/nature13954.
37. Verronèse, E. *et al.* Immune cell dysfunctions in breast cancer patients detected through whole blood multi-parametric flow cytometry assay. *Oncoimmunology* (2016) doi:10.1080/2162402X.2015.1100791.
38. Wang, L. *et al.* IL6 signaling in peripheral blood T cells predicts clinical outcome in breast cancer. *Cancer Res.* (2017) doi:10.1158/0008-5472.CAN-16-1373.
39. Wolf, A. M. *et al.* Increase of regulatory T cells in the peripheral blood of cancer patients. *Clin. Cancer Res.* (2003).
40. Ahmadzadeh, M. *et al.* Tumor-infiltrating human CD4+ regulatory T cells display a distinct TCR repertoire and exhibit tumor and neoantigen reactivity. *Sci. Immunol.* (2019) doi:10.1126/sciimmunol.aao4310.

41. Wang, L. *et al.* Connecting blood and intratumoral Treg cell activity in predicting future relapse in breast cancer. *Nat. Immunol.* (2019) doi:10.1038/s41590-019-0429-7.

42. Shimasaki, N., Jain, A. & Campana, D. NK cells for cancer immunotherapy. *Nature Reviews Drug Discovery* (2020) doi:10.1038/s41573-019-0052-1.

43. Mamessier, E. *et al.* Human breast cancer cells enhance self tolerance by promoting evasion from NK cell antitumor immunity. *J. Clin. Invest.* (2011) doi:10.1172/JCI45816.

44. Mathios, D. *et al.* Anti-PD-1 antitumor immunity is enhanced by local and abrogated by systemic chemotherapy in GBM. *Sci. Transl. Med.* (2016) doi:10.1126/scitranslmed.aag2942.

45. Broz, M. L. *et al.* Dissecting the Tumor Myeloid Compartment Reveals Rare Activating Antigen-Presenting Cells Critical for T Cell Immunity. *Cancer Cell* (2014) doi:10.1016/j.ccell.2014.09.007.

46. Roberts, E. W. *et al.* Critical Role for CD103+/CD141+ Dendritic Cells Bearing CCR7 for Tumor Antigen Trafficking and Priming of T Cell Immunity in Melanoma. *Cancer Cell* (2016) doi:10.1016/j.ccell.2016.06.003.

47. Salmon, H. *et al.* Expansion and Activation of CD103+ Dendritic Cell Progenitors at the Tumor Site Enhances Tumor Responses to Therapeutic PD-L1 and BRAF Inhibition. *Immunity* (2016) doi:10.1016/j.immuni.2016.03.012.

48. Spranger, S., Dai, D., Horton, B. & Gajewski, T. F. Tumor-Residing Batf3 Dendritic Cells Are Required for Effector T Cell Trafficking and Adoptive T Cell Therapy. *Cancer Cell* (2017) doi:10.1016/j.ccell.2017.04.003.

49. Spitzer, M. H. *et al.* Systemic Immunity Is Required for Effective Cancer Immunotherapy. *Cell* (2017) doi:10.1016/j.cell.2016.12.022.

50. Fransen, M. F. & Van Hall, T. Tumor-draining lymph nodes are pivotal in PD-1/PD-L1 checkpoint therapy. *JCI Insight* **3**, e124507 (2018).

51. Philip, M. *et al.* Chromatin states define tumour-specific T cell dysfunction and

reprogramming. *Nature* **545**, 452–456 (2017).

52. Scott, A. C. *et al.* TOX is a critical regulator of tumour-specific T cell differentiation. *Nature* **571**, 270–274 (2019).
53. Khan, O. *et al.* TOX transcriptionally and epigenetically programs CD8+ T cell exhaustion. *Nature* **571**, 211–218 (2019).
54. Yost, K. E. *et al.* Clonal replacement of tumor-specific T cells following PD-1 blockade. *Nat. Med.* (2019) doi:10.1038/s41591-019-0522-3.
55. Wu, T. D. *et al.* Peripheral T cell expansion predicts tumour infiltration and clinical response. *Nature* (2020) doi:10.1038/s41586-020-2056-8.
56. Valpione, S. *et al.* Immune awakening revealed by peripheral T cell dynamics after one cycle of immunotherapy. *Nat. Cancer* (2020) doi:10.1038/s43018-019-0022-x.
57. Rahil, Z. *et al.* Landscape of coordinated immune responses to H1N1 challenge in humans. *J. Clin. Invest.* (2020) doi:10.1172/jci137265.
58. Kotliar, D. *et al.* Single-cell profiling of Ebola virus infection in vivo reveals viral and host transcriptional dynamics. 1–19 (2020) doi:10.1101/2020.06.12.148957.
59. Eisenbarth, S. C. Dendritic cell subsets in T cell programming: location dictates function. *Nature Reviews Immunology* (2019) doi:10.1038/s41577-018-0088-1.
60. Taniuchi, I. CD4 Helper and CD8 Cytotoxic T Cell Differentiation. *Annu. Rev. Immunol.* (2018) doi:10.1146/annurev-immunol-042617-053411.
61. Buchholz, V. R. *et al.* Disparate individual fates compose robust CD8+ T cell immunity. *Science (80-.).* (2013) doi:10.1126/science.1235454.
62. Grassmann, S. *et al.* Early emergence of T central memory precursors programs clonal dominance during chronic viral infection. *Nat. Immunol.* (2020) doi:10.1038/s41590-020-00807-y.
63. Osborne, L. C. *et al.* Virus-helminthcoinfection reveals a microbiota-independent mechanism of immunomodulation. *Science (80-.).* (2014) doi:10.1126/science.1256942.

64. Barnstorf, I. *et al.* Chronic virus infection compromises memory bystander T cell function in an IL-6/ STAT1-dependent manner. *J. Exp. Med.* (2019) doi:10.1084/jem.20181589.

65. Snell, L. M. *et al.* CD8+ T Cell Priming in Established Chronic Viral Infection Preferentially Directs Differentiation of Memory-like Cells for Sustained Immunity. *Immunity* (2018) doi:10.1016/j.immuni.2018.08.002.

66. Kamboj, M. & Sepkowitz, K. A. Nosocomial infections in patients with cancer. *The Lancet Oncology* (2009) doi:10.1016/S1470-2045(09)70069-5.

67. Wong, A., Marrie, T. J., Garg, S., Kellner, J. D. & Tyrrell, G. J. Increased risk of invasive pneumococcal disease in haematological and solid-organ malignancies. *Epidemiol. Infect.* (2010) doi:10.1017/S0950268810000919.

68. Liang, W. *et al.* Cancer patients in SARS-CoV-2 infection: a nationwide analysis in China. *The Lancet Oncology* (2020) doi:10.1016/S1470-2045(20)30096-6.

69. Kuderer, N. M. *et al.* Clinical impact of COVID-19 on patients with cancer (CCC19): a cohort study. *Lancet* (2020) doi:10.1016/S0140-6736(20)31187-9.

70. Mittal, R. *et al.* Phenotypic T cell exhaustion in a murine model of bacterial infection in the setting of pre-existing malignancy. *PLoS One* (2014) doi:10.1371/journal.pone.0093523.

71. Russ, A. J. *et al.* Melanoma-induced suppression of tumor antigen-specific T cell expansion is comparable to suppression of global T cell expansion. *Cell. Immunol.* (2011) doi:10.1016/j.cellimm.2011.06.011.

72. Fransen, M. F. *et al.* Tumor-draining lymph nodes are pivotal in PD-1/PD-L1 checkpoint therapy. *JCI insight* (2018) doi:10.1172/jci.insight.124507.

73. Tang, H. *et al.* PD-L1 on host cells is essential for PD-L1 blockade-mediated tumor regression. *J Clin Invest* **128**, 580–588 (2018).

74. Curiel, T. J. *et al.* Blockade of B7-H1 improves myeloid dendritic cell-mediated antitumor immunity. *Nat. Med.* **9**, 562–567 (2003).

75. Chamoto, K. *et al.* Mitochondrial activation chemicals synergize with surface receptor PD-

1 blockade for T cell-dependent antitumor activity. *PNAS* **114**, E761–E770 (2017).

76. Lin, H. *et al.* Host expression of PD-L1 determines efficacy of PD-L1 pathway blockade–mediated tumor regression. *J. Clin. Invest.* **128**, 805–815 (2018).

77. Zhang, S. *et al.* The Role of Myeloid-Derived Suppressor Cells in Patients with Solid Tumors: A Meta-Analysis. *PLoS One* **11**, e0164514 (2016).

78. Osborne, L. C. *et al.* Virus-helminth coinfection reveals a microbiota-independent mechanism of immunomodulation. *Science (80-.).* **345**, 578–582 (2014).

79. Danna, E. A. *et al.* Surgical Removal of Primary Tumor Reverses Tumor-Induced Immunosuppression Despite the Presence of Metastatic Disease. *Cancer Res.* **64**, 2205–2211 (2004).

80. Ghochikyan, A. *et al.* Primary 4T1 tumor resection provides critical “window of opportunity” for immunotherapy. *Clin Exp Metastasis* **31**, 185–198 (2014).

81. Mosely, S. I. S. *et al.* Rational Selection of Syngeneic Preclinical Tumor Models for Immunotherapeutic Drug Discovery. *Cancer Immunol Res* **5**, 29–41 (2017).

82. Westcott, P. M. K. *et al.* The mutational landscapes of genetic and chemical models of Kras-driven lung cancer. *Nature* **517**, 489–492 (2015).

83. Zeitouni, B. *et al.* Abstract 1840: Whole-exome somatic mutation analysis of mouse cancer models and implications for preclinical immunomodulatory drug development. in *Proceedings of the 107th Annual Meeting of the American Association for Cancer Research* (2017). doi:10.1158/1538-7445.AM2017-1840.

84. Heinzel, F. P., Sadick, M. D., Holaday, B. J., Coffman, R. L. & Locksley, R. M. Reciprocal expression of interferon gamma or interleukin 4 during the resolution or progression of murine leishmaniasis. Evidence for expansion of distinct helper T cell subsets. *J. Exp. Med.* **169**, 59–72 (1989).

85. Kather, J. N. *et al.* Topography of cancer-associated immune cells in human solid tumors. *Elife* **7**, (2018).

86. Spitzer, M. H. *et al.* An interactive reference framework for modeling a dynamic immune system. *Science (80-.).* **349**, 1259425 (2015).
87. Anz, D. *et al.* CD103 is a hallmark of tumor-infiltrating regulatory T cells. *Int. J. Cancer* **129**, 2417–2426 (2011).
88. Ross, E. A. *et al.* CD31 is required on CD4 + T cells to promote T cell survival during Salmonella infection. *J. Immunol.* **187**, 1553–1565 (2011).
89. Hänninen, A., Maksimow, M., Alam, C., Morgan, D. J. & Jalkanen, S. Ly6C supports preferential homing of central memory CD8+ T cells into lymph nodes. *Eur. J. Immunol.* **41**, 634–644 (2011).
90. Fourcade, J. *et al.* Upregulation of Tim-3 and PD-1 expression is associated with tumor antigen–specific CD8+ T cell dysfunction in melanoma patients. *J. Exp. Med.* **207**, 2175–2186 (2010).
91. Mita, Y. *et al.* Crucial role of CD69 in anti-tumor immunity through regulating the exhaustion of tumor-infiltrating T cells. *Int. Immunol.* **30**, 559–567 (2018).
92. Sun, C., Mezzadra, R. & Schumacher, T. N. Regulation and Function of the PD-L1 Checkpoint. *Immunity* **48**, 434–452 (2018).
93. Bianchini, M. *et al.* PD-L1 expression on nonclassical monocytes reveals their origin and immunoregulatory function. *Sci. Immunol.* **4**, eaar3054 (2019).
94. Busch, D. H., Pilip, I. M., Vijh, S. & Pamer, E. G. Coordinate regulation of complex T cell populations responding to bacterial infection. *Immunity* **8**, 353–362 (1998).
95. Kaech, S. M. & Ahmed, R. Memory CD8 + T cell differentiation: initial antigen encounter triggers a developmental program in naïve cells. *Nat. Immunol.* **2**, 415–422 (2001).
96. Herndler-Brandstetter, D. *et al.* KLRG1+ Effector CD8+ T Cells Lose KLRG1, Differentiate into All Memory T Cell Lineages, and Convey Enhanced Protective Immunity. *Immunity* **48**, 716–729 (2018).
97. Jung, S. *et al.* In vivo depletion of CD11c+ dendritic cells abrogates priming of CD8+ T

cells by exogenous cell-associated antigens. *Immunity* **17**, 211–220 (2002).

98. Gabrilovich, D. I., Corak, J., Ciernik, I. F., Kavanaugh, D. & Carbone, D. P. Decreased antigen presentation by dendritic cells in patients with breast cancer. *Clin. Cancer Res.* **3**, 483–490 (1997).

99. Wu, W.-C. *et al.* Circulating hematopoietic stem and progenitor cells are myeloid-biased in cancer patients. *Proc. Natl. Acad. Sci.* **111**, 4221–4226 (2014).

100. Apte, R. N. *et al.* Effects of micro-environment- and malignant cell-derived interleukin-1 in carcinogenesis, tumour invasiveness and tumour-host interactions. *Eur. J. Cancer* **42**, 751–759 (2006).

101. Wu, T. C. *et al.* IL1 receptor antagonist controls transcriptional signature of inflammation in patients with metastatic breast cancer. *Cancer Res.* **78**, 5243–5258 (2018).

102. Singer, C. F. *et al.* Interleukin-1alpha protein secretion in breast cancer is associated with poor differentiation and estrogen receptor alpha negativity. *Int. J. Gynecol. Cancer* **16**, 556–559 (2006).

103. Pickup, M., Novitskiy, S. & Moses, H. L. The roles of TGFβ in the tumour microenvironment. *Nat. Rev. Cancer* **13**, 788–799 (2013).

104. Mariathasan, S. *et al.* TGFβ attenuates tumour response to PD-L1 blockade by contributing to exclusion of T cells. *Nature* **554**, 544–548 (2018).

105. Suzuki, A. *et al.* IL-1 production as a regulator of G-CSF and IL-6 production in CSF-producing cell lines. *Br. J. Cancer* **65**, 515–518 (1992).

106. Mittal, R., Wagener, M., Breed, E. R., Liang, Z. & Yoseph, B. P. Phenotypic T Cell Exhaustion in a Murine Model of Bacterial Infection in the Setting of Pre-Existing Malignancy. *PLoS One* **9**, 93523 (2014).

107. Xie, J. *et al.* Pre-existing malignancy results in increased prevalence of distinct populations of CD4+ T cells during sepsis. *PLoS One* **13**, e0191065 (2018).

108. Klastersky, J. & Aoun, M. Opportunistic infections in patients with cancer. *Ann. Oncol.* **15**,

iv329–iv335 (2004).

109. Baluch, A. & Pasikhova, Y. Influenza Vaccination in Oncology Patients. *Curr Infect Dis Rep* **15**, 486–490 (2013).

110. O'Hara, M. H. *et al.* Abstract CT004: A Phase Ib study of CD40 agonistic monoclonal antibody APX005M together with gemcitabine (Gem) and nab-paclitaxel (NP) with or without nivolumab (Nivo) in untreated metastatic ductal pancreatic adenocarcinoma (PDAC) patients. in *Cancer Research* vol. 79 CT004–CT004 (American Association for Cancer Research (AACR), 2019).

111. Zuckerman, N. S. *et al.* Altered local and systemic immune profiles underlie lymph node metastasis in breast cancer patients. *Int. J. Cancer* **132**, 2537–2547 (2012).

112. Kosaka, A., Ohkuri, T., Program, B. T. & Okada, H. Combination of an agonistic anti-CD40 monoclonal antibody and the COX-2 inhibitor celecoxib induces anti-glioma effects by promotion of type-1 immunity in myeloid cells and T-cells. *Cancer Immunol Immunother* **63**, 847–857 (2014).

113. Tseng, W. W. *et al.* Development of an orthotopic model of invasive pancreatic cancer in an immunocompetent murine host. *Clin. Cancer Res.* **16**, 3684–3695 (2010).

114. Kathryn E. Foulds, Lauren A. Zenewicz, Devon J. Shedlock, J. J. & Amy E. Troy, and H. S. Cutting Edge: CD4 and CD8 T Cells Are Intrinsically Different in Their Proliferative Responses. *J Immunol* **168**, 1528–1532 (2002).

115. Zunder, E. R. *et al.* Palladium-based Mass-Tag Cell Barcoding with a Doublet-Filtering Scheme and Single Cell Deconvolution Algorithm. *Nat. Protoc.* **10**, 316–333 (2015).

116. Finck, R. *et al.* Normalization of mass cytometry data with bead standards. *Cytom. Part A* **83 A**, 483–494 (2013).

117. Bair, E. & Tibshirani, R. Semi-Supervised Methods to Predict Patient Survival from Gene Expression Data. *PLoS Biol.* **2**, 0511–0522 (2004).

118. Dumeaux, V. *et al.* Interactions between the tumor and the blood systemic response of

breast cancer patients. *PLoS Comput. Biol.* **13**, (2017).

119. Aran, D., Hu, Z. & Butte, A. J. xCell: digitally portraying the tissue cellular heterogeneity landscape. *Genome Biol.* **18**, 1–14 (2017).

120. Buck, M. D., Sowell, R. T., Kaech, S. M. & Pearce, E. L. Metabolic Instruction of Immunity. *Cell* **169**, 570–586 (2017).

121. Restifo, N. P., Dudley, M. E. & Rosenberg, S. A. Adoptive immunotherapy for cancer: Harnessing the T cell response. *Nat. Rev. Immunol.* **12**, 269–281 (2012).

122. Callahan, M. K., Postow, M. A. & Wolchok, J. D. Targeting T Cell Co-receptors for Cancer Therapy. *Immunity* **44**, 1069–1078 (2016).

123. Badovinac, V. P., Haring, J. S. & Harty, J. T. Initial T Cell Receptor Transgenic Cell Precursor Frequency Dictates Critical Aspects of the CD8+ T Cell Response to Infection. *Immunity* (2007) doi:10.1016/j.immuni.2007.04.013.

124. Araki, K. *et al.* HHS Public Access. **460**, 108–112 (2010).

125. Pearce, E. L. *et al.* Enhancing CD8 T-cell memory by modulating fatty acid metabolism. *Nature* **460**, 103–107 (2009).

126. Gerriets, V. A. & Rathmell, J. C. Metabolic pathways in T cell fate and function. *Trends Immunol.* **33**, 168–173 (2012).

127. Zhang, L. & Romero, P. Metabolic Control of CD8 + T Cell Fate Decisions and Antitumor Immunity. *Trends Mol. Med.* **24**, (2017).

128. Olenchock, B. A., Rathmell, J. C. & Vander Heiden, M. G. Biochemical Underpinnings of Immune Cell Metabolic Phenotypes. *Immunity* **46**, 703–713 (2017).

129. Wang, R. *et al.* The Transcription Factor Myc Controls Metabolic Reprogramming upon T Lymphocyte Activation. *Immunity* (2011) doi:10.1016/j.immuni.2011.09.021.

130. Calderon, M. J. *et al.* 4-1BB costimulation induces T cell mitochondrial function and biogenesis enabling cancer immunotherapeutic responses. *J. Exp. Med.* **215**, 1091–1100 (2018).

131. Menk, A. V. *et al.* Early TCR Signaling Induces Rapid Aerobic Glycolysis Enabling Distinct Acute T Cell Effector Functions. *Cell Rep.* **22**, 1509–1521 (2018).

132. Lee, J. *et al.* Regulator of fatty acid metabolism, acetyl coenzyme a carboxylase 1, controls T cell immunity. *J. Immunol.* **192**, 3190–3199 (2014).

133. Buck, M. D. D. *et al.* Mitochondrial Dynamics Controls T Cell Fate through Metabolic Programming. *Cell* **166**, 63–76 (2016).

134. Borges da Silva, H. *et al.* The purinergic receptor P2RX7 directs metabolic fitness of long-lived memory CD8(+) T cells. *Nature* **559**, 264–268 (2018).

135. D'Souza, A. D., Parikh, N., Kaech, S. M. & Shadel, G. S. Convergence of multiple signaling pathways is required to coordinately up-regulate mtDNA and mitochondrial biogenesis during T cell activation. *Mitochondrion* **7**, 374–385 (2007).

136. Andrejeva, G. & Rathmell, J. C. Similarities and Distinctions of Cancer and Immune Metabolism in Inflammation and Tumors. *Cell Metab.* **26**, 49–70 (2017).

137. van der Windt, G. J. W. *et al.* Mitochondrial Respiratory Capacity Is a Critical Regulator of CD8+T Cell Memory Development. *Immunity* **36**, 68–78 (2012).

138. Joshi, N. S. *et al.* Inflammation Directs Memory Precursor and Short-Lived Effector CD8+ T Cell Fates via the Graded Expression of T-bet Transcription Factor. *Immunity* (2007) doi:10.1016/j.immuni.2007.07.010.

139. Kalia, V. *et al.* Prolonged Interleukin-2Rα Expression on Virus-Specific CD8+ T Cells Favors Terminal-Effector Differentiation In Vivo. *Immunity* (2010) doi:10.1016/j.immuni.2009.11.010.

140. Obar, J. J. & Lefrançois, L. Early Signals during CD8 + T Cell Priming Regulate the Generation of Central Memory Cells . *J. Immunol.* (2010) doi:10.4049/jimmunol.1000492.

141. Mingueneau, M. *et al.* Single-cell mass cytometry of TCR signaling: Amplification of small initial differences results in low ERK activation in NOD mice. *Proc. Natl. Acad. Sci.* **111**, 16466–16471 (2014).

142. Krishnaswamy, S. *et al.* Conditional density-based analysis of T cell signaling in single-cell data. *Science (80-.).* **346**, 1250689–1250689 (2014).

143. Ma, E. H. *et al.* Metabolic Profiling Using Stable Isotope Tracing Reveals Distinct Patterns of Glucose Utilization by Physiologically Activated CD8+ T Cells. *Immunity* 1–15 (2019) doi:10.1016/j.immuni.2019.09.003.

144. Bandura, D. R. *et al.* Mass Cytometry: Technique for Real Time Single Cell Multitarget Immunoassay Based on Inductively Coupled Plasma Time-of-Flight Mass Spectrometry. *Anal. Chem.* **81**, 6813–6822 (2009).

145. Bendall, S. C. *et al.* Single-cell mass cytometry of differential immune and drug responses across a human hematopoietic continuum. *Science (80-.).* **332**, 687–696 (2011).

146. Bodenmiller, B. *et al.* Multiplexed mass cytometry profiling of cellular states perturbed by small-molecule regulators. *Nat. Biotechnol.* **30**, 858–867 (2012).

147. Good, Z. *et al.* Proliferation tracing with single-cell mass cytometry optimizes generation of stem cell memory-like T cells. *Nat. Biotechnol.* (2019) doi:10.1038/s41587-019-0033-2.

148. Cheung, P. *et al.* Single-Cell Chromatin Modification Profiling Reveals Increased Epigenetic Variations with Aging. *Cell* **173**, 1385-1397.e14 (2018).

149. McGregor, D. D., Koster, F. T. & Mackaness, G. B. Biological sciences: The short lived small lymphocyte as a mediator of cellular immunity. *Nature* **228**, 855–856 (1970).

150. Pollizzi, K. N. *et al.* mTORC1 and mTORC2 selectively regulate CD8+ T cell differentiation. *J. Clin. Invest.* **125**, 2090–2108 (2015).

151. Dennis, M. K. *et al.* Postranscriptional control of T cell effector function by aerobic glycolysis. *Cell* **127**, 358–366 (2012).

152. Wiegand, G. & Remington, S. J. CITRATE SYNTHASE: Structure, Control, and Mechanism. *Annu. Rev. Biophys. Biophys. Chem.* **15**, 97–117 (1986).

153. Ren, W. *et al.* Amino-acid transporters in T-cell activation and differentiation. *Cell Death*

Dis. **8**, 1–9 (2017).

154. Hayashi, K., Jutabha, P., Endou, H., Sagara, H. & Anzai, N. LAT1 Is a Critical Transporter of Essential Amino Acids for Immune Reactions in Activated Human T Cells. *J. Immunol.* **191**, 4080 LP – 4085 (2013).

155. Nii, T. *et al.* amino acid transporter LAT1 during T-cell activation. *Reactions* **704**, 693–704 (2001).

156. Sinclair, L. V *et al.* Control of amino-acid transport by antigen receptors coordinates the metabolic reprogramming essential for T cell differentiation. *Nat. Immunol.* **14**, 500–508 (2013).

157. Carpenter, K., Pollitt, R. J. & Middleton, B. Human liver long-chain 3-hydroxyacyl-coenzyme a dehydrogenase is a multifunctional membrane-bound beta-oxidation enzyme of mitochondria. *Biochem. Biophys. Res. Commun.* **183**, 443–448 (1992).

158. Howie, D., Ten Bokum, A., Necula, A. S., Cobbold, S. P. & Waldmann, H. The Role of Lipid Metabolism in T Lymphocyte Differentiation and Survival . *Frontiers in Immunology* vol. 8 1949 (2018).

159. Cunningham, C. A., Hoppins, S. & Fink, P. J. Cutting Edge: Glycolytic Metabolism and Mitochondrial Metabolism Are Uncoupled in Antigen-Activated CD8 + Recent Thymic Emigrants . *J. Immunol.* **201**, 1627–1632 (2018).

160. Tarze, A. *et al.* GAPDH, a novel regulator of the pro-apoptotic mitochondrial membrane permeabilization. *Oncogene* **26**, 2606–2620 (2007).

161. Enamorado, M. *et al.* Mitochondrial Morphological and Functional Reprogramming Following CD137 (4-1BB) Costimulation. *Cancer Immunol. Res.* **6**, 798–811 (2018).

162. Laforge, M. *et al.* NF-κB pathway controls mitochondrial dynamics. *Cell Death Differ.* **23**, 89–98 (2016).

163. Feske, S. Calcium signalling in lymphocyte activation and disease. *Nat. Rev. Immunol.* **7**, 690–702 (2007).

164. Fracchia, K. M., Pai, C. Y. & Walsh, C. M. Modulation of T Cell Metabolism and Function through Calcium Signaling. *Front. Immunol.* **4**, 1–11 (2013).

165. Gray, S. M., Amezquita, R. A., Guan, T., Kleinstein, S. H. & Kaech, S. M. Polycomb Repressive Complex 2-Mediated Chromatin Repression Guides Effector CD8+ T Cell Terminal Differentiation and Loss of Multipotency. *Immunity* (2017) doi:10.1016/j.immuni.2017.03.012.

166. Chisolm, D. A. *et al.* CCCTC-Binding Factor Translates Interleukin 2- and α-Ketoglutarate-Sensitive Metabolic Changes in T Cells into Context-Dependent Gene Programs. *Immunity* **47**, 251-267.e7 (2017).

167. Carrio, R., Bathe, O. F. & Malek, T. R. Initial Antigen Encounter Programs CD8+ T Cells Competent to Develop into Memory Cells That Are Activated in an Antigen-Free, IL-7- and IL-15-Rich Environment. *J. Immunol.* **172**, 7315–7323 (2014).

168. Jiang, J., Lau, L. L. & Shen, H. Selective Depletion of Nonspecific T Cells During the Early Stage of Immune Responses to Infection. *J. Immunol.* (2003) doi:10.4049/jimmunol.171.8.4352.

169. Chu, T. *et al.* Bystander-Activated Memory CD8 T Cells Control Early Pathogen Load in an Innate-like, NKG2D-Dependent Manner. *Cell Rep.* (2013) doi:10.1016/j.celrep.2013.02.020.

170. O'Sullivan, D. *et al.* Memory CD8$^+$ T Cells Use Cell-Intrinsic Lipolysis to Support the Metabolic Programming Necessary for Development. *Immunity* **41**, 75–88 (2014).

171. Zeng, H. *et al.* mTORC1 and mTORC2 Kinase Signaling and Glucose Metabolism Drive Follicular Helper T Cell Differentiation. *Immunity* **45**, 540–554 (2016).

172. Spitzer, M. H. & Nolan, G. P. Mass Cytometry: Single Cells, Many Features. *Cell* **165**, 780–791 (2016).

173. Zunder, E. R., Lujan, E., Goltsev, Y., Wernig, M. & Nolan, G. P. A continuous molecular roadmap to iPSC reprogramming through progression analysis of single-cell mass

cytometry. *Cell Stem Cell* **16**, 323–337 (2015).

174. Bendall, S. C. *et al.* Single-Cell Trajectory Detection Uncovers Progression and Regulatory Coordination in Human B Cell Development. *Cell* **157**, 714–725 (2014).

175. Sukumar, M. *et al.* Inhibiting glycolytic metabolism enhances CD8+ T cell memory and antitumor function. *J. Clin. Invest.* **123**, 4479–4488 (2013).

176. Sullivan, D. O. *et al.* Memory CD8+ T Cells use cell intrinsic lipolysis. *Immunity* **41**, 75–88 (2014).

177. Cantor, J. R. *et al.* Physiologic Medium Rewires Cellular Metabolism and Reveals Uric Acid as an Endogenous Inhibitor of UMP Synthase. *Cell* **169**, 258-272.e17 (2017).

178. van der Windt, G. J. W., Chang, C.-H. & Pearce, E. L. Measuring Bioenergetics in T Cells Using a Seahorse Extracellular Flux Analyzer. *Curr. Protoc. Immunol.* **113**, 3.16B.1-3.16B.14 (2016).

179. Klein Geltink, R. I. *et al.* Mitochondrial Priming by CD28. *Cell* **171**, 385-397.e11 (2017).

180. Quigley, M., Huang, X. & Yang, Y. Extent of Stimulation Controls the Formation of Memory CD8 T Cells. *J. Immunol.* (2007) doi:10.4049/jimmunol.179.9.5768.

181. Catron, D. M., Rusch, L. K., Hataye, J., Itano, A. A. & Jenkins, M. K. CD4+ T cells that enter the draining lymph nodes after antigen injection participate in the primary response and become central-memory cells. *J. Exp. Med.* (2006) doi:10.1084/jem.20051954.

182. Porter, B. B. & Harty, J. T. The onset of CD8+-T-cell contraction is influenced by the peak of Listeria monocytogenes infection and antigen display. *Infect. Immun.* (2006) doi:10.1128/IAI.74.3.1528-1536.2006.

183. Edelson, B. T. *et al.* CD8α+ Dendritic Cells Are an Obligate Cellular Entry Point for Productive Infection by Listeria monocytogenes. *Immunity* (2011) doi:10.1016/j.immuni.2011.06.012.

184. Bromberg, J. F., Horvath, C. M., Wen, Z., Schreiber, R. D. & Darnell, J. E. Transcriptionally active Stat1 is required for the antiproliferative effects of both interferon

α and interferon γ. *Proc. Natl. Acad. Sci. U. S. A.* (1996) doi:10.1073/pnas.93.15.7673.

185. Kadoki, M. *et al.* Organism-Level Analysis of Vaccination Reveals Networks of Protection across Tissues. *Cell* (2017) doi:10.1016/j.cell.2017.08.024.

186. Norris, B. A. *et al.* Chronic but Not Acute Virus Infection Induces Sustained Expansion of Myeloid Suppressor Cell Numbers that Inhibit Viral-Specific T Cell Immunity. *Immunity* (2013) doi:10.1016/j.immuni.2012.10.022.

187. Delale, T. *et al.* MyD88-Dependent and -Independent Murine Cytomegalovirus Sensing for IFN-α Release and Initiation of Immune Responses In Vivo. *J. Immunol.* (2005) doi:10.4049/jimmunol.175.10.6723.

188. Artyomov, M. N. & Van den Bossche, J. Immunometabolism in the Single-Cell Era. *Cell Metabolism* (2020) doi:10.1016/j.cmet.2020.09.013.

189. Ali, O. A., Emerich, D., Dranoff, G. & Mooney, D. J. In situ regulation of DC subsets and T cells mediates tumor regression in mice. *Sci. Transl. Med.* (2009) doi:10.1126/scitranslmed.3000359.

Publishing Agreement

It is the policy of the University to encourage open access and broad distribution of all theses, dissertations, and manuscripts. The Graduate Division will facilitate the distribution of UCSF theses, dissertations, and manuscripts to the UCSF Library for open access and distribution. UCSF will make such theses, dissertations, and manuscripts accessible to the public and will take reasonable steps to preserve these works in perpetuity.

I hereby grant the non-exclusive, perpetual right to The Regents of the University of California to reproduce, publicly display, distribute, preserve, and publish copies of my thesis, dissertation, or manuscript in any form or media, now existing or later derived, including access online for teaching, research, and public service purposes.

DocuSigned by:
5A83B5E6B4A0415...

Author Signature

12/7/2020

Date